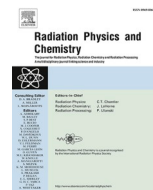

Reprints of Published Research Papers



Effect of swift heavy ions irradiation on physicochemical and dielectric properties of chitosan and chitosan-Ag nanocomposites

Gnansagar B. Patel^a, N.L. Singh^{a,*}, Fouran Singh^b, P.K. Kulriya^b

^a Department of Physics, The M. S. University of Baroda, Vadodra, 390002, India

^b Inter University Accelerator Centre, Aruna Asaf Ali Marg, New Delhi, 110067, India

ARTICLE INFO

Keywords:

Chitosan
Chitosan–silver nanocomposites
Swift heavy ions irradiation
Physicochemical properties
Dielectric spectroscopy

ABSTRACT

Self-sustained films of biodegradable chitosan (CS) and chitosan-Ag nanocomposites (CSN) were prepared by chemical route followed by C^{+5} and Ni^{+7} ions irradiation with varying fluences. The crystallite size decreased from 11.1 to 2.7 nm for CS and 17.6 to 14.2 nm for CSN with increasing ions fluence as observed from the analysis of X-ray Diffraction (XRD) spectra. ATR-FTIR spectra revealed assorted vibrational modes and degradation of polymeric chains in both, CS and CSN matrices upon irradiation. The molecular interactions between main and side-chain functional groups impeded due to nanoparticles confining effects. MeV ions yield low-molecular-weight fragments with degassing of some volatile gaseous species during irradiation. An acute amendment in absorption spectra ascribed to change in surface color and differential absorbance at the wavelength of 370 nm showing blocking of UV radiation. The formation of conjugated linkages and carbonization of CS and CSN matrices lead to decrease in bandgap. Modifications in the physicochemical properties were found to be in persuasive association with changes in frequency-dependent dielectric responses. The shape parameter was moderately decreased and indicating non-Debye relaxation. The conductivity of CS and CSN matrices enhanced and follows the universal dielectric response. The amendment in surface morphology was also revealed upon irradiation.

1. Introduction

The recent innovation in the field of electronic equipment required flexibility, wispy, low-weight and environment-friendly multifunctional materials. Currently, flexible, compact and wearable technology are concerning significant attention worldwide owing to relevance in the wearable healthcare devices, energy storage devices, actuators, biosensors, radiofrequency sensing platforms, and electromagnetic shielding (Moura et al., 2016). Transformable solid-state matrices are the vital needs of these appliances that can accomplish by polymer–nanocomposites, which exhibits superior or newer properties. As a host matrix, polymer materials are explicitly suited due to their viability of processing, flexibility and film-forming capability. Also, polymers having biocompatibility and biodegradability characteristics are preferable and have great importance in diverse applications because of their trivial environmental hazard.

Chitosan (CS) is derived by deacetylation of biopolymer chitin and established as a promising host matrix for the assembly of biomolecules, cells, nanoparticles, and other substances (Koev et al., 2010). Chitosan is

a biodegradable, biocompatible and non-toxic polysaccharide having distinctive hydroxyl ($-OH$) and amine ($-NH_2$) groups and has the excellent film-forming ability (Piroonpan et al., 2020). It shows an impressive mechanical strength, chemical resistance, and thermal stability up to 200 °C (Sakurai, 2000). However, the major difficulty to use pristine chitosan in electronics devices is its low permittivity. This difficulty can be overcome by incorporating weak acids, conducting polymers, plasticizers, salt, and ceramics, etc. into the chitosan. In addition, it can also be solved by embedding nanostructured additives like $BaTiO_3$, TiO_2 , SiO_2 as well as Fe, Cu, Ag, and Au nanoparticles. Among the latter approaches, silver nanoparticles (Ag NPs) were chosen as an additive because of higher-order 10^6 S/cm electric conductivity and have less probability to oxidize or corrode. Moreover, it also exhibits pronouncedly unique behavior in nanosize (<100 nm) due to the quantum size effect as compare to bulk (Parak et al., 2005). Incorporating Ag NPs in the chitosan developed assembly of chitosan–silver nanocomposites (CSN) matrices through interacting with hydroxyl and amine functional groups. Consequently, inter and intra-molecular hydrogen bonds of chitosan macromolecular might affect, which leads

* Corresponding author.

E-mail address: nl.singh-phy@msubaroda.ac.in (N.L. Singh).

<https://doi.org/10.1016/j.radphyschem.2020.109288>

Received 6 June 2020; Received in revised form 1 October 2020; Accepted 15 November 2020

Available online 13 December 2020

0969-806X/© 2020 Published by Elsevier Ltd.

to modification of physicochemical behavior. Hence, the dielectric response of the CSN matrices is also affected. Nowadays, numerous efforts are being elaborated to establish the implementation and functioning of biodegradable nanocomposites in distinctive areas (Sadasivuni et al., 2017).

González-Campos et al. (2010) studied the relaxation processes employing the thermal and dielectric behavior of chitosan-Ag NPs as a function of NPs loading and moisture content. Prokhorov et al. (2011) explored variation in the conductivity of the chitosan-Ag NPs system with temperature using a percolation mechanism. It has been also reported that the electrical and antimicrobial properties of bio-nanocomposites depend on the Ag NPs concentration (González-Campos et al., 2013). Kumar-Krishnan et al. (2015) studied the relationship between electrical, structural, and antibacterial properties of chitosan-Ag NPs and chitosan/Ag⁺ nanocomposites. All these studies proposed a relationship between electrical properties and antibacterial activities by concerning Ag NPs loading. However, beyond a certain extent of nanoparticles loading in matrix ascending ambiguity and hence the system become heterogeneous. Several reports have been published concerning chitosan and Ag NPs in a wide range of fields associating different parameters and conditions (Moura et al., 2016).

Functionalization of CS and CSN importantly broaden its relevance areas and effects. It can be derived by the chemical modification involving grafting of functional molecules and the physical modification involving the physical mixing of organic and/or inorganic constituents. Apart from these, the ionizing radiation approach emerges as an ingenious tool, which can capably functionalize the polymeric materials. The electromagnetic radiation (e.g. UV-rays, X-rays, gamma rays) and particle (electrons, neutrons, or charged species) with energies prominently higher than the dissociation energy of the polymeric linkages considered as an ionizing radiation. These radiations cause irreversible amendments in physicochemical, optical, dielectric, and morphological responses of polymeric matrices (Avasthi and Mehta, 2011; Demina et al., 2014). In the case of photon-matter interactions, the energy of electromagnetic radiation attenuated in a discontinuous manner. The electromagnetic radiation could change the polymeric materials up to a specific level owing to lower deposition of localized energy density in comparison with the particle radiation. Moreover, electrons and charged species have immense capabilities to modify various properties of the polymeric systems than the neutrons irradiation. Fink et al. (1995b) observed that for the same transferred energy density, energetic electrons were slightly less efficient in the polymer damage than the energetic ions. It turned out that the required threshold energy density for the creation of carbonaceous by electron irradiation was found tremendously larger in comparison to heavy ions.

In recent years, well-controlled swift heavy ions (SHIs) irradiation techniques have been found its novel applications and advancement in the discipline of polymer science (Apel, 2019). The effect of SHIs irradiation on materials at the electronic and molecular level are instigated due to the loss of energy of the energetic ions travelling through the materials. The energy loss of SHIs mainly through two distinct processes: (i) nuclear energy loss (S_n) by elastic collisions with the nuclei (ii) electronic energy loss (S_e) by inelastic collisions with the atomic electrons of the target material. The electronic energy loss is found to dominates for SHIs (>10 MeV) and is transferred mainly through excitation and ionization of the atomic electrons (Avasthi and Mehta, 2011). The threshold value for the polymer is of the order of few MeV/ μm and hence relatively large scale electronic energy loss (S_e) of energetic ions could proficiently yield noteworthy changes, which could not achieved by the electromagnetic radiation, electron beam, and low energy ions irradiation (Avasthi, 2009; Hnatowicz, 1999). As the electronic energy loss exceed the threshold value, ionized cylindrical zones are formulated in the irradiated solids due to the passage of energetic ions. The creation of ionized cylindrical regions due to the interaction of SHIs with materials is well-described by the Coulomb explosion model and thermal spike model (Hnatowicz, 1999). Although, the thermal spike model

utterly suit to explain the interaction of SHIs with polymeric host matrices (Singhal and Rattan, 2016). As per this model, the deposited energy is transmitted to the atomic lattice by electron-phonon coupling (Avasthi and Mehta, 2011). Consequently, there is localized thermal quenching for a transient period depending on the energy and kind of incident ion. As an effect, the polymeric macromolecules reorganized owing to a rapid cool-down process lead to a remarkable amendment in the target materials. The reordering of the nanoparticles in the array is also perceived around the ionized cylindrical province of highly doped polymeric matrix.

Biswas et al. (2004) reported that SHIs irradiation introduce realignment of the silver nanocluster into distinct carbonaceous nano-regions in polymeric host. They reveal tailoring of nanoparticles shape and size located on the surface as well as residing the polymer matrix. Mishra et al. (2010) studied that the optical response of polyethylene terephthalate-Ag NPs matrices tuned using SHIs irradiation. The physical properties of Ag NPs embedded polystyrene (Gavade et al., 2011) and polymethyl methacrylate (Gavade et al., 2014) matrices showed an improved response upon SHIs irradiation. Singhal et al. (2016) studied that SHIs irradiation enhances the dispersion of constituent within the polymeric matrix.

The CS and CSN matrices have high-end devotions in biomedical and electrochemical devices (Begum et al., 2016; González-Campos et al., 2010, 2013; Kumar-Krishnan et al., 2014, 2015; Prokhorov et al., 2011; Sadasivuni et al., 2017). As the SHIs irradiation being implicated as a tool to obtain enhanced response of polymer and polymer nanocomposites. The influence depends upon ion range, S_e and diameter of ion track, governed by the informed selection of energy, mass, and fluence of SHIs. The present investigation aimed to study the effect of MeV ions irradiation on the physicochemical response of CS and CSN matrices as a function of electronic energy loss (S_e) and ion fluence. The impacts of these variables on relaxation and conductivity of matrices were investigated by dielectric spectroscopy. Amendment in surface morphology was explored by using SEM and AFM studies. The CS and CSN matrices proposed in the existing investigation can be possibly utilized in optical devices and dielectric applications.

2. Experimental

2.1. Materials

Powder chitosan (degree of deacetylation 75–85%, CAS No. 9012-76-4), acetic acid (ACS reagent, $\geq 99.7\%$, CAS No. 64-19-7) and silver nanoparticle (<100 nm) were purchased from Sigma-Aldrich. The molecular weight of chitosan was evaluated using Ubbelohde capillary viscometer. The viscometric parameters were determined in 0.1 M $\text{CH}_3\text{COOH}/0.2$ M NaCl solution at 25 °C. The experimental evaluation of intrinsic viscosity, $[\eta]$, was performed as per Huggins extrapolation method. After that, the viscosity-average molecular weight (\bar{M}_v) was measured using Mark-Houwink-Sakurada equation, $[\eta] = K(\bar{M}_v)^a$, where $K = 0.00181$ mL/g and $a = 0.93$ are the viscometric constants (Yomota et al., 1993). The average molecular weight of chitosan was equal to 52,408 g/mol.

2.2. Preparation and SHIs irradiation of CS and CSN matrices

The stock solution of chitosan to fabricate the CS and CNS matrices was acquired by the solution casting approach. To yield the matrices of thickness (~ 80 μm), 2% (w/v) concentration of chitosan solution was prepared by dissolving chitosan powder in 1% (v/v) of acetic acid solution. Then, the stock solution was dialyzed to remove undissolved reactants using a qualitative filter paper (Indicator, India). To prepare the nanocomposites matrices with higher Ag NPs concentration (>5 wt %), direct dispersion of Ag NPs powder into the chitosan suspension was employed despite the chemical reduction approach. It was magnetically

stirred at ambient temperature. To obtain the homogeneous dispersion of NPs, the solution was further sonicated for 30 min (Citizen, Model CD 4820). A bath type sonicator having low ultrasonic power (90 W) with 42 kHz frequency was used to minimize the degradation by sonication. The acquired solution was cascaded into a properly balanced and well-cleaned Teflon petri dish. Finally, the CS and CSN matrices severed from the petri dish. For convenience, the CSN matrices were labeled as CSNA, CSNB, and CSNC for 5, 10, and 15 wt% of Ag NPs doping by concerning dry-based chitosan. Moreover, doping of Ag NPs higher than 15 wt% resulted in a heterogeneous matrix. Finally, the acquired matrices were conditioned for additional desiccation in desiccators with silica gel.

The CS and CSN matrices were irradiated with 60-MeV C^{+5} and 100-MeV Ni^{+7} ions at the fluences of 1×10^{11} and 1×10^{12} ions/cm², accessible at the Inter University Accelerator Centre (IUAC), New Delhi, India from 15 UD Tandem Pelletron accelerator (Patel et al, 2016, 2017). The self-sustained films affixed on a rectangular copper ladder and entrenched into a cylindrical vessel, preserved at a high vacuum of $\sim 10^{-6}$ Torr. The (1×1) cm² section of pre-fixed matrices were sequentially scanned in the x-y coordinate by utilizing the electromagnetic scanner for homogeneous irradiation with low current (~ 0.5 pA) ion beam to prevent the heating effects. The SHIs profile, explicitly, mass, energy, and fluence decide the magnitudes of the electronic as well as nuclear energy losses during its passage through polymeric materials (Avasthi, 2009). The projected ranges (R_p) of C^{+5} (60-MeV) and Ni^{+7} (100-MeV) ions and electronic energy loss (S_e) and nuclear energy loss (S_n) for CSNC matrices were calculated using SRIM 2013 code (Ziegler et al., 2010). The simulated values of S_e , S_n and R_p for C^{+5} ion are 108.7 keV/ μ m, 0.06263 keV/ μ m, and 360 μ m, respectively. On the other hand, for Ni^{+7} ion, the corresponding values are 1686 keV/ μ m, 2.979 keV/nm, 84 μ m, respectively. The S_n value of C^{+5} and Ni^{+7} ions considered to be fairly trivial than the value of S_e for the given matrix. Also, the electronic energy loss of Ni^{+7} ion was found to be presumably

higher than the C^{+5} ion.

2.3. Characterizations of CS and CSN matrices

The phase structure of the CS and CSN matrices (pristine and radiation treated) was studied by X-ray diffraction (XRD, Bruker D8-Advance diffractometer). These matrices were scanned in 2-theta range of $5^\circ \leq 2\theta \leq 80^\circ$ with a monochromatic Cu-K α wavelength of 1.5418 Å to record the diffraction patterns. The chemical structure was investigated by ATR-FTIR spectroscopy (JASCO-4100 spectrometer) performed with multi-reflection ATR accessories (ATR PRO410-M). ZnSe was used as an ATR crystal for which the incidence angle of the infrared radiation was 45°. FTIR spectra were collected with a resolution of 1 cm⁻¹ after hundred progressive scans to infer a superior signal-to-noise ratio. The UV-Visible spectrometer was performed in absorption mode to record the optical responses in the span of 200–800 nm wavelength (Hitachi Model U-3300 spectrometer). The dielectric measurements as a function of frequency were executed by using a precision LCR meter in the frequency range 20 Hz to 2 MHz (Agilent E4980A). The self-sustained matrices were sorted between the electrodes of the solid dielectric test fixture (Agilent 16451B) to procure the data at ambient temperature via an entirely computer-assisted interface. The modification of surface morphology was explored by using a field-effect scanning electron microscope (FESEM, Zeiss Merlin VP Compact). Atomic Force Microscopic (AFM) images were used to explore the surface characteristics and roughness parameters (AFM Nanoscope digital instruments, Canberra, USA).

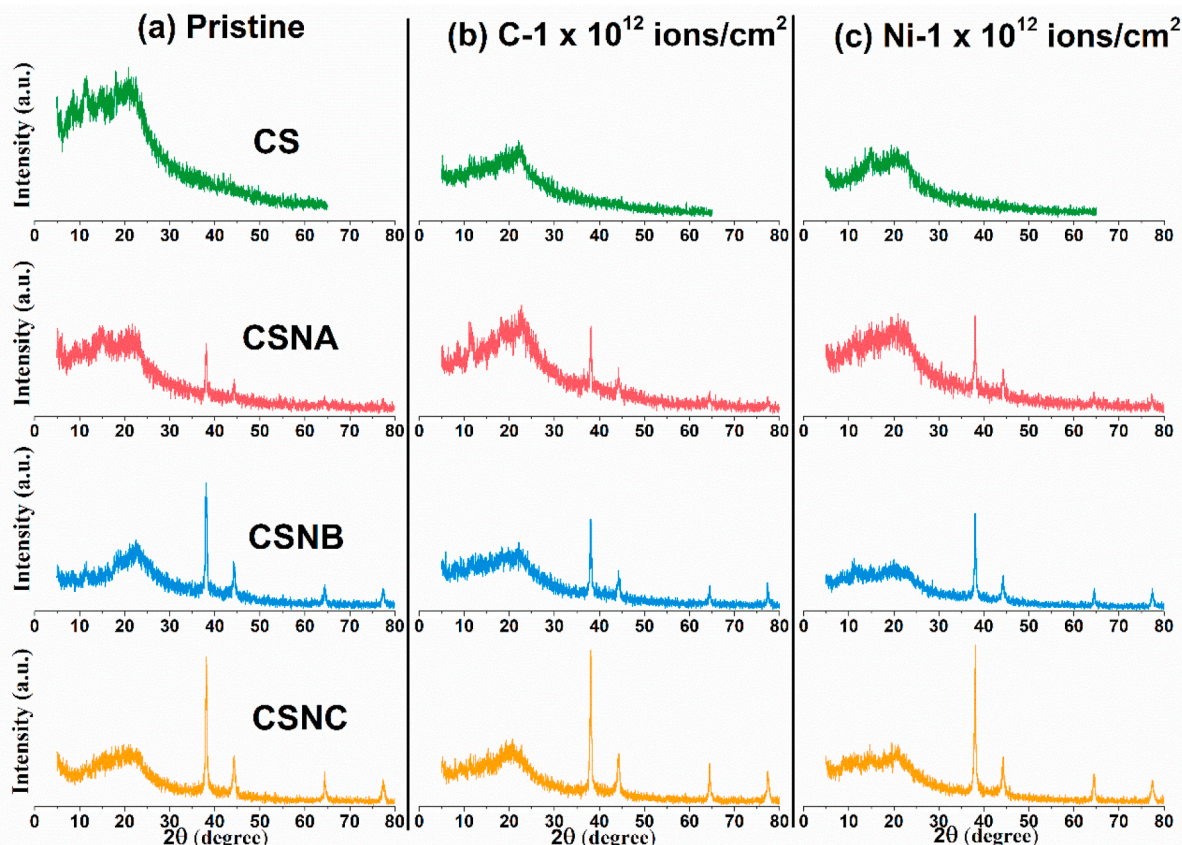


Fig. 1. XRD of (a) pristine CS and CSN matrices irradiated with (b) C^{+5} ions (c) Ni^{+7} ions at the fluence of 1×10^{12} ions/cm².

3. Results and discussion

3.1. XRD analysis

Fig. 1 shows the XRD patterns for pristine and irradiated CS and CSN matrices at the highest fluence of C^{+5} and Ni^{+7} ions. The XRD patterns of the CS illustrate the characteristic diffraction peaks at 8.2° , 11.6° , 15° , 18° , and 21.7° belong to pure chitosan structure (Patel et al., 2017). It is noticed that hydrated crystalline (8.2° and 11.6°) and anhydrous crystalline (15°) structures along with amorphous structure (18° , and 21.7°) (Wang et al., 2005) were suppressed upon irradiation indicating structural disordering. The hydrated form of chitosan has bonded with water molecules in the chitosan matrix (Murugaraj et al., 2011). At the time of SHIs irradiation, a random cascade of ions within the matrix (Avasthi, 2009) destroyed the feeble hydrogen linkages with water molecules as well as $-NH$ or $-OH$ groups of CS promoted deficiency of water molecules along with increasing polymeric free volume. Fig. 1 revealed that due to the incorporation of Ag NPs, only peak at 23° of amorphous structure is seen in the XRD pattern of chitosan, the peaks at 8° and 12° of hydrated crystalline structure of chitosan are much less clear, all the diffraction peaks from Ag NPs are seen in XRD spectra of CSN matrices with 10 and 15% of NPs, but not with 5%. The peaks at 2-theta values of 38.1° , 44.3° , 64.5° and 77.4° correspond to Bragg's reflections from (111), (200), (220) and (311) planes of the face-centred cubic lattice phase of Ag NPs (Kumar-Krishnan et al., 2015). It is evidence of effective integration of Ag NPs in CS assembly. These results are attributed to a strong interaction, mainly at the interfaces between hydroxyl, amine and hydrogen linkages of CS with Ag NPs yielding delocalization in polymeric chains upon additive loading. Moreover, the increase in the degree of amorphization revealed a decrease in the intermolecular interaction between the CS chains.

The percentage crystallinity of CS was estimated using the area ratio method (Singh et al., 2011). For pristine CS, the calculated value of percentage crystallinity is 22.5%. The percentage crystallinity of CS was suppressed upon SHIs irradiation and attained the values of 19.6% and 14.9% for C^{+5} ions, 15.9% and 13.5% for Ni^{+7} ions at the fluences of 1×10^{11} and 1×10^{12} ions/cm², respectively. Also, there is a detectable broadening of the peaks pointed to the alteration in the crystallite domain size. The change in crystalline domain size ascribed to the formation of defects and disorders or grain splitting. The average crystallite size of CS and CSN (pristine and irradiated) matrices was calculated through Scherrer's approach, and listed in Table 1. Incorporating Ag NPs lead to an increase in the average crystallite size of the CSN system due to the dispersion of tiny crystalline NPs. Due to C^{+5} and Ni^{+7} ions irradiation, the average crystallite size of the CSN matrices is considerably reduced with increasing fluence. Indicating that the ions with the higher value of electronic energy loss and higher fluence induced considerable amorphization due to increase in nanoscale free polymeric

volume. Moreover, the SHIs induced effects on the pristine polymer are predominant than the CSN matrices.

3.2. ATR-FTIR analysis

To characterize the SHIs induced effect on functional modes/chemical linkages of CS and CSN as a function of beam parameters and the interaction between CS and Ag NPs within CSN matrices, the IR spectroscopy was employed. The fundamental vibrational modes of CS (Patel et al., 2017) are presented in Fig. 2. The acetate form of CS verified by the band appeared at 1540 cm^{-1} ($-NH_3^+$) rather than at 1590 cm^{-1} ($-NH_2$). At wave number 1710 cm^{-1} , new vibrational mode evolved owing to SHIs irradiation with lower intensity attributed to carbonyl bond vibrations (See inset of Fig. 2). Also, the shifts in amide I group ($C=O$ stretching vibrations) located at 1639 cm^{-1} towards the higher wavenumber (See inset of Fig. 2) attributed to the removal of the adsorbed water due to destruction of intra-chain hydrogen linkages between representative ($-OH$ and $-NH_2$) modes of CS with water molecule (Nogales et al., 1997). The intensity of vibrational modes at 1149 and 1070 cm^{-1} (glucose rings) with 1008 cm^{-1} (glycosidic linkage) decreased, which is ascribed to cleavage of glycidyl linkages exist in $C-O-C$ groups linking tetrahydropyran rings. The stronger overlapping vibrations of $O-H$ stretching with the $N-H$ stretching at 3346 cm^{-1} is

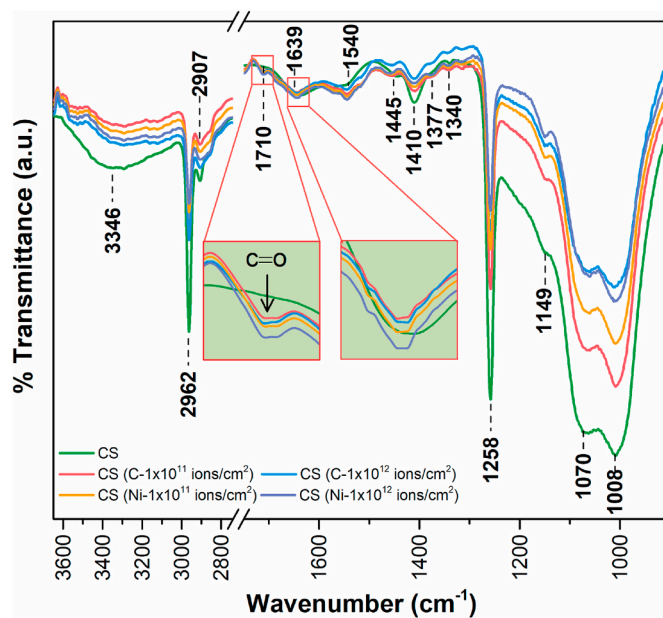


Fig. 2. ATR-FTIR spectra of pre and post C^{+5} and Ni^{+7} ions irradiated CS.

Table 1

Variation in crystallite size, optical energy bandgap (E_g), the number of carbon atoms per conjugation length (N) and R^2 for pristine and irradiated CS and CSN matrices with C^{+5} and Ni^{+7} ions at the fluences of 1×10^{11} and 1×10^{12} ions/cm², respectively.

Sample	C^{+5} (60 MeV)				Ni^{+7} (100 MeV)			
	Crystallite Size (nm)	E_g (eV)	N	R^2	Crystallite Size (nm)	E_g (eV)	N	R^2
Pristine CS	11.1	5.6	-	0.97	11.1	5.6	-	0.97
CS (1×10^{11} ions/cm ²)	8.5	5.5	39	0.91	6.1	5.0	48	0.97
CS (1×10^{12} ions/cm ²)	3.0	3.4	100	0.98	2.7	3.1	122	0.96
Pristine CSNA	14.0	5.0	47	0.97	14.0	5.0	47	0.97
CSNA (1×10^{11} ions/cm ²)	13.4	4.8	51	0.90	12.9	4.6	56	0.98
CSNA (1×10^{12} ions/cm ²)	13.0	3.2	113	0.84	12.0	3.1	121	0.93
Pristine CSNB	15.6	4.9	49	0.96	15.6	4.9	49	0.96
CSNB (1×10^{11} ions/cm ²)	15.3	3.9	77	0.99	15.1	3.8	83	0.99
CSNB (1×10^{12} ions/cm ²)	14.6	3.2	115	0.96	13.8	2.7	162	0.85
Pristine CSNC	17.6	4.7	54	0.96	17.6	4.7	54	0.96
CSNC (1×10^{11} ions/cm ²)	16.2	3.9	79	0.97	14.5	3.6	93	0.88
CSNC (1×10^{12} ions/cm ²)	16.2	2.7	162	0.92	14.2	2.4	203	0.92

affected upon radiation but does not vanish. The band at 1258 cm^{-1} associated with bending vibration of -OH became weak without peak broadening. Moreover, there is momentous suppression of the vibrational modes at 1377 cm^{-1} (symmetric CH_3 deformation and CH bending), 1410 cm^{-1} (CH_2 bending and CH_3 deformation), 1445 cm^{-1} (CH_2 scissoring) and 1340 cm^{-1} (CH_2 wagging) (Kemp, 1991). Asymmetric C-H stretching mode at 2962 cm^{-1} suppressed considerably, while symmetric C-H stretching mode at 2907 cm^{-1} (Kemp, 1991) was not altered. SHIs caused persuasive transformation in vibrational bands of CS concerning intensity and broadening of the peaks. These results revealed to fundamental group abstraction (-OH , -NH_2 , acetyl, and glycidyl linkages) along with hydrogen abstraction.

Fig. 3 shows the additive-dependant IR spectra of CSN matrices. At first, reduction in the intensity and change in peak width upon Ag NPs loading corresponds to strong overlapped stretching mode at $3500\text{--}3300\text{ cm}^{-1}$ is attributed to Ag NPs attachments with N-H (Wei and Qian, 2008). Moreover, the band at 1540 cm^{-1} relatively shifted ($\sim 8\text{ cm}^{-1}$) owing to the linkage of Ag NPs with the nitrogen atom of CS. On account of Ag loading, peak broadening and peak shifting toward lower wavenumber position with diminishing intensity have also been observed (González-Campos et al., 2013; Kumar-Krishnan et al., 2015; Wei and Qian, 2008). The vibrational modes at 1377 , 1445 and 1340 cm^{-1} start merging to 1410 cm^{-1} upon increasing the additive level. In addition, 1410 cm^{-1} shifted toward lower wavenumber region revealed hydrogen bonding due to dipolar coupling between surface charge of Ag NPs and proton in CS. Broadening and increase in intensity of asymmetric vibrational mode at 1149 cm^{-1} attributed to the creation of defects through the charge transfer reaction between Ag NPs and CS matrix. The molecular interactions between main and side-chain functional groups constrained due to presence of silver nanoparticles. The nanoparticles within the polymeric assembly caused confining effects. The adjacent polymeric coating on the surface of the nanoparticles restricts the mobility of macromolecular chains (Mortazavian et al., 2016). The SHIs impact on the CSN matrices (See Fig. 4) revealed a similar trend as observed for the CS, i.e. noteworthy fall in transmittance intensity, broadening, new carbonyl band at 1710 cm^{-1} and overlapping of modes with negligible shift for all vibrational modes.

Figs. 2 and 4 revealed macromolecular polymer structural modification at a molecular level upon SHIs irradiation. Since the electronic energy loss of both the ions is quite higher as compared to the threshold energy (few $\text{MeV}/\mu\text{m}$) for the polymer is yielding columnar type defect

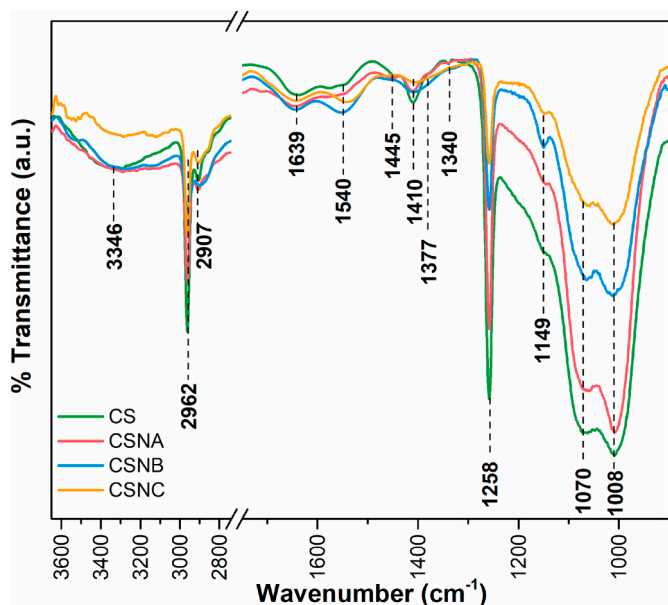


Fig. 3. ATR-FTIR spectra of Ag NPs dependent CSN matrices.

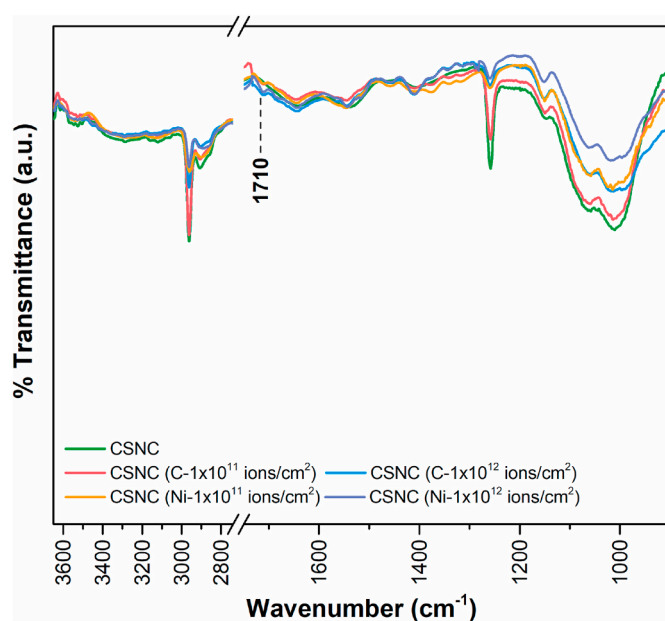


Fig. 4. ATR-FTIR spectra of pre and post C^{+5} and Ni^{+7} ions irradiated CSNC matrices.

or creation of the latent track along the ion trajectory in the polymeric assembly (Avasthi, 2009). The various linkages of polymer structure have a strength of the order of eV (Huheey et al., 1993) and are greatly trivial than S_e values of ions. The kinetic energy of ion in the MeV range gradually decreases during the passage due to the transformation of ion energy to electrons excitation and internal ionization in the keV range. Hence, all kinds of the localized covalent linkages along the ions trajectory experience heterolysis and/or homolysis scission due to random and short time collision cascades producing ionic species and radical species, respectively (Fried, 2014). Accordingly, SHIs cause randomization of macromolecular chains as a result of long chains cleave and disordering due to reorientation of chains. Depending on the molecular mass of the producing species, they may be permanently residing in the bulk or leave the assembly due to a high vacuum. Also, the tremendous elimination in -OH and C-H modes reduced an atomic ratio of hydrogen and carbon. The degradation strongly depends on beam parameters because an ion with greater S_e , heavier mass, and higher fluence caused considerable degradation of polymeric chains in both, CS and CSN matrices.

3.3. Optical analysis

The optical absorption spectra for pre and post C^{+5} and Ni^{+7} ions irradiated CS matrices are demonstrated in Fig. 5. The peak at 310 nm is evidence of the acetate nature of the CS matrix (also revealed from FTIR). Pristine CS exhibits minimal absorption in the visible region ($\sim 400\text{--}800\text{ nm}$) revealed the entirely bound nature of the electrons (Daniels, 1989) in the polymeric materials. Inset of Fig. 5 indicated perceptible enhanced in differential absorbance ($A-A_0$) at the wavelength 370 nm by varying fluence. Also, an abrupt increase in the absorption intensity of the existing peak at 310 nm indicating the formation of color responsive resonating matrix (Abou-Taleb, 2014). Increased intensity of the peak at 310 nm indicating the formation of C=O , C=C and C=NH . The existence of such chromophores within the matrix responsible for change in polymeric material from pale yellow to dark yellow, brown and dark brown with increasing fluence (images not presented here). There is a moderate increase in absorption along with shifting of absorption edge (AE) toward higher wavelength side.

Fig. 6 exhibited a trend of absorption of CS upon treating with various doping levels of Ag NPs. UV absorption response of the metallic

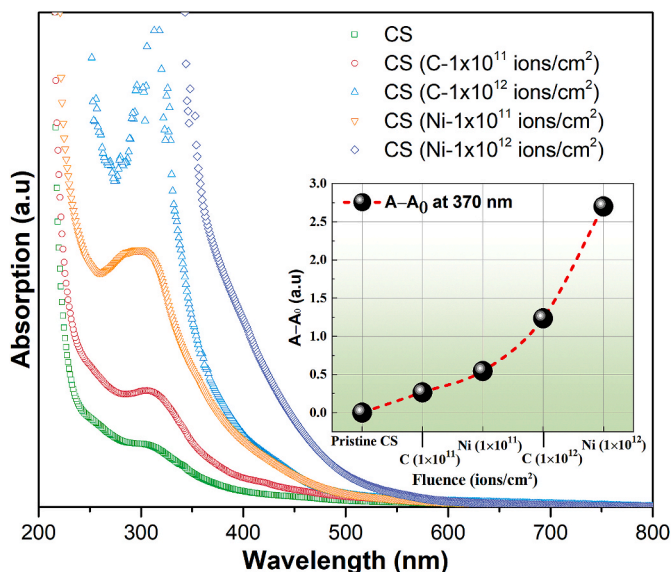


Fig. 5. UV-Vis spectra of (a) pre and post C^{+5} and Ni^{+7} ions irradiated CS.

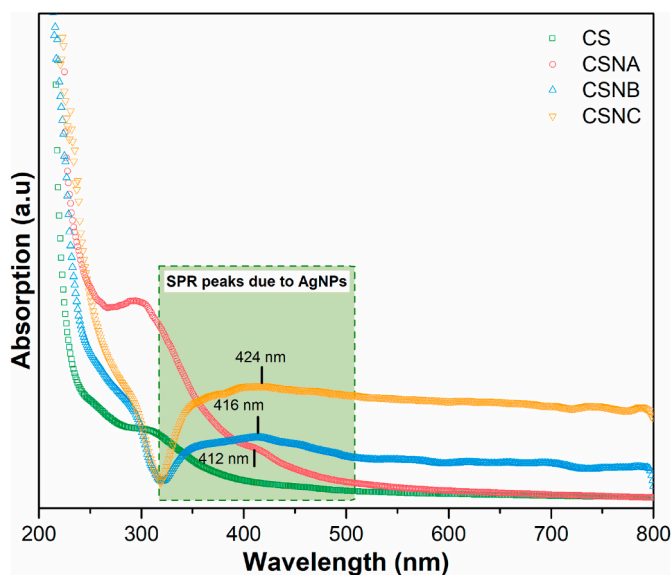


Fig. 6. UV-Vis spectra of Ag NPs dependent CSN matrices.

nanoparticles depending on the dimensions, profiles, and composition of the particle as well as its surrounding medium (Karak, 2019). Further, the separation among the particles within the matrix exhibits substantial influence. The surface plasmon resonance (SPR) peak relevant to Ag NPs appeared at 412 nm, 416 nm, and 424 nm for CSNA, CSNB, and CSNC respectively. Also, the SPR peak exhibited broader and asymmetric nature with a prolonged tail toward the higher wavelength region. This may be ascribed to multipolar excitations and radiative damping due to higher doping and variable-sized Ag NPs dispersion. The SPR peak intensity depends on the excited electrons on account of coherent excitation of the nanomaterials and the surrounded dielectric medium (Persson, 1993).

Upon SHIs irradiation of CSN matrices, the absorption response revealed an appearance of a peak contrary to the pristine one as observed from Fig. 7. SPR peak of CSN exhibited red shift along with an increase in intensity as a function of fluence for both the ions indicating change in size dispersion of Ag NPs and enhance in dielectric constant of a surrounding medium (García, 2011). Modified optical behavior of CSN

subjected to scattering effect of the electron from the surface and the charge transfer process occurred at the particle-polymer interface (Zojer et al., 2019). The surface feature of the nanoparticles may change because of polymer grafting, that is, the polymeric layer adjoined around the nanoparticles might constrain the mobility of the polymer chain and the nanoparticles in consort with increase the effective volume of the nanoparticles. Consequently, influence in inter-particle coupling affect the SPR band (Prakash et al., 2016). The polymer grafting is facilitated by the rapidly occurred cool down events of molten polymeric assembly within 10^{-14} s afterward the MeV ions travel through the host matrix (Avasthi and Mehta, 2011; Fink, 2004). The peak evolved in 300–340 nm range for each CSN matrix ascribed to the formation of chromophores as seen in pristine CS upon irradiation.

Figs. 5 and 7 depicted that the CS and CSN matrices have alike tendency in AE alteration, that is, broadening and red shift, due to ion-material interaction. The broadening ascribed to the creation of defects in terms of wrecking vital linkages and randomization of macromolecular polymeric chains (Kumar et al., 2011). These arguments quite resemble with XRD and FTIR outcomes. The red shift is credited to enhance low molecular-weight species and ions (i.e. charge density). Additionally, the free volume of polymer is enhanced due to profuse mass loss because of outgassing volatile molecular fragments of assorted species. All post-irradiated samples with both the ions at a fluence of 1×10^{12} ions/cm² exhibit expressive absorption from 370 to 510 nm. It shows that CS and CSN biodegradable materials can be used for shielding of UV radiation. The transformation in AE further modified localized energy states, which improve the optical energy bandgap (E_g) of the polymeric matrix.

The optical bandgap and nature of electronic transition between parabolic bands estimated using Tauc's equation,

$$\alpha h\nu = B(h\nu - E_g)^n \quad (1)$$

where h , ν and B are Planck's constant, photon frequency and the energy-independent constant respectively (Tauc et al., 1966). The nature of electronic transition adopts the value of exponent n . In the existing case, the values of E_g were obtained from $(\alpha h\nu)^2 \rightarrow h\nu$ plot by extrapolating the linear least-squares fit of $(\alpha h\nu)^2$ to zero. By using linear regression, an adequate fitting is attained for $n = 1/2$ with reliable goodness-of-fit (R^2). Indicating that the CS and CSN matrices obey quantum mechanically direct allowed transition. Table 1 revealed that due to incorporating Ag NPs, the E_g value of CS eased by $\sim 17\%$, that is, from 5.6 eV (CS) to 4.7 eV (CSNC). Suggesting coordination at the interface between Ag NPs and CS due to profuse accessibility of vital amino and hydroxyl groups resulted in the long-term stability of the matrix. Also, the lower energy transition ensuing foundation of charge transfer complexes between the HOMO and LUMO energy bands. These discussions are also supported by FTIR. The E_g values of CS and CSN were further decline upon C^{+5} and Ni^{+7} ions irradiation. SHIs irradiation proficiently tune the bandgap of CS and CSN matrices as a function of ion fluence. The Ni^{+7} ions remarkably diminishing the bandgap than C^{+5} . Because Ni^{+7} ions caused substantial structural rearrangements, defects formation through unsaturation (Hnatowicz, 1999).

As explained in the ATR-FTIR section, C-H and -OH coordinates have significantly affected by SHIs irradiation. SHIs induced enhance in optical responses also depend on the ratio of hydrogen to carbon atom concentration (H/C) (Compagnini et al., 1990). The excitation and ionization of polymer due to MeV ions interactions may facilitate the phase alteration of sp^3 and sp^2 . Precisely, the hybridization of sp^3 to sp^2 resulted in carbonaceous clustering plus liberation of hydrogen gas (Baptista and Zawislak, 2004). Fink et al. (1995a) presuming that hydrogenated amorphous carbon clusters structure as C_{60} . The number of carbon atoms per conjugation length (N) was evaluated by employing Fink model (Fink et al., 1995a) and tabulated in Table 1. Also, the clustering upon Ni^{+7} ions irradiation consisted excess carbon atoms than C^{+5} ions. This is credited to the abundant deposition of energy within

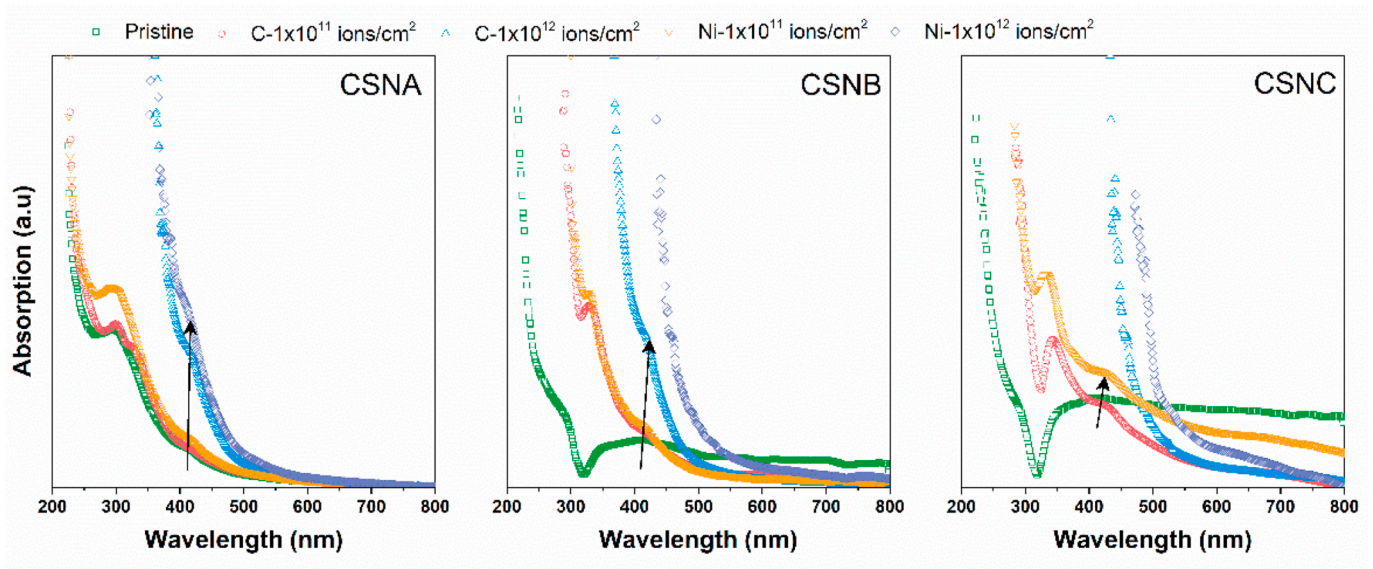


Fig. 7. UV-Vis spectra of pre and post C^{+5} and Ni^{+7} ions irradiated CSNC matrices.

nanometre province could raise the temperature around 10^4 K nearby the ion trajectory (Avasthi and Mehta, 2011). So, the transient products having a short lifetime existing within the formed molten domain along the ion trajectory. Afterward the hyper-thermal circumstances, the physicochemical responses of polymeric matrices modified. These reforms are indorsed to creation of stable fragments with lower molecular masses along with species having unsaturated double or triple bonds (Baptista and Zawislak, 2004; Hnutowicz, 1999). Indeed, modified

physicochemical responses of biodegradable matrices as a function of Ag NPs and beam parameters yielding relevant prompt on dielectric properties.

3.4. AC electrical frequency response

Frequency-dependent dielectric spectroscopy is a versatile technique to avail prominent evidence about the internal behavior of polymer

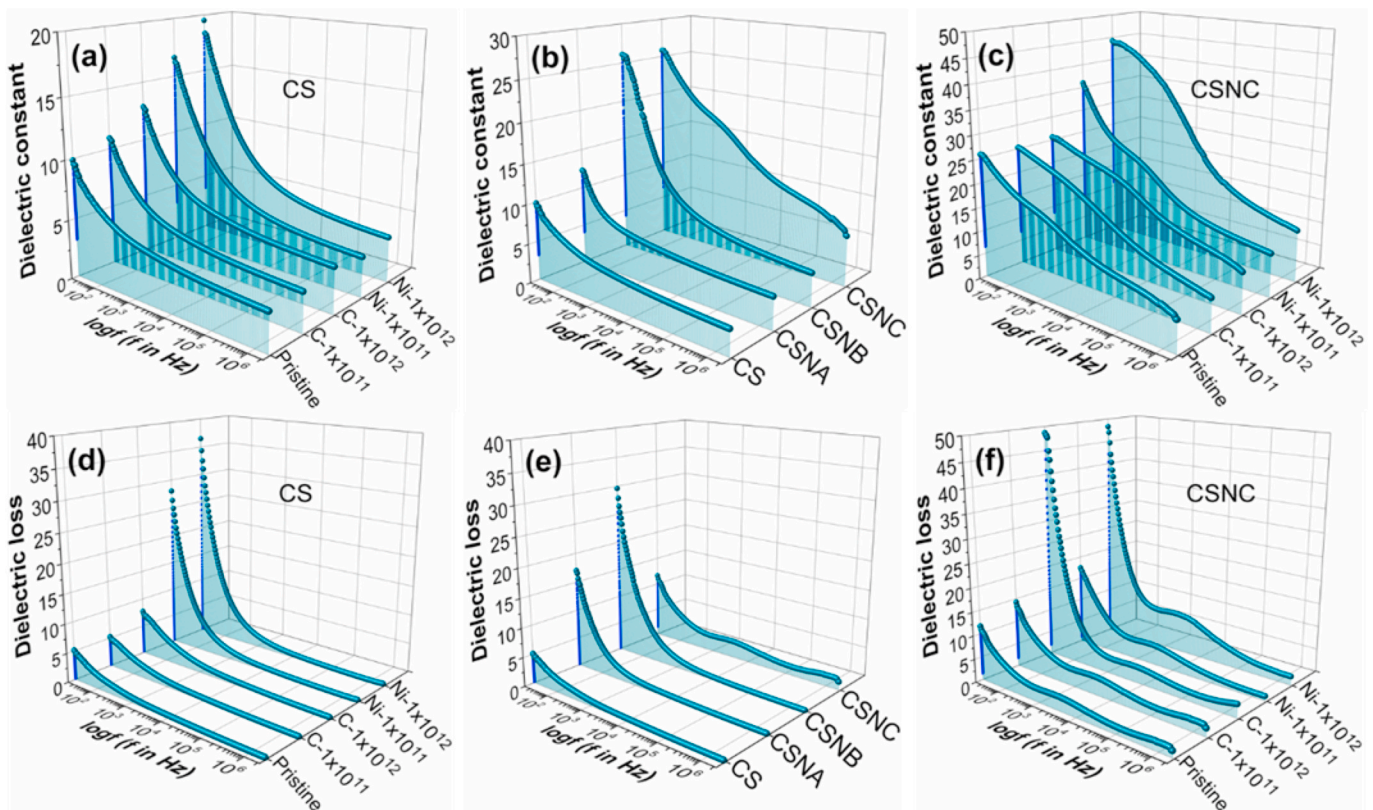


Fig. 8. Plot of dielectric constant versus log frequency for (a) pre and post C^{+5} and Ni^{+7} ions irradiated CS, (b) Ag NPs dependent CSN and (c) pre and post C^{+5} and Ni^{+7} ions irradiated CSNC matrices and plot of dielectric losses versus log frequency for (d) pre and post C^{+5} and Ni^{+7} ions irradiated CS, (e) Ag NPs dependent CSN and (f) pre and post C^{+5} and Ni^{+7} ions irradiated CSNC matrices, respectively.

specimens with nano-filler because of prevailing the distinctive phases (Psarras, 2010). Indeed, the confining effects of nanoparticles and SHIs interaction were reflected in the dynamic fragility and conduction mechanism of the polymer matrix, which could not perceivable by former macroscopic techniques. Therefore, the response of such a complex system can be investigated by using distinctive dielectric formalisms. In which, the integrated consequences of polymeric matrices under the action of the oscillating electric field were explored. The dielectric response of a polymeric matrix is instigated by the atomic, electronic, interfacial, and orientation polarization of the component molecules (Wang et al., 2018).

The real part $\epsilon'(\omega)$ of complex permittivity (ϵ^*) obtained using the measured capacitance (C_p), thickness of self-sustained matrix (d in m) and radius of electrode–matrix contact area (r in m) by following equation,

$$\epsilon'(\omega) = C_p d / \pi r^2 \epsilon_0 \quad (2)$$

where dielectric permittivity of air (ϵ_0) is $8.854 \times 10^{-12} \text{ C}^2/\text{Nm}^2$. Fig. 8 (a) shows the graph of $\epsilon'(\omega) \rightarrow \log f$ for pre and post C^{+5} and Ni^{+7} ions irradiated CS matrices. Indeed, there is an overall increase in $\epsilon'(\omega)$ was perceived with moderately alike frequency dependence trend upon C^{+5} and Ni^{+7} ions irradiation. The broader dispersion in 20 Hz to 3 kHz, whereas beyond 3 kHz a frequency-independent plateau revealed and increased $\epsilon'(\omega)$ with fluence for both the ions. The $\epsilon'(\omega)$ value for Ni^{+7} ions irradiation in the dispersion region seemed higher for the fluences of 1×10^{11} and 1×10^{12} ions/cm². The $\epsilon'(\omega)$ response in dispersion region ascribed to modify molecular dynamics, specifically, as revealed from FTIR, the Ni^{+7} ions tremendously rupture polymeric main and side chains yielding lower-mass macromolecular and enhancing chain segmental mobility. Also, enhanced free polymeric volume as revealed from XRD may reduce the cohesive forces functioning between the polymeric chains also improve chain segmental mobility. The lower frequency response of matrices attributed to space charges/interfacial and electrode electric double-layer polarization due to succeeding consequences of $-\text{NH}_2$ and $-\text{O}-$ groups dipoles orientation plus long-range charge carriers fluctuations across the matrix owing to a slower rate of time-dependent electric field (Pal et al., 2019; Patel et al., 2019). Whereas beyond 3 kHz, dipoles begin to lag behind the field yielded frequency-independent response of matrices. However, the improved value of $\epsilon'(\omega)$ in plateau section indorsed to induce charge carrier density and instigation of defect sites due to matrix-ion interactions as argued in UV–Visible findings.

Fig. 8 (b) exhibits the graph of $\epsilon'(\omega) \rightarrow \log f$ for CSN matrices. The increased loading of Ag NPs in the matrix caused solely increase in the dielectric constant. Since the CSN matrices embraced metallic islands in an insulating host. Therefore, the substantial diversity in conductivities of two phases yielding the formation of interfacial dipole mainly at the interface due to partial charge transfer (Zojer et al., 2019). Under the influence of the field, these dipoles being polarized and indorsed to the dielectric constant. Fig. 8 (c) revealed graph of $\epsilon'(\omega) \rightarrow \log f$ for pre and post C^{+5} and Ni^{+7} ions irradiated CSNC matrices. There is an overall noteworthy increment in $\epsilon'(\omega)$ upon irradiation over the entire frequency region revealed in high dielectric materials in alternatives for flexible and stretchable electronics for electromagnetic shielding purpose (Wang et al., 2018). Indeed, the structural rearrangement upon SHIs irradiation of highly doped heterogeneous polymer matrix with variable-sized Ag NPs may facilitate cluster-to-cluster interaction due to increased correlation length. These discussions were further supported by the prior studies carried out by our group proposing the SHIs irradiation induced modification of different polymer composites systems (Gavade et al., 2011, 2014; Qureshi et al., 2008; Singh et al., 2007, 2011).

Fig. 8(d–f) illustrated $\epsilon''(\omega) \rightarrow \log f$ for pre and post C^{+5} and Ni^{+7} ions irradiated CS, Ag NPs dependent CSN and pre and post C^{+5} and Ni^{+7} ions irradiated CSNC matrices respectively. The dielectric loss diminished with the increase in the frequency up to 1 kHz, subsequently, the

dielectric loss attained a lower value and fairly does not depend on frequency for all the matrices under study. The exponent nature resembles that the polarization influence is dominant in the matrices than the dc conductivity (Ku and Liepins, 1987). For CSN matrices, the $\epsilon''(\omega)$ increased in 20 Hz to 1 kHz frequency range as a function of Ag NPs loading. Except, minor relaxation in the frequency range 1 kHz–20 kHz for the CSNC matrix. This implies that the Ag NPs doping influences the relaxation of the polymeric chain due to nanoparticle confining effects. SHIs irradiated CS and CSN matrices exhibited alike frequency dependent response, except, lower frequency dispersion.

The electric modulus spectra concern with the relaxation of a field in the bulk, hence being an ingenious perspective in the analysis of dielectric spectroscopy. Providing prospects to study and investigate phenomena involving relaxation and conduction response at a microscopic extent, excluding the low-frequency dispersion occurrences (Prokhorov et al., 2011). So, the electric modulus formalism has been introduced using the frequency-dependent $\epsilon'(\omega)$ and $\epsilon''(\omega)$ values as explained elsewhere (Steinmetz, 2012).

The imaginary modulus spectra showed a peak as perceived from Fig. 9(a–c). The $M''(\omega) \rightarrow \log f$ plots have a loss peak at the distinctive relaxation frequency f_{max} for pre and post C^{+5} and Ni^{+7} ions irradiated CS and CSN matrices, respectively. Observed relaxation in window of ($f < f_{max}$) indorsed to the existence of interfacial polarization plus long-range migration of charge carriers, explicitly, efficient hopping between the adjacent sites (Aziz et al., 2010). Whereas the relaxation for frequencies ($f > f_{max}$) attributed to short-range migration of charge carriers within potential wells (Patel et al., 2017). The Kohlrausch–Williams–Watt (KWW) (Williams and Watts, 1970) elicited empirical exponential function explicitly well-fitted the experimental data of the frequency-dependent $M''(\omega)$ graphic in the frequency province was amended by Bergman and can be expressed as follows (Bergman, 2000):

$$M''(\omega) = \frac{M''_{max}}{(1 - \beta_{KWW}) + \left[\left(\frac{\beta_{KWW}}{1 + \beta_{KWW}} \right) \left(\beta_{KWW} \left(\frac{f_{max}}{f} \right) + \left(\frac{f}{f_{max}} \right)^{\beta_{KWW}} \right) \right]} \quad (3)$$

where β_{KWW} is the Kohlrausch coefficient with the condition $0 \leq \beta_{KWW} \leq 1$ and M''_{max} is the peak value of the imaginary electric modulus curve. The value of $\beta_{KWW} = 1$ signifies the ideal Debye relaxation response and the value of β_{KWW} less than unity signifies a non-ideal Debye relaxation response (Bergman, 2000; Williams and Watts, 1970). The solid symbol in Fig. 9(a–c) stands for the superior fitting of the $M''(\omega)$ curve, whereas the hollow symbol resembles to experimental data. The defined fitting to the experimental frequency-dependent $M''(\omega)$ values with simulated predictable values is endorsed using the figure of merit (FOM) estimation. The parametric values β_{KWW} , M''_{max} and f_{max} estimated from the Bergman equation fit are summarised in Table 2 for pre and post irradiated CS and CSN matrices. The value of β_{KWW} is less than unity for all the matrices approved non-Debye relaxation response. The relocation in relaxation peak toward higher frequencies as a function of ion fluence perceived in the case of the CS matrix (see Fig. 9 (a)). While Ag NPs loading exhibited alike trend along with modification in peak shape, that is, broadening and the peak value of $M''(\omega)$ curve, as indorsed from Fig. 9 (b). The relaxation peak of the CSNC matrix is broader and have a smaller value of M''_{max} (see Fig. 9 (c)). Indeed, owing to nanoparticles confining restrict, the molecular interactions between main and side-chain functional groups assisted the macromolecules movement of individual chains. Hence, the relaxation time of the process becomes shorter and the relevant loss peak is recorded at a higher frequency (Psarras, 2010). The Ag NPs loading affects the conduction phenomenon also. The $\epsilon''(\omega) \rightarrow \log f$ and $M''(\omega) \rightarrow \log f$ curves of the CS does not individually involve loss peak indicating relaxation process, while in the case of CSNC matrix, the loss peak present in both graphics indicating conduction process, not a relaxation one (Begum et al., 2016). Upon SHIs irradiation, the relocation of relaxation peak to higher frequencies

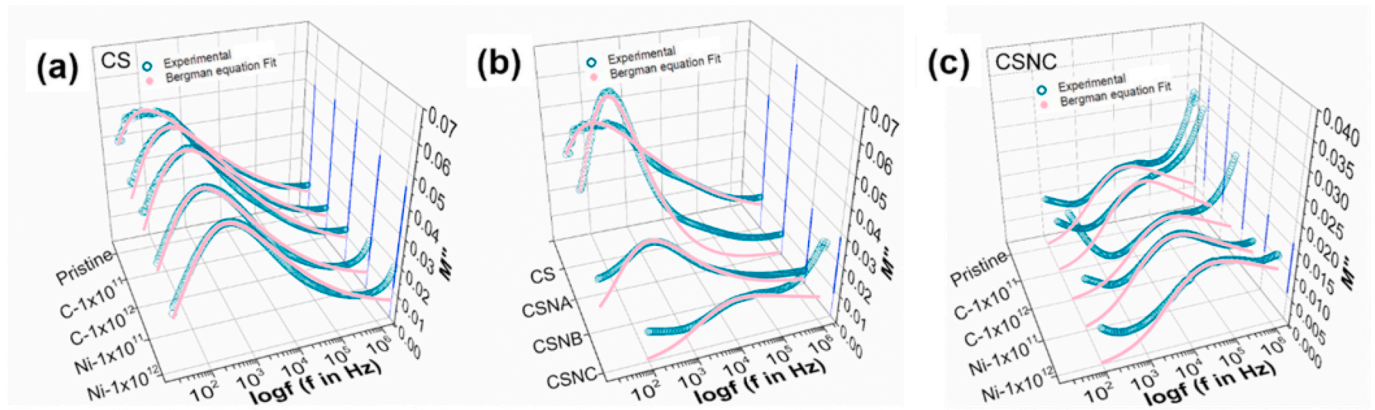


Fig. 9. Bergman equation fit of imaginary part of modulus versus log frequency for (a) pre and post C^{+5} and Ni^{+7} ions irradiated CS, (b) Ag NPs dependent CSN and (c) pre and post C^{+5} and Ni^{+7} ions irradiated CSNC matrices.

Table 2

Parameter values obtained from the Bergman equation fit.

Sample	M''_{max}	f_{max}	β_{KWW}	FOM (%)
CS	0.08415	179	0.42121	5.32
CS ($C-1 \times 10^{11}$ ions/cm ²)	0.08411	600	0.26855	4.31
CS ($C-1 \times 10^{12}$ ions/cm ²)	0.08395	700	0.26121	4.06
CS ($Ni-1 \times 10^{11}$ ions/cm ²)	0.07644	610	0.30427	5.49
CS ($Ni-1 \times 10^{12}$ ions/cm ²)	0.07324	820	0.30124	6.18
CSNA	0.10100	217	0.52577	9.83
CSNB	0.04488	770	0.39114	9.61
CSNC	0.02690	43,870	0.24855	5.05
CSNC ($C-1 \times 10^{11}$ ions/cm ²)	0.02680	44,000	0.28847	10.30
CSNC ($C-1 \times 10^{12}$ ions/cm ²)	0.02247	100,547	0.24180	7.63
CSNC ($Ni-1 \times 10^{11}$ ions/cm ²)	0.02617	45,000	0.24642	1.73
CSNC ($Ni-1 \times 10^{12}$ ions/cm ²)	0.02611	135,000	0.20121	3.62

is also perceived for CS and CSN matrices. Hence, the relaxation phenomenon can be a SHIs assisted consequence involving the fundamental hopping mechanism of the charge. In consequence of C^{+5} and Ni^{+7} ions irradiation, the values of M''_{max} decreased and shifted toward higher frequencies indicates the transformation of materials. The SHIs irradiation induced macroscopic dielectric response originates from the alignment of induced dipoles present in an amorphous province and the existence of free side chains and radicals in the matrix. The dielectric modulus behavior has a persuasive consonance with FTIR response.

The total electrical conductivity, $\sigma(\omega, T)$, was estimated as the addition of the plateau region appeared at lower frequencies contributing as direct current, σ_{dc} , and the frequency-dependent dispersive region emerged at higher frequency contributing as alternate current, $\sigma_{ac} = B\omega^s$. The frequency-dependent conductivity principally obeys the

Jonscher universal power law as follow (Jonscher, 1996):

$$\sigma(\omega, T) = \sigma_{dc} + B\omega^s \quad (4)$$

where B is pre-exponential parameter and s ($0 \leq s \leq 1$) is dimensionless temperature-dependent fractional exponent (Jonscher, 1996). Fig. 10 (a-c) revealed the variation of frequency-dependent total conductivity for pre and post C^{+5} and Ni^{+7} ions irradiated CS, Ag NPs dependent CSN, and pre and post C^{+5} and Ni^{+7} ions irradiated CSNC matrices respectively. The σ_{dc} was evaluated by extrapolation of the σ plateau to zero frequency. Fig. 11 illustrates the variation in dc conductivity concerning ion beam parameters and Ag NPs loading. The dc conductivity moderately increased upon Ag NPs loading, this kind of response was reported in the literature for CSN matrices (Kumar-Krishnan et al., 2015; Prokhorov et al., 2011). The dc conductivity enhanced upon C^{+5} and Ni^{+7} ions irradiation infers successful hopping of charge carriers between adjacent sites due to increased amorphous phase. The migration of charge carriers with increasing frequencies is hindered. The conductivity graphics revealed that beyond the critical frequency (f_c), the conductivity of matrices increases steeply as stated by the power law. The values of σ_{ac} beyond the f_c further boosted with an increase in fluence attributed to the creation of defect in terms of degradation of macromolecules through chain scissioning, formation of C=O, C=C and C=NH linkages plus sp^2 hybridization and enriched localized carbon-rich network (Compagnini et al., 1990; Fink, 2004; Fink et al., 1995a; Gavade et al., 2014). The exponent "s" calculated from the slope ($d\sigma_{ac}/d\omega$) of $\log\sigma_{ac} \rightarrow \log\omega$ curve measured using linear regression approach at higher frequency window to suppress the interfacial polarization influences. The modification in the value of "s" by considering the variable parameters of SHIs irradiation and Ag NPs loading observed from Fig. 12. The goodness-of-fit (R^2) varies moderately between 0.97

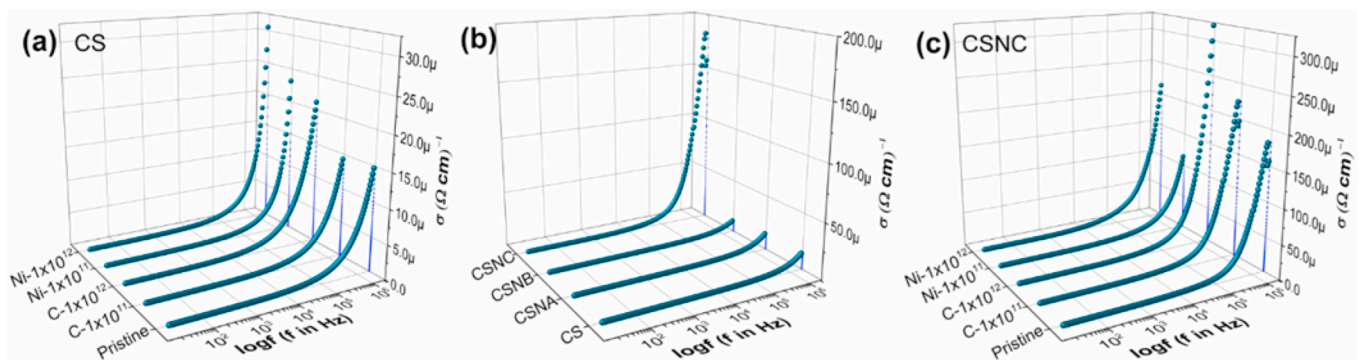


Fig. 10. Plot of conductivity versus log frequency for (a) pre and post C^{+5} and Ni^{+7} ions irradiated CS, (b) Ag NPs dependent CSN and (c) pre and post C^{+5} and Ni^{+7} ions irradiated CSNC matrices.

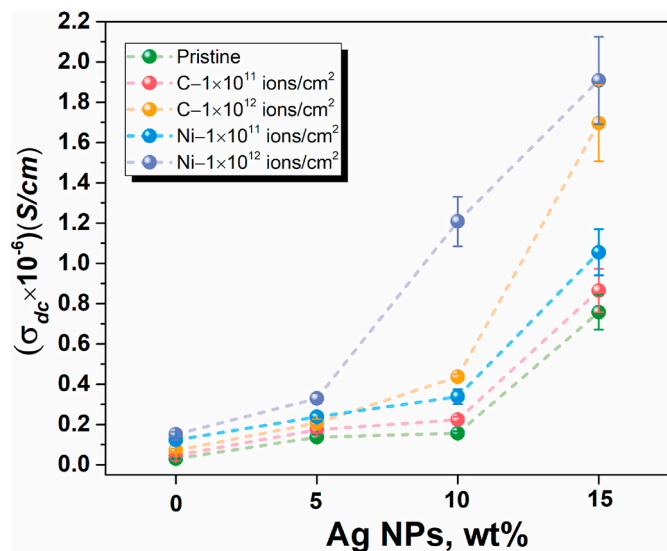


Fig. 11. Variation in dc conductivity as a function of ion fluence.

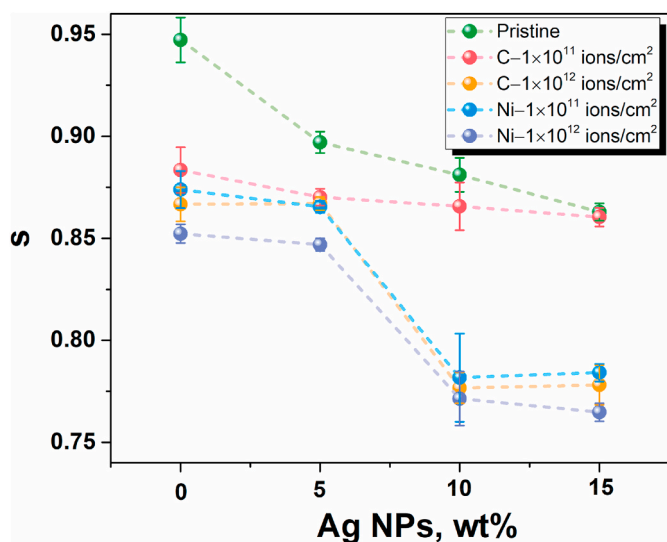


Fig. 12. Variation in frequency exponent "s" as a function of ion fluence.

and 0.99 showed a reliable accuracy of measurement. The frequency exponent attained the values in between 0.94 and 0.76 with a maximum standard deviation of ± 0.02 . This indicates hopping of charge carriers is suitable conduction mechanism and it is AC type (Jonscher, 1996). Fig. 13 revealed the linear response of $\log(f\epsilon'')$ vs $\log f$ graph over a broad spectrum of frequency range for pre and post C^{+5} and Ni^{+7} ions irradiated CS and CSN matrices. This is credited to the well-defined dominance of the universal dielectric response (UDR) model, wherein the hopping of charge carriers between adjacent sites coupled with the dipolar relaxation, generally, observed in a persuasive disordered/amorphous materials (Bowen and Almond, 2006; Elliott, 1994).

3.5. Surface morphology

Fig. 14(a–f) displays the Scanning Electron Micrograph (SEM) of pre and post C^{+5} and Ni^{+7} ions irradiated CS (Fig. 14(a–c)) and CSNC (Fig. 14(d–f)) matrices at a fluence of 1×10^{12} ions/cm². The SEM micrograph of the CS revealed irregular surface morphology evolving the nodules possess the crystallized domains due to the slower rate of evaporation (Ghosal et al., 2018). Definitely belong to the hydrated

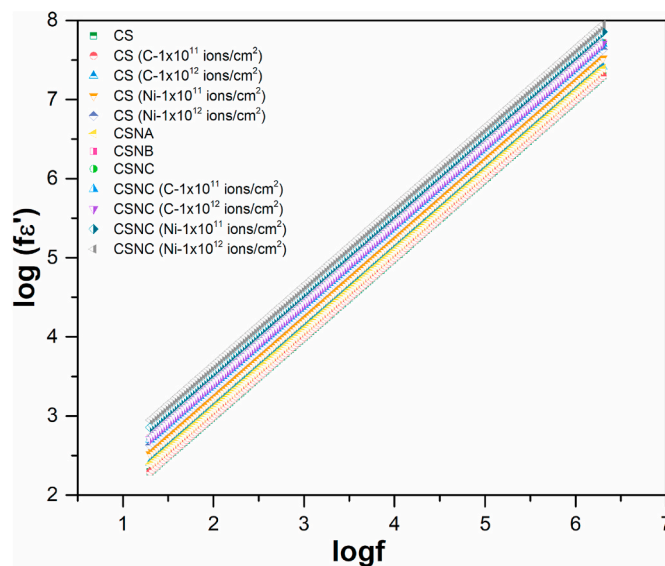


Fig. 13. Plot of $\log(f\epsilon'')$ versus \log frequency for pre and post C^{+5} and Ni^{+7} ions irradiated CS, Ag NPs dependent CSN and pre and post C^{+5} and Ni^{+7} ions irradiated CSNC matrices.

crystalline (8.2° and 11.6°) and anhydrous crystalline (15°) structures of the CS as discussed in XRD. Inset micrograph of Fig. 14 (a) revealed crevices also attributed to the semi-crystalline nature of the CS. Presumably, the extinction of the crevices upon the Ag NPs loading in the polymeric matrix as observed from Fig. 14 (d) ascribed to significant interaction between fillers and polymeric chains, mainly at the interface, as inferred in physicochemical responses. As can be perceived that the SHIs irradiation caused prominent modifications in the surface morphologies of the CS and CSNC matrices. Comparatively, the flatter morphologies of SHIs irradiated matrices than pristine one evidences of induced amorphous phase. The energetic C^{+5} and Ni^{+7} ions steeply boosted the localized temperature within a few picoseconds period originating from a rapid molten provinces nearby the ion trajectory (Avasthi and Mehta, 2011). Consequently, the polymeric chains rearrange themselves yielding enhanced interfacial interaction together with the formation of new chemical linkages and defects. The ion trajectories overlapped with an increase in ion fluence due to rapid quenching resulted in a carbon-rich network with an enhanced conjugated system. Inclusively, the Ni^{+7} ion imparts a substantial impact on surface topography owing to tremendous electronic loss.

Fig. 15(a–f) shows AFM images of CS and CSNC before and after exposure to C^{+5} and Ni^{+7} ions at the fluence of 1×10^{12} ions/cm². One can notice that the surface morphology of CS and CSN reformed under SHIs irradiation. The analysis of AFM images was performed to obtain the Root Mean Square (RMS) roughness (R_q) and average roughness (R_a) parameters. The AFM images for virgin CS and CSNC appeared distinctive with hillock-like structures. The R_q and R_a for CS were found to be 15.2 nm and 11.8 nm, respectively. The R_q decreased to 10.4 nm and 10.3 nm, whereas, the R_a decreased to 8.4 nm and 8.3 nm upon C^{+5} and Ni^{+7} ions irradiation, respectively. The values of R_q and R_a were moderately changed for chitosan. Although the substantial impact of MeV ions irradiation on the physicochemical properties of CS was experienced, which is not attributed to the roughness parameters. A similar kind of trend in surface morphology of the CS matrix was also observed upon UV treatment (Kowalonek, 2017). The reason behind such a respond upon SHIs irradiation is resembled to melting and resolidification cascades due to superlative temperature ($\sim 10^4$ K) (Avasthi and Mehta, 2011) resulted in polymeric degradation and production of transient elements, which are eventually distributed on the surface with evacuation of some volatile gases. The smoothness and homogeneity of the CS surface were enhanced due to SHIs irradiation. For

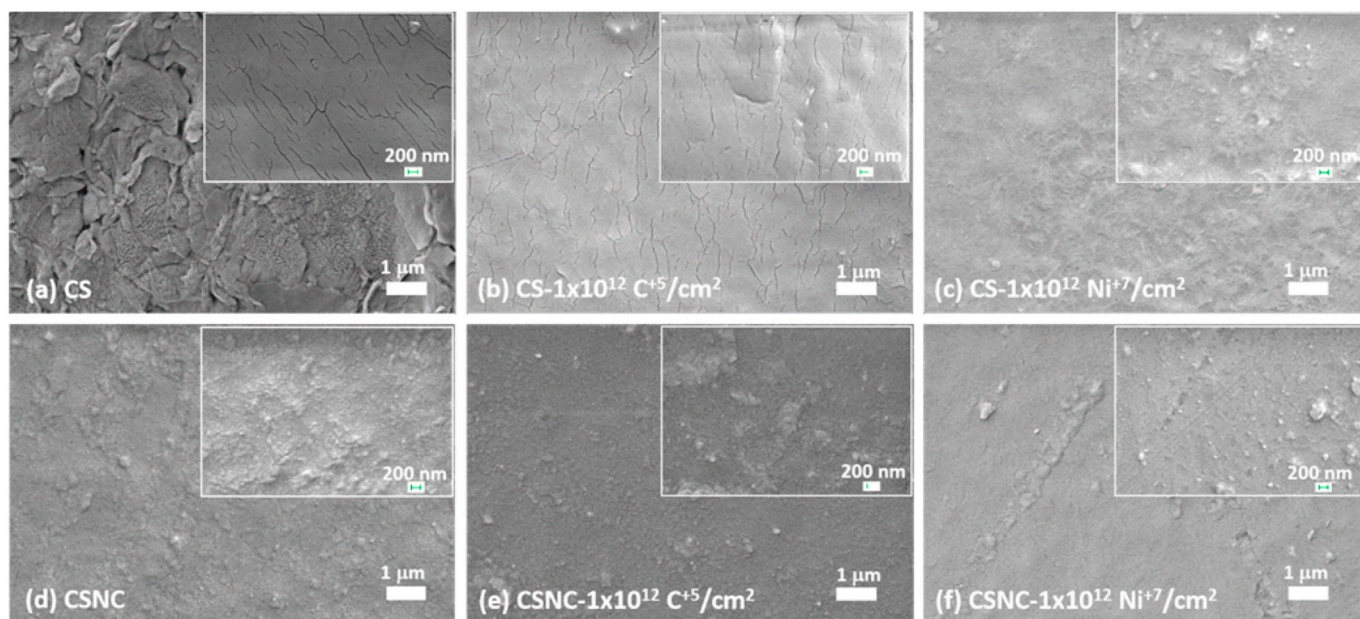


Fig. 14. SEM micrographs of pristine CS (a), irradiated with C^{+5} ions (b), Ni^{+7} ions (c) at the fluence of 1×10^{12} ions/cm² and pristine CSNC (d), irradiated with C^{+5} ions (e), Ni^{+7} ions (f) at the fluence of 1×10^{12} ions/cm².

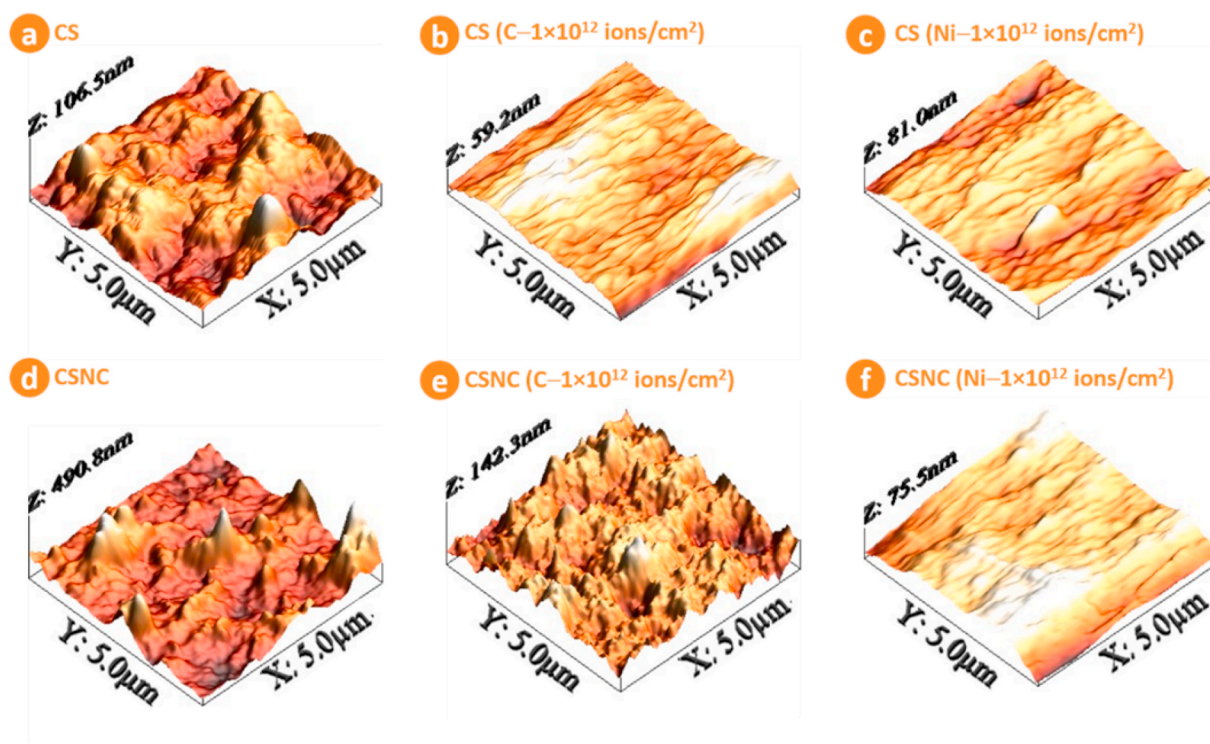


Fig. 15. AFM images of pristine CS (a), irradiated with C^{+5} ions (b), Ni^{+7} ions (c) at the fluence of 1×10^{12} ions/cm² and pristine CSNC (d), irradiated with C^{+5} ions (e), Ni^{+7} ions (f) at the fluence of 1×10^{12} ions/cm².

the CSNC matrix, the R_q and R_a were found to be 71.2 nm and 50.3 nm, respectively. An incorporation of nano-filler within the matrix considerably increased the surface roughness. The increase in roughness parameters is due to the increase of density and size of metal particles on the surfaces of the chitosan films (Qureshi et al., 2008; Singh et al., 2011). After C^{+5} and Ni^{+7} ions irradiation, the value of R_q decreased to 19.2 nm and 12.3 nm, whereas the value of R_a decreased to 15.2 nm and 9.4 nm, respectively. These findings ascribed to the immense collision impact of ions over the relatively soft polymeric surface might wreck the

hill-like features and caused localized surface diffusion of nanoparticles within the matrix. The AFM analysis was complemented to the SEM imaging admitted qualitatively and quantitatively investigations of the topographical features of the matrices.

4. Conclusions

Biodegradable self-sustained matrices of chitosan and hybrid chitosan were formed *via* solution casting route. The matrices were irradiated

with energetic C^{+5} and Ni^{+7} ions to study the perception of comprehensive modifications induced as a function of beam parameters. The structural and microstructural/SEM revealed successful Ag NPs loading within matrices and an increase in the degree of disorder upon SHIs irradiation. Modifications in vibration modes of matrices due to Ag NPs confining effects and SHIs irradiation were monitored by ATR-FTIR spectroscopy. The ATR-FTIR analysis showed degradation of matrices due to the scission of multiple linkages of main and side chains accompanied by the appearance of new carbonyl bonds. Particularly, the vibrational mode concerning C–H linkages reduced drastically due to substantial hydrogen abstraction. Accordingly, double bonds are prompted due to sp^2 clustering yielding a carbon-rich network as inferred in optical response. The optical band gap decreased upon Ag NPs loading and SHIs irradiation attributable to the origination of defects due to charge transfer reaction between polymer and surface of the nanoparticles and radiation-induced disorder respectively. Also, the successive red shift of the AE figure out the utilization of matrices under investigation as shielding of UV photons. The physicochemical modifications are reflected in conduction and macromolecular relaxation aspects and comprehensively interpreted in distinct dielectric formalisms. The frequency-dependent values of $\epsilon'(\omega)$ increased over a wide span together with lower frequency dispersion. The dynamics of molecules also influence due to nanoparticle confining effects and SHIs irradiation. Interestingly, the higher loading of filler hindered the molecular interaction and SHIs induced chains scissoring with lower molecular mass enhance molecular dynamics. The conductivity, that is, ac and dc both considerably enhanced with fluence and followed the power law. The transport of the charge carriers in the matrices is due to hopping cascade and the matrices under investigations imitate according to the UDR model. Inclusively, our investigation shows that the environment-friendly polymeric matrices functionalized respecting the many aspects by suitably selecting privies parameters of MeV ion. The functionalized matrices are capably used as UV and electromagnetic shielding materials.

CRedit authorship contribution statement

Gnansagar B. Patel: Conceptualization, Methodology, Software, Formal analysis, Investigation, Data curation, Writing - original draft, Writing - review & editing, Visualization. **N.L. Singh:** Conceptualization, Methodology, Formal analysis, Investigation, Resources, Data curation, Writing - original draft, Writing - review & editing, Supervision, Project administration. **Fouran Singh:** Conceptualization, Investigation, Data curation, Writing - review & editing. **P.K. Kulriya:** Investigation, Data curation, Writing - review & editing.

Declaration of competing interest

The authors declare that they have no known competing financial interests or personal relationships that could have appeared to influence the work reported in this paper.

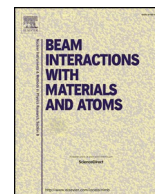
Acknowledgments

One of the authors (GBP) appreciatively acknowledges the DST-PURSE program for the award of research fellowship. The authors thanks to IUAC, New Delhi for capacious support throughout the beam time experiment, post-irradiated XRD, UV-Visible and AFM characterizations, and financial assistance. We gratefully acknowledge Dr. Mukesh Ranjan, FCIPT, Gandhinagar, Gujarat, and Prof. V. A. Rana, Department of Physics, School of Sciences, Gujarat University for providing SEM and LCR facilities respectively.

References

- Abou-Taleb, M.H., 2014. Characterization of polymer blends using UV-visible spectroscopy. In: *Characterization of Polymer Blends*. Wiley-VCH Verlag GmbH & Co. KGaA, Weinheim, Germany, pp. 789–820. <https://doi.org/10.1002/9783527645602.ch24>.
- Apel, P.Y., 2019. Fabrication of functional micro- and nanoporous materials from polymers modified by swift heavy ions. *Radiat. Phys. Chem.* 159, 25–34. <https://doi.org/10.1016/j.radphyschem.2019.01.009>.
- Avasthi, D., 2009. Modification and characterisation of materials by swift heavy ions. *Defence Sci. J.* 59, 401–412. <https://doi.org/10.14429/dsj.59.1540>.
- Avasthi, D.K., Mehta, G.K., 2011. *Swift Heavy Ions for Materials Engineering and Nanostructuring*, Springer Series in Materials Science. Springer Netherlands, Dordrecht. <https://doi.org/10.1007/978-94-007-1229-4>.
- Aziz, S.B., Abidin, Z.H.Z., Arof, A.K., 2010. Influence of silver ion reduction on electrical modulus parameters of solid polymer electrolyte based on chitosan-silver triflate electrolyte membrane. *Express Polym. Lett.* 4, 300–310. <https://doi.org/10.3144/expresspolymlett.2010.38>.
- Baptista, D.L., Zawislak, F.C., 2004. Hard and sp^2 -rich amorphous carbon structure formed by ion beam irradiation of fullerene, a-C and polymeric a-C:H films. *Diam. Relat. Mater.* 13, 1791–1801. <https://doi.org/10.1016/j.diamond.2004.04.006>.
- Begum, S.N.S., Aswal, V.K., Ramasamy, R.P., 2016. Small-angle neutron scattering and spectroscopic investigations of fractal formation in chitosan-Ag nanocomposite facilitated by hydrazine hydrate. *J. Phys. Chem. C* 120, 2400–2410. <https://doi.org/10.1021/acs.jpcc.5b09747>.
- Bergman, R., 2000. General susceptibility functions for relaxations in disordered systems. *J. Appl. Phys.* 88, 1356–1365. <https://doi.org/10.1063/1.373824>.
- Biswas, A., Avasthi, D.K., Fink, D., Kanzow, J., Schürmann, U., Ding, S.J., Aktas, O.C., Saeed, U., Zaporozhtchenko, V., Faupel, F., Gupta, R., Kumar, N., 2004. Nanoparticle architecture in carbonaceous matrix upon swift heavy ion irradiation of polymer-metal nanocomposites. *Nucl. Instrum. Methods Phys. Res. Sect. B Beam Interact. Mater. Atoms* 217, 39–50. <https://doi.org/10.1016/j.nimb.2003.09.032>.
- Bowen, C.R., Almond, D.P., 2006. Modelling the “universal” dielectric response in heterogeneous materials using microstructural electrical networks. *Mater. Sci. Technol.* 22, 719–724. <https://doi.org/10.1179/174328406X101328>.
- Compagnini, G., Foti, G., Reitano, R., Mondio, G., 1990. Graphitic clusters in hydrogenated amorphous carbon induced by keV-ion irradiation. *Appl. Phys. Lett.* 57, 2546–2548. <https://doi.org/10.1063/1.103832>.
- Daniels, C.A., 1989. *Polymers: Structure and Properties*. CRC Press, USA.
- Demina, T.S., Gilman, a.B., Akopova, T.a., Zelenetskii, a.N., 2014. Modification of the chitosan structure and properties using high-energy chemistry methods. *High Energy Chem.* 48, 293–302. <https://doi.org/10.1134/S0018143914050063>.
- Elliott, S., 1994. Frequency-dependent conductivity in ionically and electronically conducting amorphous solids. *Solid State Ionics* 70 (71), 27–40. [https://doi.org/10.1016/0167-2738\(94\)90284-4](https://doi.org/10.1016/0167-2738(94)90284-4).
- Fink, D., 2004. *Fundamentals of Ion-Irradiated Polymers*, Springer Series in Materials Science. Springer Berlin Heidelberg, Berlin, Heidelberg. <https://doi.org/10.1007/978-3-662-07326-1>.
- Fink, D., Chung, W.H., Klett, R., Schmoltdt, A., Cardoso, J., Montiel, R., Vazquez, M.H., Wang, L., Hosoi, F., Omichi, H., Goppelt-Langer, P., 1995a. Carbonaceous clusters in irradiated polymers as revealed by UV-Vis spectrometry. *Radiat. Eff. Defect Solid* 133, 193–208. <https://doi.org/10.1080/10420159508223990>.
- Fink, D., Chung, W.H., Wilhelm, M., 1995b. Damage of polyvinylalcohol by 16 MeV electrons. *Radiat. Eff. Defect Solid* 133, 209–215. <https://doi.org/10.1080/10420159508223991>.
- Fried, J.R., 2014. *Polymer Science and Technology*, third ed. Prentice Hall Press, USA.
- García, M.A., 2011. Surface plasmons in metallic nanoparticles: fundamentals and applications. *J. Phys. D Appl. Phys.* 44, 283001. <https://doi.org/10.1088/0022-3727/44/28/283001>.
- Gavade, C., Singh, N.L., Khanna, P.K., 2014. Optical and dielectric properties of ion beam irradiated Ag/polymethyl methacrylate nanocomposites. *J. Nanosci. Nanotechnol.* 14, 5911–5916. <https://doi.org/10.1166/jnn.2014.8736>.
- Gavade, C., Singh, N.L., Sharma, A., Khanna, P.K., Singh, F., 2011. The effect of SHI irradiation on structural, thermal and dielectric properties of a silver nanoparticle-embedded polystyrene matrix. In: *Radiation Effects and Defects in Solids*, pp. 585–591. <https://doi.org/10.1080/10420150.2011.579123>.
- Ghosal, K., Chandra, A., Praveen, G., Snigdha, S., Roy, S., Agatamor, C., Thomas, S., Proveznik, I., 2018. Electrospinning over solvent casting: tuning of mechanical properties of membranes. *Sci. Rep.* 8, 5058. <https://doi.org/10.1038/s41598-018-23378-3>.
- González-Campos, J.B., Mota-Morales, J.D., Kumar, S., Zárate-Triviño, D., Hernández-Iturriaga, M., Prokhorov, Y., Lepe, M.V., García-Carvajal, Z.Y., Sanchez, I.C., Luna-Bárceñas, G., 2013. New insights into the bactericidal activity of chitosan-Ag bionanocomposite: the role of the electrical conductivity. *Colloids Surf. B Biointerfaces* 111, 741–746. <https://doi.org/10.1016/j.colsurfb.2013.07.003>.
- González-Campos, J.B., Prokhorov, E., Luna-Bárceñas, G., Sanchez, I.C., Lara-Romero, J., Mendoza-Duarte, M.E., Villaseñor, F., Guevara-Olvera, L., 2010. Chitosan/silver nanoparticles composite: molecular relaxations investigation by dynamic mechanical analysis and impedance spectroscopy. *J. Polym. Sci., Part B: Polym. Phys.* 48, 739–748. <https://doi.org/10.1002/polb.21941>.
- Hnatowicz, V., 1999. Simple model of radial structure of latent tracks in polymers. *Phys. Status Solidi* 216, 931–941. [https://doi.org/10.1002/\(SICI\)1521-3951\(199912\)216:2<931::AID-PSSB931>3.0.CO;2-I](https://doi.org/10.1002/(SICI)1521-3951(199912)216:2<931::AID-PSSB931>3.0.CO;2-I).
- Huheey, J.E., Keiter, E.A., Keiter, R.L., 1993. *Inorganic Chemistry: Principles of Structure and Reactivity*, fourth ed. PEARSON. HarperCollins College Publishers, New York.

- Jonscher, A.K., 1996. *Universal Relaxation Law: a Sequel to Dielectric Relaxation in Solids*. Chelsea Dielectrics Press.
- Karak, N., 2019. Fundamentals of nanomaterials and polymer nanocomposites. In: *Nanomaterials and Polymer Nanocomposites*. Elsevier, pp. 1–45. <https://doi.org/10.1016/B978-0-12-814615-6.00001-1>.
- Kemp, W., 1991. *Organic Spectroscopy*. Macmillan Education UK, London. <https://doi.org/10.1007/978-1-349-15203-2>.
- Koev, S.T., Dykstra, P.H., Luo, X., Rubloff, G.W., Bentley, W.E., Payne, G.F., Ghodssi, R., 2010. Chitosan: an integrative biomaterial for lab-on-a-chip devices. *Lab Chip* 10, 3026. <https://doi.org/10.1039/c0lc00047g>.
- Kowalonek, J., 2017. Surface and thermal properties of UV-irradiated chitosan/poly (ethylene oxide) blends. *J. Photochem. Photobiol. Chem.* 348, 209–218. <https://doi.org/10.1016/j.jphotochem.2017.08.035>.
- Ku, C.C., Liepins, R., 1987. *Electrical Properties of Polymers*. Hanser Publishers, New York.
- Kumar-Krishnan, S., Prokhorov, E., Hernández-Iturriaga, M., Mota-Morales, J.D., Vázquez-Lepe, M., Kovalenko, Y., Sanchez, I.C., Luna-Bárceñas, G., 2015. Chitosan/silver nanocomposites: synergistic antibacterial action of silver nanoparticles and silver ions. *Eur. Polym. J.* 67, 242–251. <https://doi.org/10.1016/j.eurpolymj.2015.03.066>.
- Kumar-Krishnan, S., Prokhorov, E., Ramírez, M., Hernandez-Landaverde, M.A., Zarate-Triviño, D.G., Kovalenko, Y., Sanchez, I.C., Méndez-Nonell, J., Luna-Bárceñas, G., 2014. Novel gigahertz frequency dielectric relaxations in chitosan films. *Soft Matter* 10, 8673–8684. <https://doi.org/10.1039/C4SM01804D>.
- Kumar, V., Sonkawade, R.G., Chakarvarti, S.K., Kulriya, P., Kant, K., Singh, N.L., Dhaliwal, A.S., 2011. Study of optical, structural and chemical properties of neutron irradiated PADC film. *Vacuum* 86, 275–279. <https://doi.org/10.1016/j.vacuum.2011.07.001>.
- Mishra, Y.K., Mohapatra, S., Chakravadhanula, V.S.K., Lalla, N.P., Zaporozhchenko, V., Avasthi, D.K., Faupel, F., 2010. Synthesis and characterization of Ag-polymer nanocomposites. *J. Nanosci. Nanotechnol.* 10, 2833–2837. <https://doi.org/10.1166/jnn.2010.1449>.
- Mortazavian, H., Fennell, C.J., Blum, F.D., 2016. Structure of the interfacial region in adsorbed poly(vinyl acetate) on silica. *Macromolecules* 49, 298–307. <https://doi.org/10.1021/acs.macromol.5b02214>.
- Moura, D., Mano, J.F., Paiva, M.C., Alves, N.M., 2016. Chitosan nanocomposites based on distinct inorganic fillers for biomedical applications. *Sci. Technol. Adv. Mater.* 17, 626–643. <https://doi.org/10.1080/14686996.2016.1229104>.
- Murugaraj, P., Mainwaring, D.E., Tonkin, D.C., Al Kobaisi, M., 2011. Probing the dynamics of water in chitosan polymer films by dielectric spectroscopy. *J. Appl. Polym. Sci.* 120, 1307–1315. <https://doi.org/10.1002/app.33163>.
- Nogales, A., Ezquerro, T.A., Rueda, D.R., Martínez, F., Retuert, J., 1997. Influence of water on the dielectric behaviour of chitosan films. *Colloid Polym. Sci.* 275, 419–425. <https://doi.org/10.1007/s003960050099>.
- Pal, B., Yang, S., Ramesh, S., Thangadurai, V., Jose, R., 2019. Electrolyte selection for supercapacitive devices: a critical review. *Nanoscale Adv* 1, 3807–3835. <https://doi.org/10.1039/C9NA00374F>.
- Parak, W.J., Manna, L., Simmel, F.C., Gerion, D., Alivisatos, P., 2005. Quantum dots. In: *Nanoparticles*. Wiley-VCH Verlag GmbH & Co. KGaA, Weinheim, FRG, pp. 4–49. <https://doi.org/10.1002/3527602399.ch2>.
- Patel, G.B., Bhavsar, S., Singh, N.L., Singh, F., Kulriya, P.K., 2016. SHI induced modification in structural, optical, dielectric and thermal properties of poly ethylene oxide films. *Nucl. Instrum. Methods Phys. Res. Sect. B Beam Interact. Mater. Atoms* 379, 156–161. <https://doi.org/10.1016/j.nimb.2016.04.018>.
- Patel, G.B., Singh, N.L., Singh, F., 2017. Modification of chitosan-based biodegradable polymer by irradiation with MeV ions for electrolyte applications. *Mater. Sci. Eng. B* 225, 150–159. <https://doi.org/10.1016/j.mseb.2017.08.023>.
- Patel, G.B., Singh, N.L., Singh, F., Kulriya, P.K., 2019. Effects of MeV ions on physicochemical and dielectric properties of chitosan/PEO polymeric blend. *Nucl. Instrum. Methods Phys. Res. Sect. B Beam Interact. Mater. Atoms* 447, 68–78. <https://doi.org/10.1016/j.nimb.2019.03.052>.
- Persson, B.N.J., 1993. Polarizability of small spherical metal particles: influence of the matrix environment. *Surf. Sci.* 281, 153–162. [https://doi.org/10.1016/0039-6028\(93\)90865-H](https://doi.org/10.1016/0039-6028(93)90865-H).
- Piroonpan, T., Katemake, P., Pasanphan, W., 2020. Comparative study of different chitosan solutions to assist the green synthesis of gold nanoparticles under irradiation. *Radiat. Phys. Chem.* 169, 108250. <https://doi.org/10.1016/j.radphyschem.2019.03.054>.
- Prakash, J., Kumar, V., Kroon, R.E., Asokan, K., Rigato, V., Chae, K.H., Gautam, S., Swart, H.C., 2016. Optical and surface enhanced Raman scattering properties of Au nanoparticles embedded in and located on a carbonaceous matrix. *Phys. Chem. Chem. Phys.* 18, 2468–2480. <https://doi.org/10.1039/c5cp06134b>.
- Prokhorov, E., Luna-Bárceñas, J.G., González-Campos, J.B., Sanchez, I.C., 2011. Conductivity mechanisms in a composite of chitosan-silver nanoparticles. *Mol. Cryst. Liq. Cryst.* 536 <https://doi.org/10.1080/15421406.2011.538327>, 24/[256]-32/[264].
- Psarras, G.C., 2010. Conductivity and dielectric characterization of polymer nanocomposites. In: *Physical Properties and Applications of Polymer Nanocomposites*. Elsevier, pp. 31–69. <https://doi.org/10.1533/9780857090249.1.31>.
- Qureshi, A., Singh, N.L., Shah, S., Kulriya, P., Singh, F., Avasthi, D.K., 2008. Modification of polymer composite films using 120MeV Ni¹⁰⁺ ions. *Nucl. Instrum. Methods Phys. Res. Sect. B Beam Interact. Mater. Atoms* 266, 1775–1779. <https://doi.org/10.1016/j.nimb.2008.01.057>.
- Sadasivuni, K.K., Ponnamma, D., Kim, J., Cabibihan, J.J., AlMaadeed, M.A., 2017. Biopolymer Composites in Electronics, *Biopolymer Composites in Electronics*. Elsevier. <https://doi.org/10.1016/C2014-0-04575-3>.
- Sakurai, K., 2000. Glass transition temperature of chitosan and miscibility of chitosan/poly(N-vinyl pyrrolidone) blends. *Polymer* 41, 7051–7056. [https://doi.org/10.1016/S0032-3861\(00\)00067-7](https://doi.org/10.1016/S0032-3861(00)00067-7).
- Singh, N.L., Qureshi, A., Singh, F., Avasthi, D.K., 2007. Effect of swift heavy ion irradiation on dielectrics properties of polymer composite films. *Mater. Sci. Eng. B* 137, 85–92. <https://doi.org/10.1016/j.mseb.2006.10.013>.
- Singh, N.L., Shah, S., Qureshi, A., Tripathi, A., Singh, F., Avasthi, D.K., Raole, P.M., 2011. Effect of ion beam irradiation on metal particle doped polymer composites. *Bull. Mater. Sci.* 34, 81–88. <https://doi.org/10.1007/s12034-011-0040-5>.
- Singhal, P., Rattan, S., 2016. Swift heavy ion irradiation as a tool for homogeneous dispersion of nanographite platelets within the polymer matrices: toward tailoring the properties of PEDOT:PSS/nanographite nanocomposites. *J. Phys. Chem. B* 120, 3403–3413. <https://doi.org/10.1021/acs.jpcc.5b11240>.
- Steinmetz, C.P., 2012. Fundamentals of electrochemical impedance spectroscopy. In: *Impedance Spectroscopy*. John Wiley & Sons, Inc., Hoboken, NJ, USA, pp. 1–21. <https://doi.org/10.1002/9781118164075.ch1>.
- Tauc, J., Grigorovici, R., Vancu, A., 1966. Optical properties and electronic structure of amorphous germanium. *Phys. Status Solidi* 15, 627–637. <https://doi.org/10.1002/pssb.19660150224>.
- Wang, B., Huang, W., Chi, L., Al-Hashimi, M., Marks, T.J., Facchetti, A., 2018. High-*k* gate dielectrics for emerging flexible and stretchable electronics. *Chem. Rev.* 118, 5690–5754. <https://doi.org/10.1021/acs.chemrev.8b00045>.
- Wang, S., Shen, L., Zhang, W., Tong, Y., 2005. Preparation and mechanical properties of chitosan/carbon nanotubes composites. *Biomacromolecules* 6, 3067–3072. <https://doi.org/10.1021/bm050378v>.
- Wei, D., Qian, W., 2008. Facile synthesis of Ag and Au nanoparticles utilizing chitosan as a mediator agent. *Colloids Surf. B Biointerfaces* 62, 136–142. <https://doi.org/10.1016/j.colsurfb.2007.09.030>.
- Williams, G., Watts, D.C., 1970. Non-symmetrical dielectric relaxation behaviour arising from a simple empirical decay function. *Trans. Faraday Soc.* 66, 80. <https://doi.org/10.1039/tf9706600080>.
- Yomota, C., Miyazaki, T., Okada, S., 1993. Determination of the viscometric constants for chitosan and the application of universal calibration procedure in its gel permeation chromatography. *Colloid Polym. Sci.* 271, 76–82. <https://doi.org/10.1007/BF00652306>.
- Ziegler, J.F., Ziegler, M.D., Biersack, J.P., 2010. Srim – the stopping and range of ions in matter (2010). *Nucl. Instrum. Methods Phys. Res. Sect. B Beam Interact. Mater. Atoms* 268, 1818–1823. <https://doi.org/10.1016/j.nimb.2010.02.091>.
- Zojer, E., Taucher, T.C., Hofmann, O.T., 2019. The impact of dipolar layers on the electronic properties of organic/inorganic hybrid interfaces. *Adv. Mater. Interfaces* 6, 1900581. <https://doi.org/10.1002/admi.201900581>.



Effects of MeV ions on physicochemical and dielectric properties of chitosan/PEO polymeric blend

Gnansagar B. Patel^a, N.L. Singh^{a,*}, Fouran Singh^b, P.K. Kulriya^b

^a Department of Physics, Faculty of Science, The M. S. University of Baroda, Vadodara 390002, India

^b Inter University Accelerator Centre, Aruna Asaf Ali Marg, New Delhi 110067, India

ARTICLE INFO

Keywords:

Chitosan/PEO blend
SHI irradiation
Structural properties
Optical properties
Dielectric properties

ABSTRACT

In the present investigation, the effects of ion beam irradiations on physicochemical and dielectric properties of the self-sustained chitosan/poly (ethylene oxide) blend film was studied. The blend film was formed via solution casting route due to its cost-effectiveness and ease of processing. These polymeric blend films were irradiated with C^{+5} (60 MeV) and Ni^{+7} (100 MeV) ions at different fluences. The tailored responses of polymeric material depend on electronic energy loss (S_e) of the ions. The electronic energy loss within the matrix depends on mass, energy and atomic number of the impinging ion. XRD and FTIR analyses revealed alterations of crystalline size and diminished diverse modes of molecular vibration, respectively. Optical parameters were analyzed by employing Tauc and Fink approaches and unveiling the waning in band gap, carbonization of the polymeric matrix, respectively. The physicochemical modifications were well correlated with frequency dependent dielectric properties in the broad interval ranging from 20 Hz to 2 MHz. It reveals a significant enhancement in the dielectric outcomes owing to structural rearrangements upon a radiation treatment. Moreover, the XRD and FTIR studies were well complemented by DSC analysis. Observation of the hillocks-like structures and alteration of surface roughness upon exposure to radiation were examined by employing AFM.

1. Introduction

Global climate changes are a worrying environmental issue, affecting current and forthcoming deeds. Everyday uses of traditional polyethylene products are one of the major cause of climate change, owing to their non-biodegradable characteristics, challenging waste management to develop eco-friendly and low-cost solid waste disposal [1]. Therefore being necessitated to replace conventional polymeric materials with sustainable, biodegradable and renewable resource-based materials [2]. To diminish the adverse environmental impacts, the use of the biodegradable polymer is quite fascinating.

Chitosan is a cationic biopolymer with functional groups amino ($-NH_2$) and hydroxyl ($-OH$) with captivating physicochemical features viz. nontoxicity, biodegradability, biocompatibility, antibacterial, and film forming capacity, which intensifies its relevance in food, medical, pharmaceutical, agricultural, and optoelectronics industries [3]. The physicochemical property of chitosan yields flexible and permeable film due to stabilized hydrogen bond network. To develop the new class of biomaterials with optimized properties for an explicit desire in various applications is *blending* of biodegradable polymers [3,4]. In addition, the polymeric blend can be formed using an easy route. Chitosan is

being blended with other polymeric materials, in order to expand the horizon of its applications [2,4,5]. Among these, poly (ethylene oxide) (PEO) with ether groups is emerged as an ensuring one, owing to uncharged, semi-crystalline, biodegradable, nontoxic, and water-soluble polymer. Particularly, PEO is broadly used in biomedical, pharmaceutical sectors as well as solid polymer electrolytes (SPEs) used in the innovation of electronic techniques in batteries, fuel cell, super-capacitors [5–7]. Although such advantages, self-standing PEO films exhibited low flexibility and weak mechanical properties owing to semi-crystalline nature [5]. The presence of chitosan within PEO matrix enhanced its physical, optical and dielectric properties. Moreover, proton donor amino group of chitosan effectively interact with proton acceptor ether group of PEO yielding homogeneous, flexible and optically improved polymeric blend [7,8]. It revealed significant interactions between the amino groups and the ether groups of chitosan and PEO respectively. Chitosan/PEO (CP) blend is a polymeric material with unique and enhanced performance over their individual shortcomings. CP blend does not lead to phase separation and amorphous chitosan chains may facilitate a decrease in PEO crystallinity [5]. Also, it tends to improve in dielectric and optical properties of the materials which can be used in various electrochemical applications because

* Corresponding author.

E-mail address: nl.singh-phy@msubaroda.ac.in (N.L. Singh).

<https://doi.org/10.1016/j.nimb.2019.03.052>

Received 27 December 2018; Received in revised form 14 March 2019; Accepted 23 March 2019

Available online 28 March 2019

0168-583X/ © 2019 Elsevier B.V. All rights reserved.

conductivity is significant in the amorphous state [9].

Zivanovic et al. [5] studied physical, mechanical, and antibacterial properties of CP blend. Li et al. [10] reported the functionality of CP films with respect to film thickness, composition and synthesis methods. Shukur et al. [6] studied the conductivity of ammonium nitrate doped CP blend base electrolytes for electrochemical devices applications. Cassani et al. [11] explored the physicochemical and nano-mechanical properties of electrodeposited CP blend. Buraidah et al. [7] investigated ammonium iodide embedded CP blend for plasmonic dye-sensitized solar cell. To date, enormous efforts have been made to improve the CP blend as a function of different variables depending on the required applications [5,7,10,11]. However, the chemical modification involves complicated methodology and the subsequent yielding explanation became difficult due to involvements of many parameters.

An alternative and facile technique to modify the physicochemical responses of the biodegradable blend by electromagnetic (e.g. UV, X-ray or Gamma photons) or particle (electron, neutron or charged species) induced irradiation in a well-controlled manner. Kowalonek [12] recently reported the surface and thermal properties of UV-irradiated chitosan/poly (ethylene oxide) blends. However, the deposited localized energy density to the matrix by UV radiation is rather small and hence it may transform the materials up to a certain extent through photooxidative degradation. Swift heavy ions (SHIs) modify the polymeric matrices by depositing extremely high localized energy density within a very small volume ($\sim 10^{-17}$ to 10^{-16} cm³), in a very short time ($\sim 10^{-17}$ to 10^{-15} s) [13]. The influence depends upon ion range, electronic energy loss (S_e) and diameter of ion track, can be regulated by informed selection of the energy, mass, and fluence of the SHIs. To the extent, the influence of SHIs irradiation on the subsequent structural, optical, dielectric, and surface properties of CP blend have not yet been investigated although their relevance toward high-end applications in medical and electrochemical devices [5–7,10]. The objective of this work is to investigate the effect of electronic energy loss, fluence and mass of MeV ions, i.e. C⁺⁵ (Z = 6) and Ni⁺⁷ (Z = 28) on physicochemical and dielectric responses of CP blend.

2. Experimental

2.1. Materials

Commercially available 50–190 kDa molecular weight and 75–85% deacetylated chitosan powder (CAS No. 9012-76-4) and 300 kDa molecular weight PEO powder (CAS No. 25322-68-3) were purchased from Sigma-Aldrich and Alfa Aesar respectively. Acetic acid (ACS reagent, $\geq 99.7\%$, CAS No. 64-19-7) procured from Sigma-Aldrich was used as a solvent.

2.2. Preparation of CP blend films

A film-forming solution of CP blend was prepared by a solution casting technique. Initially, to obtain the film with a desired thickness, an equal amount of chitosan and PEO powder were diluted separately in 1.0% glacial acetic acid using stirrer and to obtain a homogeneous film-forming solution at ambient temperature. They were filtrated and poured into a beaker for further vigorous stirring followed by half an hour sonication. To obtain a self-standing film of thickness about ~ 80 μ m, the sonicated film-forming solution was poured into a well levelled and cleaned Teflon petri dish at room temperature. Finally, the desiccated film was detached and conditioned in desiccators.

2.3. SHI irradiation of CP blend films

The desiccated CP blend film was carefully cut into the units of area 1.5×1.5 cm². These films were affixed on a vertically portable copper ladder and irradiated under a high vacuum by C⁺⁵ (60 MeV) and Ni⁺⁷ (100 MeV) ions, at fluences of 1×10^{11} and 1×10^{12} ions/cm²,

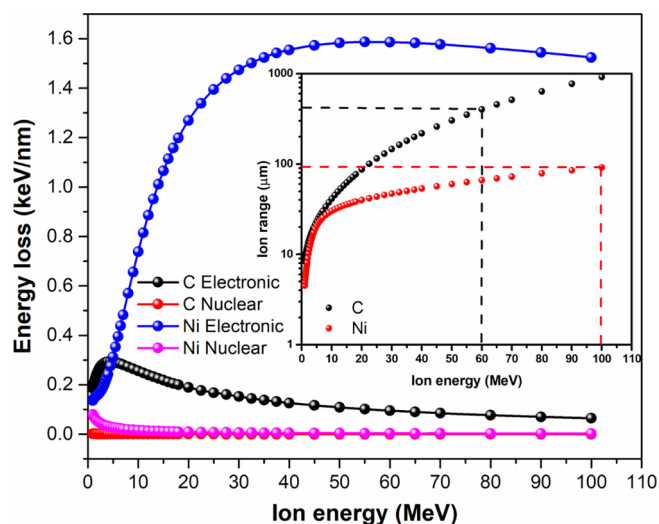


Fig. 1. Electronic and nuclear energy loss in CP blend. Inset shows the penetration depth of 60-MeV C⁺⁵ and 100-MeV Ni⁺⁷ ions as a function of energy in CP blend.

accessible at the Inter University Accelerator Centre (IUAC), New Delhi, India from 15 UD Tandem Pelletron Accelerator amenity. Pre-loaded self-supported films were uniformly irradiated in x-y coordinate of area 1×1 cm², utilizing magnetic scanning system. C⁺⁵ and Ni⁺⁷ ions beam current were kept ~ 0.5 particle nano-ampere (pnA) to prevent the thermal decomposition in CP blend films [14,15].

2.4. Energy loss and range of C⁺⁵ and Ni⁺⁷ ions in CP blend films

C⁺⁵ and Ni⁺⁷ ions undergo electronic energy loss (S_e) and nuclear energy loss (S_n) during the interaction with the polymeric materials along its trajectory. As shown in Fig. 1 and its inset, the values of S_e , S_n and ranges of C⁺⁵ and Ni⁺⁷ ions in CP blend matrix were simulated using SRIM 2013 code [16]. The S_e value was found to be 0.095 keV/nm and 1.5 keV/nm; while S_n value was 0.000 keV/nm and 0.002 keV/nm, and simulated range was 403 μ m and 92 μ m for C⁺⁵ and Ni⁺⁷ ions, respectively. It should be noted that S_n value for both the ions seems to be diminutive than S_e values. Moreover, the electronic energy loss is substantial and hundred times higher for Ni⁺⁷ than C⁺⁵. The range of ions revealed that the possibility of ions implantation was moderately trivial.

2.5. Characterizations of CP blend films

To investigate the tailored physicochemical characteristics of CP blend, we exploited X-ray diffraction (XRD), FTIR and UV-visible, three powerful techniques. Modified structural responses of CP blend were monitored by XRD with an X-ray source of monochromic Cu-K α having wavelength of 1.5418 Å (Bruker D8-Advance diffractometer). ATR-FTIR spectra were executed in 4000–800 cm⁻¹ interval to analyze the vibrational functional modes (JASCO-4100 spectrometer). Each spectrum obtained after 100 sequential scans to confirm a higher signal-to-noise ratio in multi-reflection ATR mode (ATR PRO410-M). The optical response in absorption mode was explored in 200–800 nm wavelength region (Hitachi Model U-3300 spectrometer). The impedance behavior performed by using a precision LCR meter in the broader frequency range of 20 Hz–2 MHz at room temperature (Agilent E4980A). The differential scanning calorimetry (DSC) was investigated using 2 mg segment of the CP blend under the dynamic N₂ gas environment at flow rate of 60 ml/min by heating at the rate of 10 °C/min (SII EXSTAR 6000). Atomic Force Microscopic (AFM) images were used to investigate the surface morphology and roughness, recorded in the air at ambient temperature (AFM Nanoscope digital instruments, Canberra, USA).

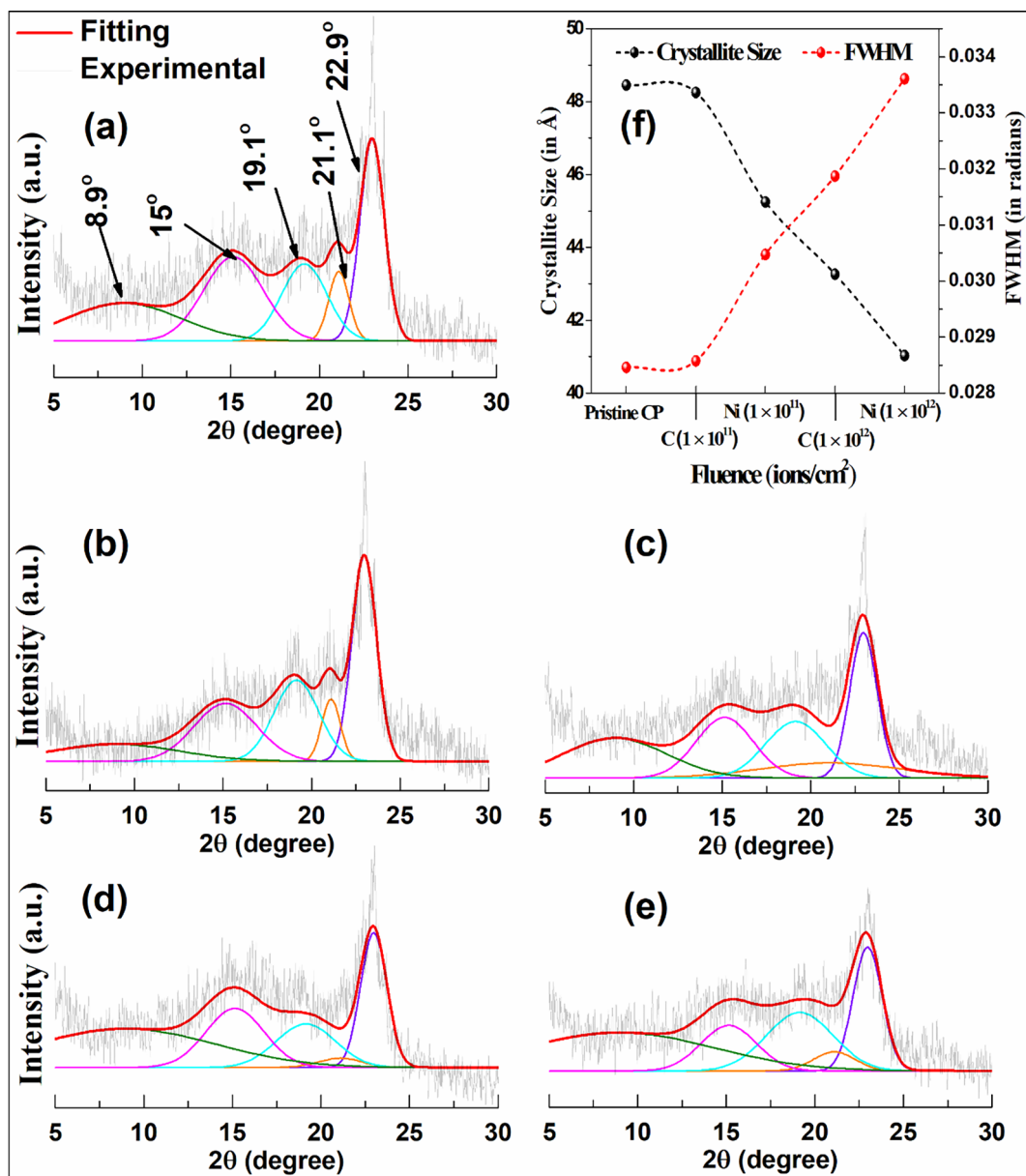


Fig. 2. XRD of (a) pristine CP blend, and irradiated with (b) C^{+5} ions at the fluence of 1×10^{11} ions/cm², (c) C^{+5} ions at the fluence of 1×10^{12} ions/cm², (d) Ni^{+7} ions at the fluence of 1×10^{11} ions/cm², (e) Ni^{+7} ions at the fluence of 1×10^{12} ions/cm², and (f) variation in crystallite size and FWHM as a function ion fluences.

3. Results and discussion

3.1. XRD analysis

The XRD patterns obtained for C^{+5} and Ni^{+7} ions irradiated CP blend films are shown in Fig. 2(a–f) to infer the structural alteration. To detach the probable overlapping peaks in CP blend matrix, the deconvolution method was employed. The peaks appeared at 2-theta value of 8.9°, 15° and 21.1° were identified as hydrated crystalline, anhydrous crystalline and amorphous form of chitosan [15]. The intense and sharp peaks at 2-theta value of 19.1° and 22.9° 2 θ were attributed to PEO crystalline phase [14]. The same positions of peaks coming from chitosan and PEO in the blend compared to these peak positions for pure polymers, observed in XRD spectra, suggests the weak or lack of interactions between the components in the blend. The existence of chitosan in the blend will lead to regulate the crystallization of the PEO and enhance the mobility of polymeric chains within the blend matrix, and enhanced the optical and dielectric responses. The FWHM of the

peak was attained by deconvolution technique and used to estimate the crystallite size (L) using the Scherrer's formula, $L = 0.89\lambda/\beta_{1/2} \cos\theta$, where $\beta_{1/2}$ is FWHM of the peak at $2\theta = 22.9^\circ$.

As presented in Fig. 2(f) and tabulated in Table 1, the FWHM was moderately increased by 15.3% and profoundly achieved greater values for higher fluence and heavier ion irradiation with negligible deviation in 2θ . The crystallite size was explicitly decreased by 10.7% due to localize melting taking place at the surface and nearby province of the cylindrical latent track of ions within the matrix. Hence, the segmental motion within the molten zones considerably enhanced nearby the ions trajectory and caused randomization of macromolecular chains by re-orientation along with increased nano-scale free volume.

3.2. FTIR analysis

Fig. 3(a) shows the allocation of the vibrational modes of pristine CP blend. The broader vibrational modes in range of 3000–3600 cm⁻¹ attributed to hydrogen bonded O–H and N–H groups and also O–H/

Table 1

Variation of FWHM, crystallite size, optical energy band gap (E_g), the number of carbon atoms per conjugation length (N) and R^2 for pristine and irradiated CP blend with 60-MeV C^{+5} and 100-MeV Ni^{+7} ions at the fluence of 1×10^{11} and 1×10^{12} ions/cm², respectively.

Sample	FWHM (in radians)	Crystallite Size (in Å)	E_g (eV)	N	R^2
Pristine CP	0.0285	48.45	5.40 ± 0.01	40.40	0.97
C (1×10^{11} ions/cm ²)	0.0286	48.25	5.19 ± 0.02	43.67	0.95
C (1×10^{12} ions/cm ²)	0.0319	43.27	3.92 ± 0.04	76.72	0.93
Ni (1×10^{11} ions/cm ²)	0.0305	45.25	4.54 ± 0.03	56.96	0.96
Ni (1×10^{12} ions/cm ²)	0.0336	41.03	3.23 ± 0.02	112.86	0.95

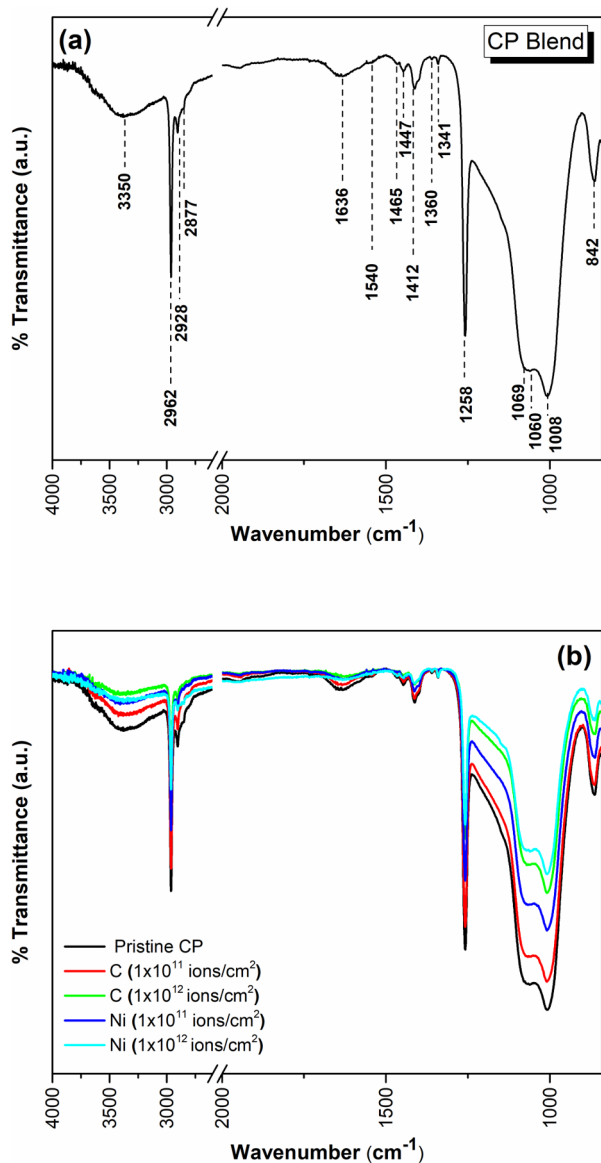


Fig. 3. FTIR spectra of (a) pure CP blend, (b) CP blend irradiated with 60-MeV C^{+5} and 100-MeV Ni^{+7} ions at the fluence of 1×10^{11} and 1×10^{12} ions/cm², respectively.

N–H interacting with oxygen from C=O group of chitosan [17]. The vibrational modes for chitosan observed at 1258 cm^{-1} (OH bending), 1636 cm^{-1} (C=O stretching (amide I)) and 1540 cm^{-1} (NH bending (amide II)). The modes at wave number 1008 cm^{-1} and 1069 cm^{-1} attributed to the saccharide structure of chitosan. The fundamental

modes of PEO appeared at 842 cm^{-1} (CH_2 rocking), 1341 cm^{-1} and 1360 cm^{-1} (CH_2 wagging) and 1060 cm^{-1} (C–O–C stretching) [18]. The ATR-FTIR spectrum exhibits vibrational groups at 1412 cm^{-1} (CH_2 bending and CH_3 deformation), 1447 cm^{-1} and 1465 cm^{-1} (CH_2 scissoring), 2877 cm^{-1} , 2928 cm^{-1} and 2962 cm^{-1} (CH stretching). The vibrational bands of the prepared blend were well consistent with previous investigations [14,15]. However, a trivial shift in some vibrational bands appeared in CP blend imply feeble interactions between molecules of two polymers, probably mainly at the interphase.

The exploration of FTIR spectra of radiation exposed CP blend (Fig. 3(b)) revealed no noticeable shift in peak position. However, the intensities of bands corresponding to all the vibrational modes decreased. These results imply the intense materials reforms by 60-MeV C^{+5} and 100-MeV Ni^{+7} ions, which lose their energy predominantly through electronic ionization having an order of few keV/nm as stated from SRIM analysis. Moreover, it is dominant at fluence of 1×10^{12} ions/cm² for nickel ion. Since, the S_e value is very high and efficient to break entire linkages within a few nanometres along the trajectory of the ions, which yields an overall fall of the intensities corresponding to all the vibrational bands. This confirms randomization of macromolecular chains, explicitly, the long chains cleave, degradation at backbones and side-chains of the macromolecular structure through extrication of hydrogen and carbon. The hydrogen ravage is more than carbon. Also, there will be the creation of ions and radicals, which may become a part of bulk or leave the host owing to high vacuum [9,14,15,19]. The authentic controlled alteration in macroscopic characteristic will boost optical and dielectric responses of the biodegradable blend and can be relevant in wide-ranging utilizations.

3.3. Optical analysis

The optical responses of the radiation treated polymeric materials are very imperative for their optoelectronic applications. Fig. 4(a) shows optical absorption data upon ions irradiations collectively for comparison and revealed noteworthy alterations. Pristine CP blend shows minimum absorption in 400–800 nm (i.e. visible range) indicates the completely bound state of electrons [20] in the matrix. After SHIs irradiations, absorption intensity increases in the UV region with fluence for both the ions. Also, at an ion fluence of 1×10^{12} ions/cm² for both ions, the absorption is significantly higher in UV region (i.e. < 370 nm), indicating shielding of UV photons. These results ascribed to transformation in color of bulk materials (images not shown here) owing to the creation of color sensitive conjugated linkage upon irradiations. As a result of it, π electrons can able to excite and change the color of materials [21]. Another assuring reason for coloration is rupture of C–C bonds of polymeric chains, which will lead to sp^2 hybridization plus an increase in charge density (i.e. radicals and ions formation within the matrix). In addition, there are no absorption bands in UV–Vis spectrum of the pristine CP blend. But after SHI treatment, a new band appeared at about 310 nm, which can be assigned to new chromophores C=C, C=O. After SHI irradiation, this peak became instance and broader revealed sp^2 hybridization due to H abstraction along with volatile outgassing. The absorption edge of the post-irradiated films became wider and persist red shift. These results ascribed to complex phenomenon involving structural alteration through destroying characteristic polymeric linkages and randomization of the macromolecular chains (as examined from XRD and FTIR data) [9,14,15,19,21]. The variation in optical responses is understood by means of optical band gap (E_g) and carbonaceous cluster evolution by Tauc [22] and Fink [23] approaches, respectively.

The Tauc's plots are shown in Fig. 4(b) and obtained values of E_g are listed in Table 1 with standard deviation and respective R^2 values. The values of R^2 indicates a reliable linear fitting of the Tauc's plots to evaluate E_g . The decreasing tendency in E_g upon irradiation is observed owing to band edge alteration and/or creation of intermediate energy level in forbidden gap and enrichment in localized charge carrier

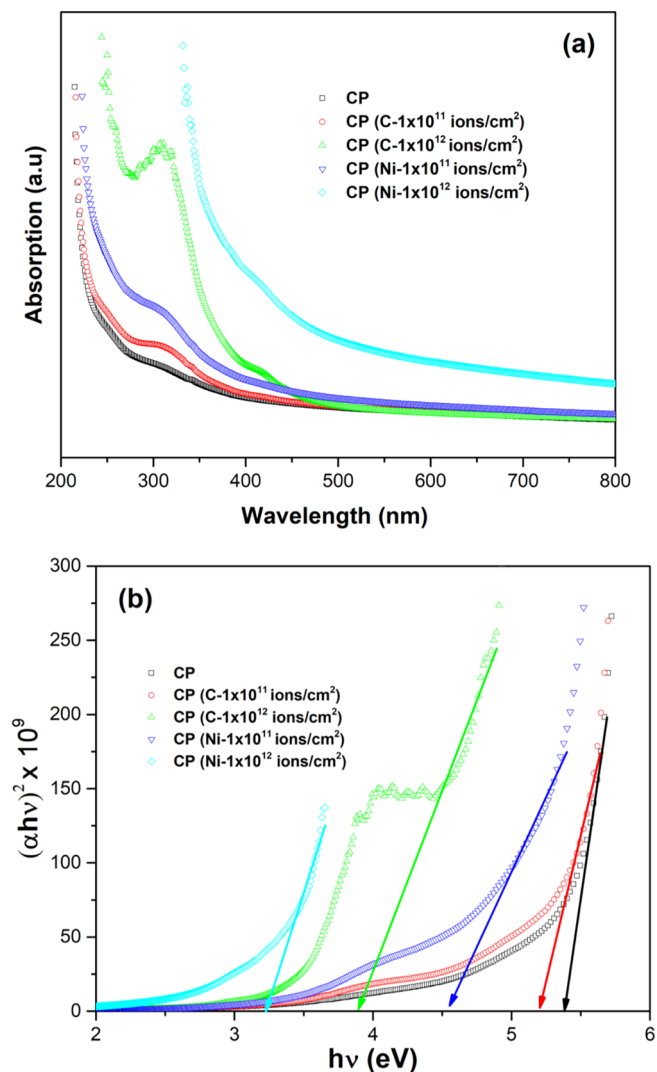


Fig. 4. (a) UV-Vis spectrum of CP blend irradiated with 60-MeV C $^{+5}$ and 100-MeV Ni $^{+7}$ ions at the fluence of 1×10^{11} and 1×10^{12} ions/cm 2 , respectively, and (b) Tauc's plot for all the CP blend samples.

density as a result of structural rearrangement [15,21]. Diminishing in E_g due to low energetic and lighter C-ion is $\sim 27\%$, whereas for highly energetic and heavier Ni-ion is $\sim 40\%$. That is, decrease in E_g due to Ni-ion is $\sim 17\%$ greater than C-ion due to extremely high electronic loss of Ni-ion cause a noteworthy impact on polymeric materials.

Fink *et al.* [23] assumed the hydrogenated amorphous carbon clusters structure formed within the polymer matrix upon SHI irradiation as C $_{60}$. The number of carbon atoms per conjugation length (N) was studied using Fink methodology [23] and listed in Table 1. Upon increasing ion fluence, the values of N goes on increasing. Also, N values are significantly high for Ni-ion owing to substantial dehydrogenation than C-ion along with an alteration in the grain structure of polymeric materials [24]. Fig. 5 exhibits the E_g and N values vs. ions fluence used for irradiations. It illustrated that the E_g decreased and N value increased as a function of ion fluence. This effect leads to modification in optical property yielding a noteworthy impact on dielectric responses of the materials.

3.4. AC electrical frequency response

Dielectric response of polymeric materials as a function of frequency investigated by the atomic, electronic, interfacial and orientation polarizations of the macromolecules. The dielectric constant (ϵ') vs. log

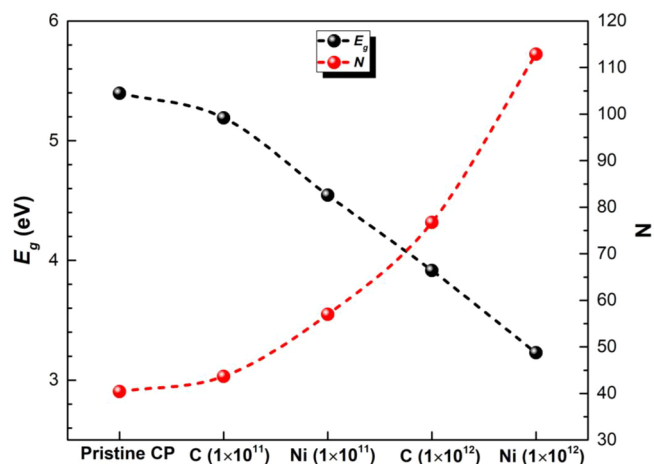


Fig. 5. Variation in band gap and number of carbon atoms per conjugation length as a function ion fluence.

frequency is plotted in Fig. 6 for all the samples under investigations. At first sight, the patterns of pristine and radiation treated CP blend appeared identical and show a broad dispersion in frequency from 20 Hz to 4 kHz. Also, ϵ' exhibits greater value at low frequency region, while inferior value at high frequency region. The trends observed for frequency of less than 4 kHz is due to electrical double layer creation (i.e. space charge/interfacial polarization) at boundaries of polymer and electrode [8]. This occurrence is endorsed to the following response of the dipoles exist due to $-\text{NH}_2$ and $-\text{O}-$ groups as well as long-range drift of free radicals due to a slower rate of varying electric field at low frequency. The ϵ' response decreased beyond 7 kHz frequency owing to a reduction in charge carrier density at the interface because of short-range drift of charge carriers and slower response of polymeric dipoles with a large moment of inertia to prompt electric field at high frequency [8,25]. Due to the effects of SHI irradiation, the overall value of ϵ' increased. The increased value at low frequency ascribed to the creation of low molecular polymeric macromolecules as revealed by FTIR data. Because their moment of inertia decreased and hence they can easily be aligned in the direction of the electric field. While the increased ϵ' at higher frequency is attributed to increased charge carrier density and defect sites upon irradiation as discuss in optical response.

Dielectric modulus over a wide frequency range gives an adequate perception of relaxation and conduction phenomenon via minimizing space charge effect at low frequency. To overcome some difficulties viz. nature of the electrode, electrical contact between electrode and specimen, absorbed impurities etc. occurring during the investigation of the dielectric spectra can be ceased in the electric modulus spectra [25]. Figs. 7 and 8 show frequency-dependent plots of the real modulus (M') and imaginary modulus (M'') respectively for pristine and irradiated films. As the frequency $f \rightarrow 0$, the real modulus $M' \rightarrow 0$, which is attributed to space charge polarisation ceases at low frequency. For an ion fluence of 1×10^{12} ions/cm 2 for both ions, the values of M' at higher frequency seems to be reduce which indorsed the increased free volume (as revealed by XRD analysis) and formation of low molecular segment owing to abstraction occurred at polymeric backbones and side-chains (as revealed by FTIR). Accordingly, there is a reduction in moment of inertia or rigidity of polymer chains may enhance the chain segmental and charge carriers mobility. As expected, two distinct relaxation observed in the plot of $M'' \rightarrow \log f$ due to the coexistence of semi-crystalline and amorphous phase in the CP blend. The relaxation at lower frequency revealed the transformation of long-range motion to rotational or segmental motion of charge carriers, while the faster relaxation at higher frequency attributed to polar side group motion [26]. In case of post-radiated films, as fluence and energy of incident ions increased, the relaxation peak at a lower frequency shifted towards higher

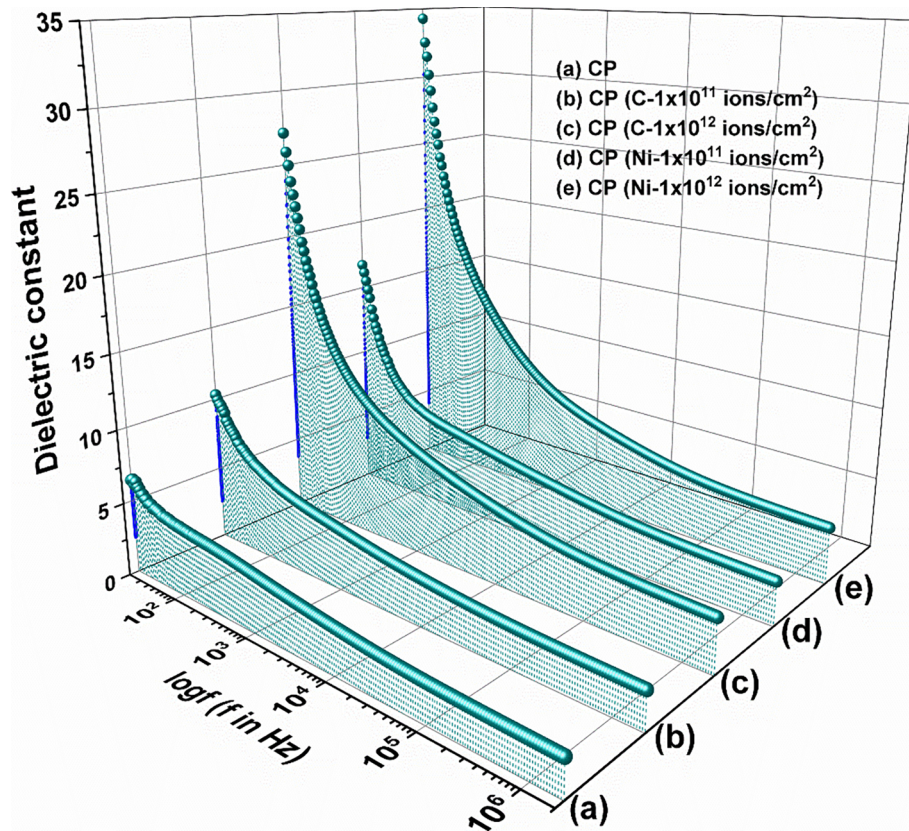


Fig. 6. Plot of dielectric constant versus log frequency for pristine and irradiated CP blend with 60-MeV C^{+5} and 100-MeV Ni^{+7} ions at the fluence of 1×10^{11} and 1×10^{12} ions/cm², respectively.

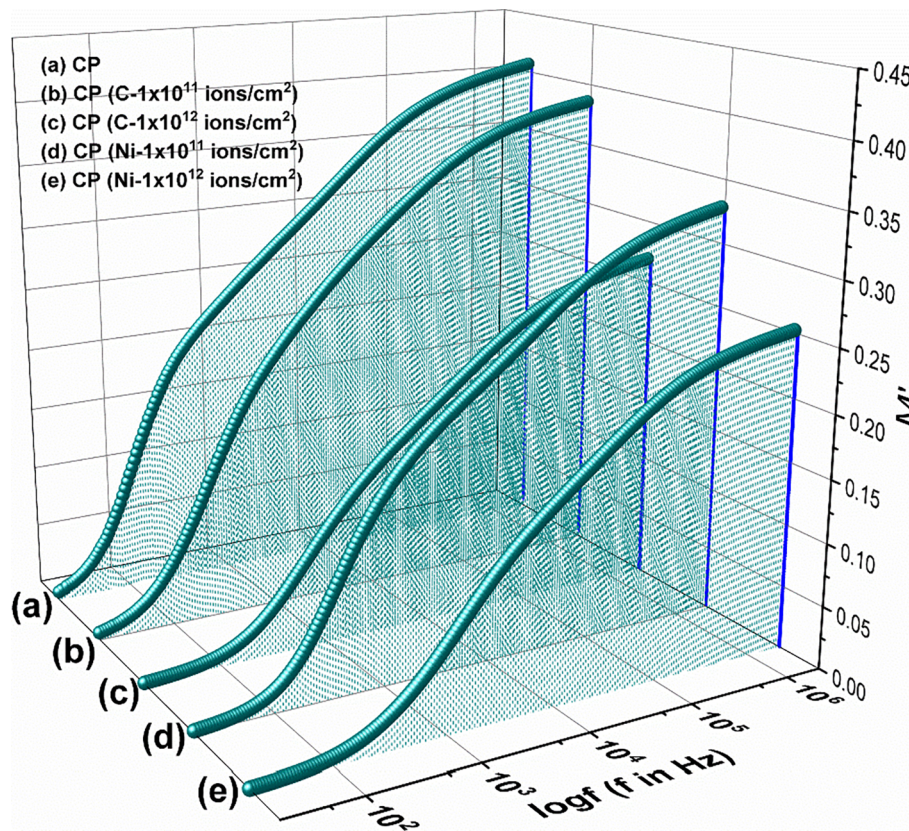


Fig. 7. Plot of real part of modulus versus log frequency for pristine and irradiated CP blend with 60-MeV C^{+5} and 100-MeV Ni^{+7} ions at the fluence of 1×10^{11} and 1×10^{12} ions/cm², respectively.

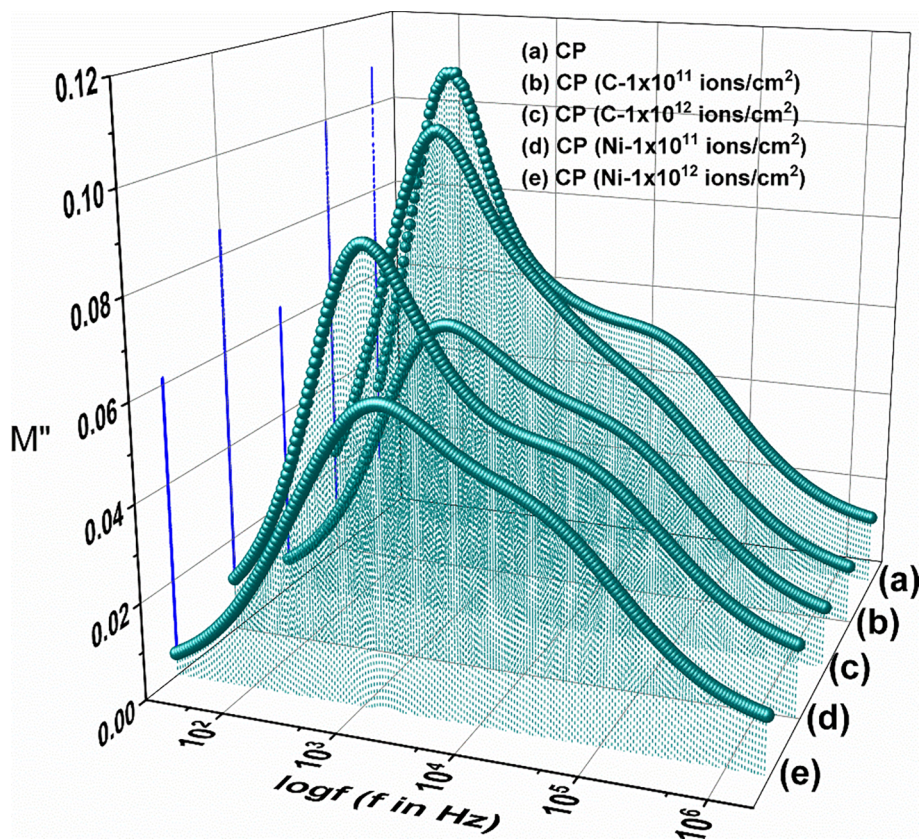


Fig. 8. Plot of imaginary part of modulus versus log frequency for pristine and irradiated CP blend with 60-MeV C⁺⁵ and 100-MeV Ni⁺⁷ ions at the fluence of 1×10^{11} and 1×10^{12} ions/cm², respectively.

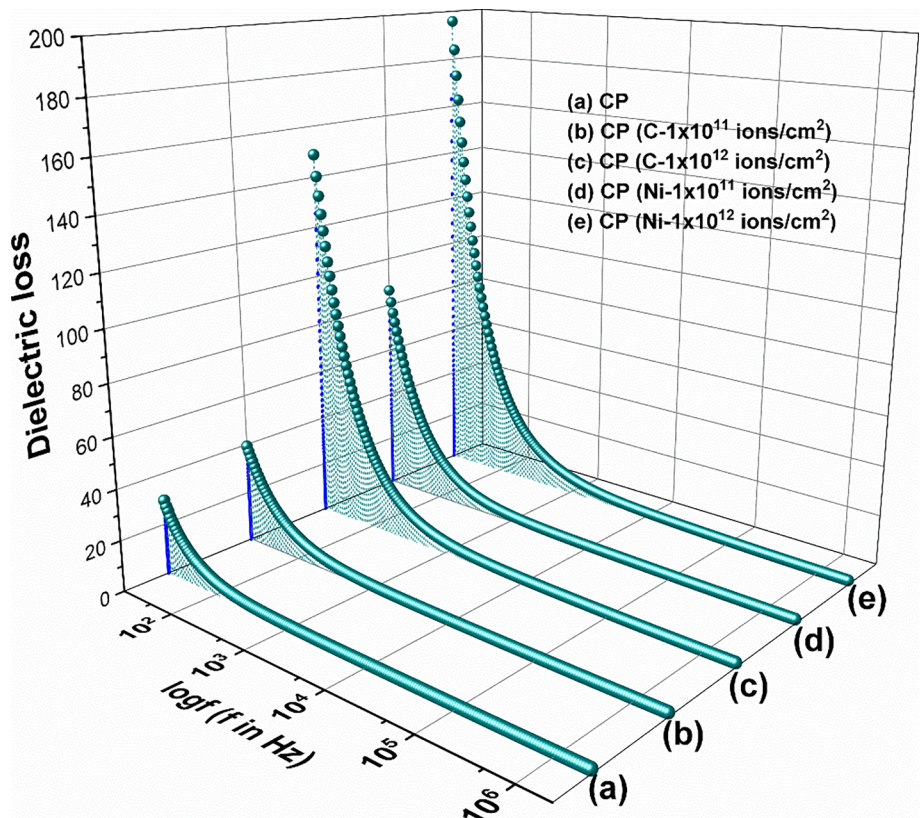


Fig. 9. Plot of dielectric losses versus log frequency for pristine and irradiated CP blend with 60-MeV C⁺⁵ and 100-MeV Ni⁺⁷ ions at the fluence of 1×10^{11} and 1×10^{12} ions/cm², respectively.

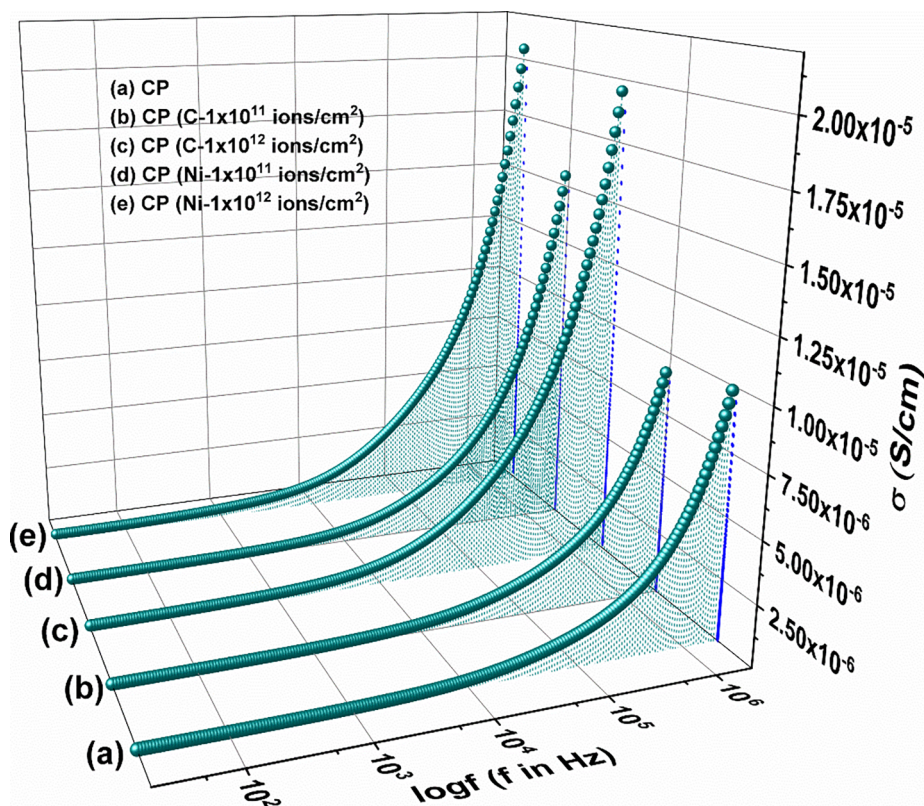


Fig. 10. Plot of conductivity versus log frequency for pristine and irradiated CP blend with 60-MeV C^{+5} and 100-MeV Ni^{+7} ions at the fluence of 1×10^{11} and 1×10^{12} ions/cm², respectively.

frequency with a reduction in the value of M''_{max} . This results ascribed to an increase in charge carrier density and reduced moment of inertia due to rupture of polymeric linkages. The value of M''_{max} and corresponding relaxation frequency remain unaffected in case of high frequency dispersion upon SHIs irradiation. However, the widening of the peak is observed, ascribed to structural reform and creation of defects. The plot of $\epsilon'' \rightarrow \log f$ as shown in Fig. 9 revealed deficiency of peak and exponentially decreasing response with increasing frequency. Indicating the effectively collective motion of induced charge carriers upon irradiation and modified polymeric components during the conduction processes. These results enhanced the conductivity upon SHI irradiation owing to the formation of conducting track and the increase in number of free radicals and charge carriers in the host matrix [15].

The frequency dependent conductivity response of all the samples is portrayed in Fig. 10. It perceived that due to SHI irradiation, the conductivity of the blend matrix for all the frequency increased. Moreover, the plot shows identical patterns of conductivity response as well as obeys “Jonscher universal power law” as follow:

$$\sigma(\omega, T) = \sigma_{dc} + B\omega^s$$

The lower frequency response attributed to dc conduction (σ_{dc}), while the higher frequency dispersion attributed to ac conduction ($\sigma_{ac} = B\omega^s$, B is pre-exponential factor). Fig. 11 revealed that the dc conductivity improved as a function of ion fluence and energy. Further, upon carbon and nickel ions irradiation at an ion fluence of 1×10^{12} ions/cm², σ_{dc} increased by $\sim 165\%$ and $\sim 279\%$ respectively. This indicates moderate decrease in moment of inertia upon heavier and energetic nickel ion irradiation owing to macromolecular chain disruption as revealed by FTIR. Fig. 12 depicts plot of $\log \sigma_{ac} \rightarrow \log \omega$ and its slope ($d\sigma_{ac}/d\omega$) at higher frequency to avoid the interfacial polarization yielding fractional exponent (s). The value of temperature dependent and dimensionless ‘s’ lies between 0 and 1. The value of s was precisely acquired by employing linear regression technique. The

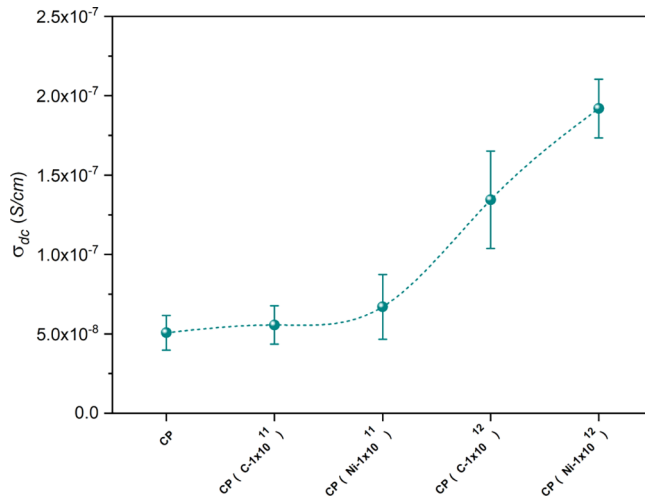


Fig. 11. Variation in dc conductivity as a function of ion fluence.

value of the regression coefficient (R^2) is nearly 0.99, suggesting reliable fitting. The estimated values of ‘s’ is ranging between 0.86 and 0.82, indicating that the conduction phenomenon in blend matrix is owing to the hopping of charge carriers, and it is AC type [27]. The transition in σ_{ac} is accompanied by modifications upon a radiation treatment is an evidence of formation of free radicals, randomization of polymeric chains, sp^2 hybridization, and development of carbon-rich conductive network within the matrix as well as increasing an extent of amorphization and free volume [9,14,15,19,21,23]. These results collaborated with physicochemical observations.

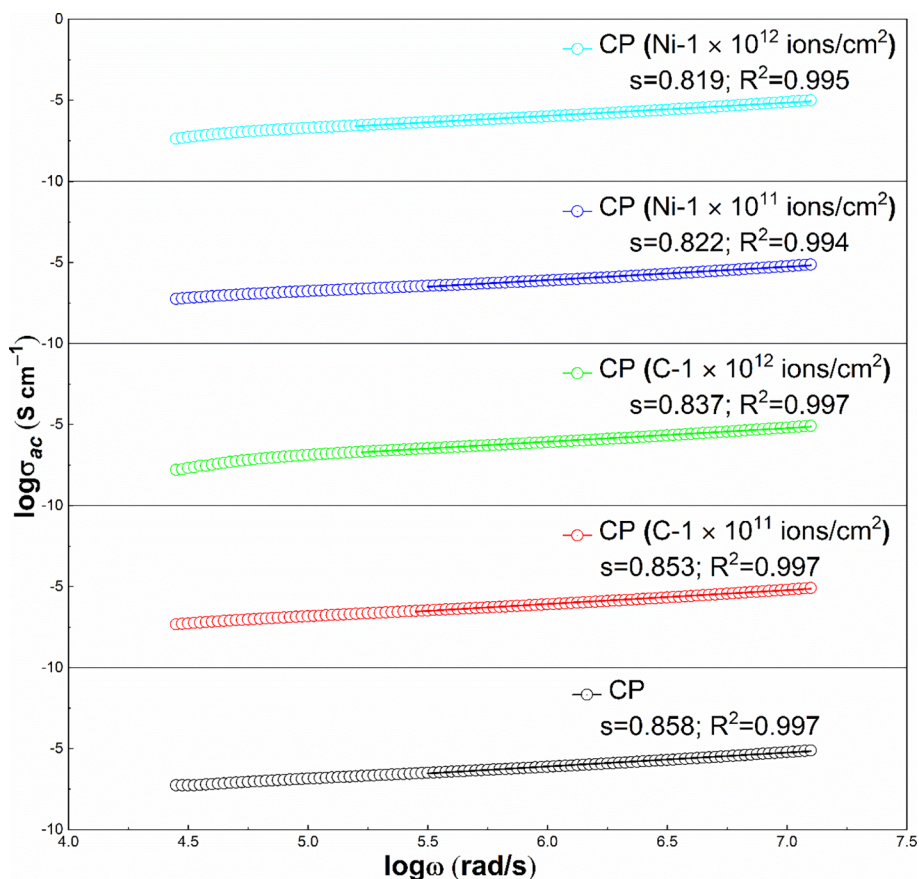


Fig. 12. Plot of log ac conductivity versus log angular frequency for all the CP blend samples.

3.5. Thermal analysis

DSC is a versatile tool to explore the thermal response as well as the degree of crystallinity of the polymeric system. Fig. 13 illustrates the DSC curves of the pristine and irradiated CP blend at an ion fluence of 1×10^{12} ions/cm². It seems that the thermal responses of CP blend were immensely perturbed by radiation treatment. The degree of

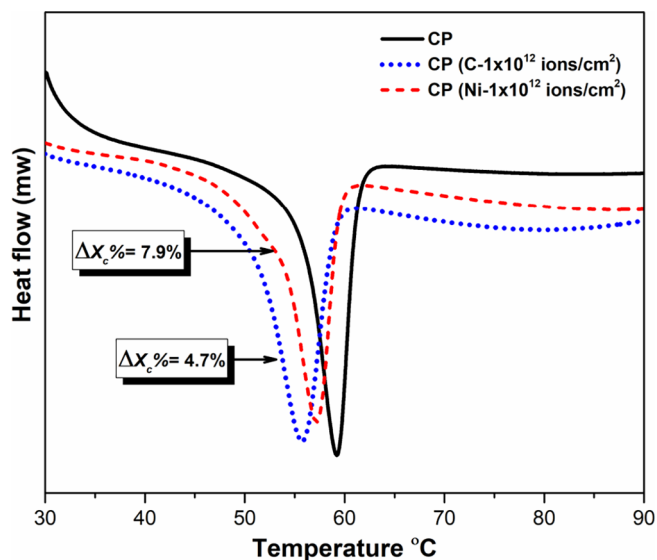


Fig. 13. DSC of pristine and irradiated CP blend with 60-MeV C⁺⁵ and 100-MeV Ni⁺⁷ ions at the highest fluence.

crystallinity ($X_c\%$) calculated as described in the literature [14]. The inset of Fig. 13 shows the relative change in the degree of crystallinity ($\Delta X_c\%$) of blend matrix. The values of $X_c\%$ decreased by $\sim 4.7\%$ and $\sim 7.9\%$ because of carbon and nickel ions irradiation respectively. Implying enhancement in inter and intra chains free volume resulted in flexibility of the polymer chains and hence decrease in moment of inertia. Moreover, it is because of molecular weight loss of polymer owing to scissioning of polymeric chains. DSC results clearly justify the XRD and FTIR discussions. Hence, modification of physicochemical properties of the blend matrix moderately governed by the incident ion beam parameters.

3.6. Surface morphology

Fig. 14(a) displays micrographs of AFM images of pure CP blend, Fig. 14(b) and (c) show CP blends irradiated at highest fluence with C⁺⁵ and Ni⁺⁷ ions, respectively, selected for probing the alteration in surface morphology. The surface of pure CP blend seemed considerably rough owing to hillock-like structures. In addition, the average surface roughness (R_a) at magnification of $5 \times 5 \mu\text{m}^2$ was obtained 68.0 nm. At a higher fluence, R_a value was significantly varied and attained 43.3 nm and 29.6 nm upon C⁺⁵ and Ni⁺⁷ ions, respectively. Implying prominent alterations of surface topography because of nickel ion, in fact, its hitting impact was potential as compared to C⁺⁵ ion at a time of penetration owing to higher mass and energy. Moreover, the small size uniform structure developed on the surface upon irradiation attributed to overlapping of ions tracks leading to carbonization of the matrix along the development of conjugated system of bonds as explained in optical data. Inclusively, the radiation treated polymeric surface became considerably smoother and could be modified by changing the beam parameters.

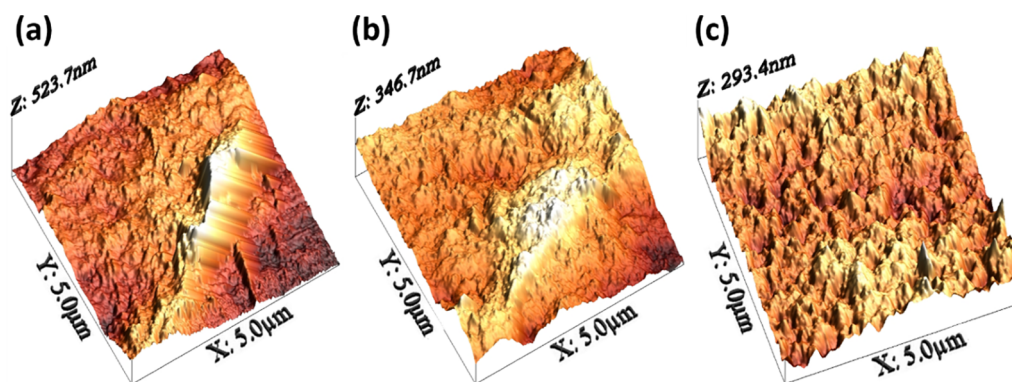


Fig. 14. AFM of (a) pristine and irradiated CP blend with (b) 60-MeV C^{+5} and (c) 100-MeV Ni^{+7} ions at the highest fluence.

4. Conclusions

Biodegradable blend matrix was formed with the help of chitosan and PEO polymer via solution blending route, which was irradiated by different ions in a controlled manner and characterized accurately. The physicochemical properties of the CP blend were affected by SHIs irradiation. The crystallite size and the degree of crystallinity were monotonously decreased by 10.7% and 7.9%, respectively. In addition, the functional vibration groups were not affected/shifted upon varying beam parameters, however yielding structural degradation and rupture of polymeric linkage. Due to the structural modifications, the absorption edge was shifted towards the longer wavelength and the band gap was decreased. These results also suggest that SHIs irradiation may initiate the defects by enhanced nano-scale free volume holes, chain scissions and randomization of macromolecular chains as well as evolution of carbon-rich network due to substantial dehydrogenated process along with the creation of conjugated system of bonds due to volatile outgassing. Dielectric responses after radiation treatment considerably enhanced with both fluence-dependent and frequency-related, which led from the physicochemical modifications. The hopping mechanism in the process of charge conduction is observed with change in only hopping parameters upon irradiation. The incident ions with higher S_e value caused a momentous impact on overall polymeric spectroscopic responses. In addition, the outcome of the experiment reveals the effectiveness of the radiation treatment by heavier ions in tailoring the blend properties with variable fluence, energy and mass of the incident ion, which therefore grows to be a valued technique to design the tailor-made polymeric matrix for desired applications.

Acknowledgments

One of the authors (GBP) gratefully acknowledges DST-PURSE programme for the award of fellowship and IUAC, New Delhi for financial support as well as technical assistance during the beam time and characterization of the samples. We thankfully acknowledge Prof. V. A. Rana, Department of Physics, School of Sciences, Gujarat University for providing LCR measurement facility.

References

- [1] R.A. Gross, B. Kalra, Biodegradable polymers for the environment, *Science* (80) 297 (2002) 803 LP-807. <http://science.sciencemag.org/content/297/5582/803.abstract>.
- [2] M. Dash, F. Chiellini, R.M. Ottenbrite, E. Chiellini, Chitosan – a versatile semi-synthetic polymer in biomedical applications, *Prog. Polym. Sci.* 36 (2011) 981–1014, <https://doi.org/10.1016/j.progpolymsci.2011.02.001>.
- [3] S.K. Shukla, A.K. Mishra, O. Arotiba, B.B. Mamba, Chitosan-based nanomaterials: a state-of-the-art review, *Int. J. Biol. Macromol.* 59 (2013) 46–58, <https://doi.org/10.1016/j.ijbiomac.2013.04.043>.
- [4] E. Meaurio, N. Hernandez-Montero, E. Zuza, J.-R. Sarasua, Miscible blends based on biodegradable polymers, *Charact. Polym. Blends*, Wiley-VCH Verlag GmbH & Co. KGaA, Weinheim, Germany, 2014, pp. 7–92 doi: 10.1002/9783527645602.ch02.
- [5] S. Zivanovic, J. Li, P.M. Davidson, K. Kit, Physical, mechanical, and antibacterial properties of chitosan/PEO blend films, *Biomacromolecules* 8 (2007) 1505–1510, <https://doi.org/10.1021/bm061140p>.
- [6] M.F. Shukur, R. Ithnin, H.A. Illias, M.F.Z. Kadir, Proton conducting polymer electrolyte based on plasticized chitosan-PEO blend and application in electrochemical devices, *Opt. Mater. (Amst.)* (2013), <https://doi.org/10.1016/j.optmat.2013.03.004>.
- [7] M.H. Buraidah, L.P. Teo, C.M. Au Yong, S. Shah, A.K. Arof, Performance of polymer electrolyte based on chitosan blended with poly(ethylene oxide) for plasmonic dye-sensitized solar cell, *Opt. Mater. (Amst.)* 57 (2016) 202–211, <https://doi.org/10.1016/j.optmat.2016.04.028>.
- [8] M.F. Shukur, R. Ithnin, H.A. Illias, M.F.Z. Kadir, Proton conducting polymer electrolyte based on plasticized chitosan-PEO blend and application in electrochemical devices, *Opt. Mater. (Amst.)* 35 (2013) 1834–1841, <https://doi.org/10.1016/j.optmat.2013.03.004>.
- [9] A. Qureshi, D. Singh, N.L. Singh, S. Ataoglu, A.N. Gulluoglu, A. Tripathi, D.K. Avasthi, Effect of irradiation by 140MeV Ag^{11+} ions on the optical and electrical properties of polypropylene/TiO₂ composite, *Nucl. Instrum. Methods Phys. Res. Sect. B* 267 (2009) 3456–3460, <https://doi.org/10.1016/j.nimb.2009.07.016>.
- [10] J. Li, S. Zivanovic, P.M. Davidson, K. Kit, Production and characterization of thick, thin and ultra-thin chitosan/PEO films, *Carbohydr. Polym.* 83 (2011) 375–382, <https://doi.org/10.1016/j.carbpol.2010.07.064>.
- [11] D.A.D. Cassani, L. Altomare, L. De Nardo, F. Variola, Physicochemical and nano-mechanical investigation of electrodeposited chitosan:PEO blends, *J. Mater. Chem. B* 3 (2015) 2641–2650, <https://doi.org/10.1039/C4TB02044H>.
- [12] J. Kowalonek, Surface and thermal properties of UV-irradiated chitosan/poly(ethylene oxide) blends, *J. Photochem. Photobiol. A Chem.* 348 (2017) 209–218, <https://doi.org/10.1016/j.jphotochem.2017.08.035>.
- [13] D.K. Avasthi, G.K. Mehta, *Swift Heavy Ions for Materials Engineering and Nanostructuring*, Springer, Netherlands Dordrecht, 2011 doi: 10.1007/978-94-007-1229-4.
- [14] G.B. Patel, S. Bhavsar, N.L. Singh, F. Singh, P.K. Kulriya, SHI induced modification in structural, optical, dielectric and thermal properties of poly ethylene oxide films, *Nucl. Instrum. Methods Phys. Res. Sect. B* 379 (2016) 156–161, <https://doi.org/10.1016/j.nimb.2016.04.018>.
- [15] G.B. Patel, N.L. Singh, F. Singh, Modification of chitosan-based biodegradable polymer by irradiation with MeV ions for electrolyte applications, *Mater. Sci. Eng. B* 225 (2017) 150–159, <https://doi.org/10.1016/j.mseb.2017.08.023>.
- [16] J.F. Ziegler, M.D. Ziegler, J.P. Biersack, SRIM – the stopping and range of ions in matter (2010), *Nucl. Instrum. Methods Phys. Res. Sect. B* 268 (2010) 1818–1823, <https://doi.org/10.1016/j.nimb.2010.02.091>.
- [17] J. Kowalonek, Surface and thermal behavior of chitosan/poly(ethylene oxide) blends, *Mol. Cryst. Liq. Cryst.* 640 (2017) 78–89, <https://doi.org/10.1080/15421406.2016.1255518>.
- [18] M. Pakravan, M.-C. Heuzey, A. Aji, A fundamental study of chitosan/PEO electrospinning, *Polymer (Guildf.)* 52 (2011) 4813–4824, <https://doi.org/10.1016/j.polymer.2011.08.034>.
- [19] N.L. Singh, A. Sharma, D.K. Avasthi, V. Shrinet, Temperature and frequency dependent electrical properties of 50 MeV Li^{3+} ion irradiated polymeric blends, *Radiat. Eff. Defects Solids* 160 (2005) 99–107, <https://doi.org/10.1080/10420150500116649>.
- [20] C.A. Daniels, *Polymers: Structure and Properties*, Technomic Publishing Company, USA, 1989.
- [21] E.H. Lee, Ion-beam modification of polymeric materials – fundamental principles and applications, *Nucl. Instrum. Methods Phys. Res. Sect. B* 151 (1999) 29–41, [https://doi.org/10.1016/S0168-583X\(99\)00129-9](https://doi.org/10.1016/S0168-583X(99)00129-9).
- [22] J. Tauc, R. Grigorovici, A. Vancu, Optical properties and electronic structure of amorphous germanium, *Phys. Status Solidi* 15 (1966) 627–637, <https://doi.org/10.1002/psb.19660150224>.
- [23] D. Fink, W.H. Chung, R. Klett, A. Schmoltdt, J. Cardoso, R. Montiel, M.H. Vazquez, L. Wang, F. Hosoi, H. Omichi, P. Goppelt-Langer, Carbonaceous clusters in irradiated polymers as revealed by UV-Vis spectrometry, *Radiat. Eff. Defects Solids* 133 (1995) 193–208, <https://doi.org/10.1080/10420159508223990>.
- [24] D. Fink, R. Klett, L.T. Chadderton, J. Cardoso, R. Montiel, H. Vazquez,

- a.a. Karanovich, Carbonaceous clusters in irradiated polymers as revealed by small angle X-ray scattering and ESR, Nucl. Instruments Methods Phys. Res. Sect. B 111 (1996) 303–314, [https://doi.org/10.1016/0168-583X\(95\)01433-0](https://doi.org/10.1016/0168-583X(95)01433-0).
- [25] R.J. Sengwa, S. Choudhary, Investigation of correlation between dielectric parameters and nanostructures in aqueous solution grown poly(vinyl alcohol)-montmorillonite clay nanocomposites by dielectric relaxation spectroscopy, Express Polym. Lett. 4 (2010) 559–569, <https://doi.org/10.3144/expresspolymlett.2010.70>.
- [26] G.C. Psarras, K.G. Gatos, J. Karger-Kocsis, Dielectric properties of layered silicate-reinforced natural and polyurethane rubber nanocomposites, J. Appl. Polym. Sci. 106 (2007) 1405–1411, <https://doi.org/10.1002/app.26831>.
- [27] A.K. Jonscher, *Dielectric Relaxation in Solids*, Chelsea Dielectric Press, London, 1983.



Modification of chitosan-based biodegradable polymer by irradiation with MeV ions for electrolyte applications



Gnansagar B. Patel^a, N.L. Singh^{a,*}, Fouran Singh^b

^a Department of Physics, The M. S. University of Baroda, Vadodara 390002, India

^b Inter University Accelerator Centre, Aruna Asaf Ali Marg, New Delhi 110067, India

ARTICLE INFO

Keywords:

Chitosan
Solid polymer electrolytes
SHI irradiation
Optical properties
Dielectric properties

ABSTRACT

Effect of swift heavy ion irradiation on electrical and optical properties of chitosan-based solid polymer electrolyte system, prepared by the solution casting technique, was investigated. The solid polymer electrolyte films were irradiated with C^{+5} and Ni^{+7} ions of energy 60 and 100 MeV, respectively, at different fluences. X-ray diffraction (XRD) analysis revealed the transformation of chitosan structure to the amorphous phase due to the addition of salt. FTIR spectra showed diverse vibrational modes and scissioning of bonds due to ion beam irradiations. Ions produce volatile low-molecular-weight species and results in the evolution of gas during irradiation processes. The polymer electrolyte became carbon rich with more conjugated bonds and diminished the band gap, as found by the UV–Vis analysis. The variable parameters obtained by the Bergman fitting specify that the relaxation process in the polymeric matrix is non-Debye, and the conductivity of electrolyte enhanced as a function of beam parameters.

1. Introduction

Climate change is a global challenge and one of the major issues for human beings. It is necessary to control the recent and imminent activities of indigenous people that affect the environment worldwide. Eco-friendly natural polymers are used as solid polymer electrolytes (SPEs) because of their low toxicity, biodegradability, and less polluting nature. Presently, SPEs are widely used in the applications of electrical and optical devices as solid state batteries, gas sensors, electrochromic display devices, supercapacitors, and fuel cells [1–8]. Biodegradable polymers such as polyethylene oxide [6], polyvinyl alcohol [7], methyl cellulose [8], and chitosan [1–4] have been studied widely, and further research studies using SPE system are in progress. The advantages of SPEs are their compactness and reliability without leakage of liquid constituents.

Chitosan is a biopolymer used as a host for SPE and is derived from chitin by deacetylation [4]. After cellulose, chitosan is the second most abundant natural amino polysaccharide with distinctive structures, multidimensional properties, and wide-ranging applications in biomedical and other industrial areas [9]. Chitosan has attracted considerable attention because of its ease of processability and customization of properties to achieve the desired functionalities [10,11]. The chitosan structure contains oxygen and nitrogen atoms with a lone pair of electrons, which help to form complexes with the salt. In the SPE

system, doped inorganic salts are dissociated in the polymeric matrix, which is responsible for the ionic conductivity. At room temperature, the ionic conductivity is about 10^{-8} – 10^{-7} S/cm [12]. The SPEs may have crystalline and amorphous phases, but the conductivity is significant in the amorphous state. Numerous attempts have been made to reduce the crystalline structure of biopolymer-based SPEs, including blending with conducting biopolymer and addition of nano fillers, ceramic fillers, and plasticizers. All these fillers improve various properties of the host polymer up to a certain extent. Hence, further modifications in the physical property of SPE matrix can be performed by irradiation with swift heavy ions (SHIs). This technique provides a unique process to modify the microstructures of materials by electronic excitation and ionization processes in a controlled manner [13,14]. We particularly preferred the silver nitrate salt as it has been rarely investigated in the SPE system with chitosan as a host. Morni et al. [4] studied the electrochemical cell performance of chitosan-doped silver nitrate salt and concluded that it can be used as an electrolyte for the fabrication of solid-state batteries. Yulianti et al. [15] used the ion implantation technique for polymer electrolyte synthesis by employing a low-energy ion (Li, Cu, or Ag) beam. In addition, the electrical properties of ion implanted-chitosan-based polymer electrolytes are enhanced by using a low energy beam. The low-energy beam cannot penetrate deep into the materials and is primarily responsible for surface modifications. Despite the vast applications of biodegradable

* Corresponding author.

E-mail address: nl.singh-phy@msubaroda.ac.in (N.L. Singh).

chitosan-based polymer, few studies have studied the SHI irradiation-induced effects on chitosan-based SPE as a function of additive level, ion beam species, and ion fluences. A comparative study of ion beam effects on the electrical and optical properties of SPE was also conducted.

2. Experimental

2.1. Materials

Chitosan powder (deacetylation 75–85%, molecular weight 50,000–190,000 Da) and acetic acid were purchased from Sigma-Aldrich. Silver nitrate with a molecular weight of 169.87 g/mol was supplied by Suvidhinath Laboratories, India. Double-distilled water was used during the synthesis procedure.

2.2. Preparation of SPE

The solution casting method was used for the synthesis of chitosan-based SPE. The chitosan powder was dissolved in 1.0% acetic acid. To this chitosan suspension, different amounts of silver nitrate were added separately. The mixture was stirred continuously with heating until it became completely homogeneous. Furthermore, it was sonicated for half an hour. The sonicated solution was poured into a Teflon petri dish at room temperature to get free-standing SPE thin films (thickness ~60 μm). For simplicity, the SPE films were labeled as CS, CSA, CSB, CSC, and CSD for 0, 5, 10, 15, and 20 wt% of silver ions in the respective chitosan acetate solution. In addition, we restrict our discussions up to 15 wt% concentration because, recrystallization of salt occurred beyond 15% concentration, as observed in many literatures [1–3,5,6,12,16]. The obtained films were kept in desiccators with silica gel for further desiccation.

2.3. SHI irradiation of SPE

The SPE films of area $1.5 \times 1.5 \text{ cm}^2$ were fixed on a vertical sliding copper ladder. After achieving vacuum around 10^{-6} Torr, these films were irradiated with 60-MeV C^{+5} and 100-MeV Ni^{+7} ions in the materials science beam line scattering chamber at IUAC, New Delhi, India. The ion beam current was 0.5 pA. The irradiation was performed at room temperature by scanning $1 \times 1 \text{ cm}^2$ area of the SPE film in the x-y plane at fluences of 1×10^{11} and 1×10^{12} ions/ cm^2 .

2.4. Energy loss and range of carbon and nickel ions in SPE

The SRIM 2013 code [17] was used to obtain the electronic energy loss (S_e), nuclear energy loss (S_n), and projected range of 60-MeV C^{+5} and 100-MeV Ni^{+7} ions in chitosan ($\text{C}_6\text{H}_{11}\text{O}_4\text{N}$) polymer matrix having an approximate mass density of 0.25 g/cm^3 . The simulated values of S_e and S_n and the projected range for C^{+5} ion were 69.29 keV per micron, 3.88×10^{-2} keV per micron, and 554 μm , respectively. In the case of Ni^{+7} ions, the obtained values of S_e and S_n and the projected range were 11.1×10^2 keV per micron, 1.81 keV per micron, and 126 μm , respectively. This implies that the nuclear energy loss during SHI irradiation is almost negligible for both ions, while the electronic energy loss seems to be dominant. In addition, the value of S_e for Ni^{+7} ions is hundred times higher than that for C^{+5} ions.

2.5. Characterizations of SPE

XRD measurement was performed using a Bruker D8-Advance diffractometer to study the amorphous or crystalline structure of SPE. The wavelength of monochromatic Cu-K α radiation is 1.5418 \AA , and the diffraction patterns were recorded at angles of $5^\circ \leq 2\theta \leq 65^\circ$. FTIR analysis was performed using a JASCO-4100 spectrometer to confirm the complexation between polymer and salt and the radiation-induced

modifications in the structural properties of the electrolyte. The FTIR spectra were recorded in the transmission mode from 400 to 4000 cm^{-1} , with a resolution of 1 cm^{-1} after 100 accumulated scans. UV-visible spectroscopy was performed to study the optical properties of the electrolyte using a Hitachi Model U-3300 spectrometer. The absorption spectra were recorded in 200–800 nm wavelength range. Complex impedance spectroscopy was performed using a Solartron SI-1260 impedance gain/phase analyzer to investigate the electrical properties of the SPE. The SPE films were sandwiched between two silver electrodes under spring tension. The impedance was measured in the frequency range of 10 Hz–10 MHz at ambient temperature with 1-V AC signal amplitude. The data were collected using a fully automated interfaced with a computer. The Z-View2 software was used to further analyze the AC electrical data. The highest conductivity was obtained for the CSC sample (similar observations on the conductivity were reported by Morni et al. [4]). The surface morphology of the electrolyte samples was studied in the tapping mode using AFM Nanoscope digital Instruments, Canberra, USA, in air at ambient temperature. The electronic digital caliper (Forbes) was used to measure the thickness of the electrolytes.

3. Results and discussion

3.1. XRD analysis

To investigate the effect of silver nitrate salt with chitosan-based polymer, the XRD study of pure chitosan and chitosan–silver nitrate salt complexes was conducted. Fig. 1 shows the X-ray diffraction patterns of pure chitosan and silver nitrate-doped chitosan-based electrolytes. Different peaks observed at 8.2° , 11.6° , 15° , 18° , and 21.7° were identified as the characteristic peaks of pure chitosan. The two peaks that appeared at 8.2° and 11.6° indicate a hydrated crystalline structure, while the peak at 15° may be attributed to the anhydrous crystalline structure. In addition, the broader peaks that appear at 18° and 21.7° show the existence of an amorphous phase of chitosan [18]. A comparison of the X-ray diffraction patterns of pure chitosan and silver nitrate-doped chitosan-based electrolytes revealed that the different peaks corresponding to chitosan disappeared and a broader peak evolved upon the addition of salt. This confirms the interaction between the silver nitrate salt and chitosan matrix. The broadening of peak can be attributed to the increased separation of the polymeric chain of the SPE incorporated with salt. In addition, the synthesis temperature of SPE system (about $60 \pm 2^\circ\text{C}$) helped to achieve the amorphous phase. In addition, the peak that corresponds to silver nitrate salt was not observed in the XRD pattern. This suggests the structural rearrangement of host polymer and salt with no surplus salt present in the SPE, but the crystalline peaks with very small intensity that appeared at $\sim 38^\circ$ and $\sim 44^\circ$ correspond to the (1 1 1) and (2 0 0) planes of silver nanoparticles, respectively. During the synthesis, chitosan acts both as reducing and capping agents in a lightly heated system, yielding silver nanoparticles [19]. In addition, the pattern of irradiated SPE system did not reveal any considerable change.

3.2. FTIR analysis

To understand the interaction of chitosan with silver nitrate salt and the effect of SHI irradiation on existing chemical bonds/functional groups within the compound, IR transmittance measurements were made. Fig. 2 represents the IR spectra of CS and highest conducting electrolyte system CSC. First of all, no peak was observed at 1590 cm^{-1} attributed to the $-\text{NH}_2$, but a band appeared at 1540 cm^{-1} conforming NH_3^+ [20]. This implies that the SPE is basically in the acetate form. The strong characteristic vibration band center at 3426 cm^{-1} corresponds to the overlapping of O–H stretching vibrations with the N–H stretching. The bands that appeared at 1639 cm^{-1} (amide I group) and 1329 cm^{-1} (amide III group) correspond to the mode of amino group

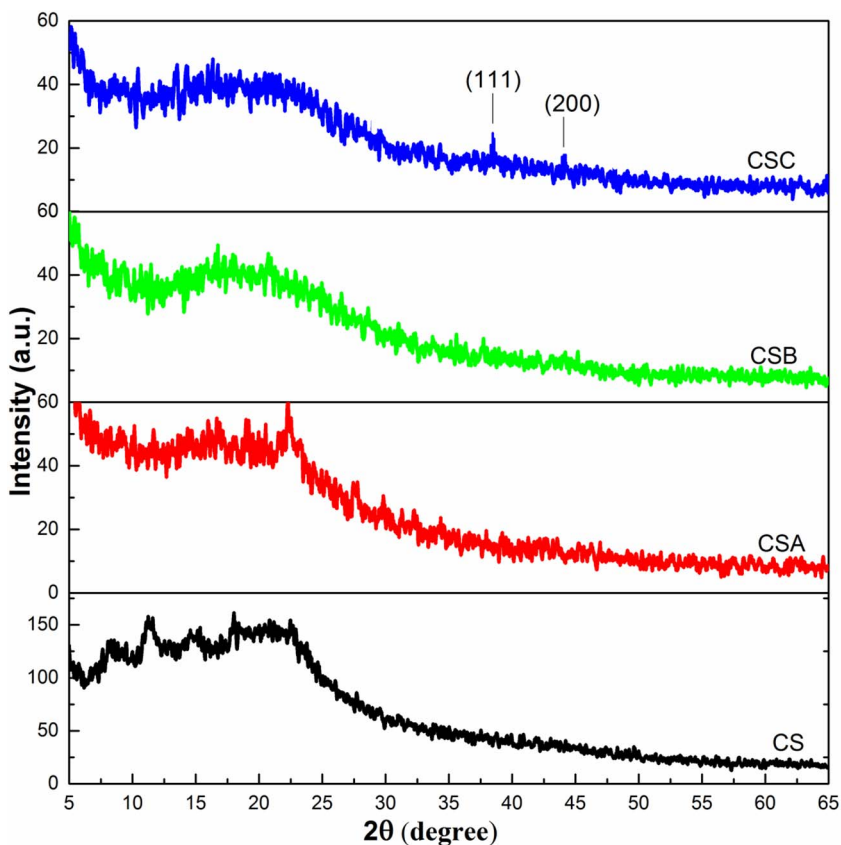


Fig. 1. XRD patterns of CS and SPE system with different concentrations.

[21]. In the IR spectra, vibrational modes at 1410 cm^{-1} (CH_2 bending and CH_3 deformation), 1380 cm^{-1} (symmetric CH_3 deformation and CH bending), and 1320 cm^{-1} (CH_2 wagging) were also observed [22]. The peaks at wavenumbers 2925 and 2881 cm^{-1} were due to the C–H stretching vibrations (asymmetric and symmetric, respectively). The bands at $1260, 1154, 898,$ and 665 cm^{-1} can be attributed to the OH bending, C–O stretching, C–H out-of-plane, and the –NH twisting vibration mode, respectively [23].

The inset of Fig. 3 depicts the concentration-dependent FTIR spectra

of the electrolyte system. The characteristic absorption peaks of CS at $1639, 1540, 1410, 1329, 1154,$ and 898 cm^{-1} shifted to $1650, 1559, 1404, 1324, 1143,$ and 897 cm^{-1} upon the addition of salt in the CSC electrolyte system. Furthermore, the intensities of peaks corresponding to $2925, 2881, 1540,$ and 898 cm^{-1} increased, while the intensities of other peaks corresponding to the vibrational modes decreased. In addition, the broadening of the peak may be due to increased concentration of free ions. A similar trend was observed for the concentration-dependent interaction of salt–chitosan host matrix. The

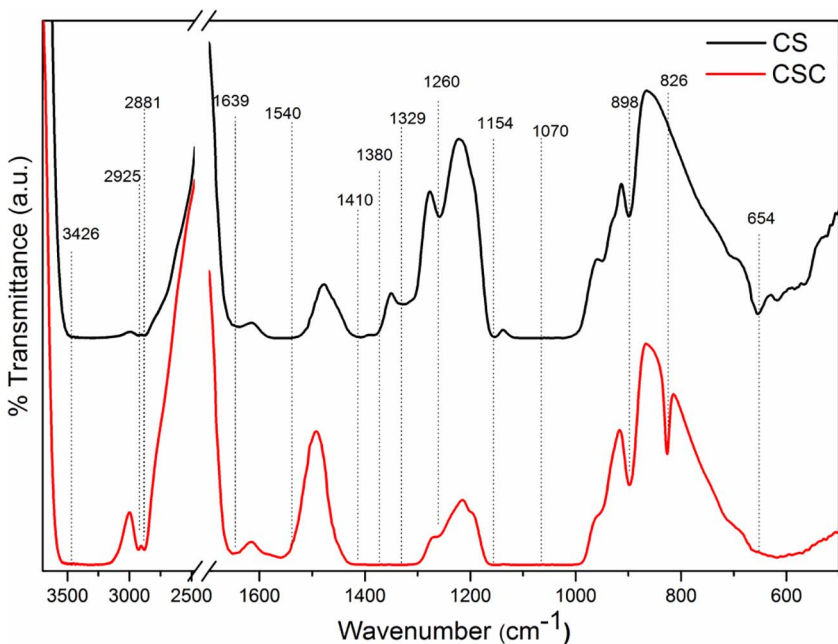
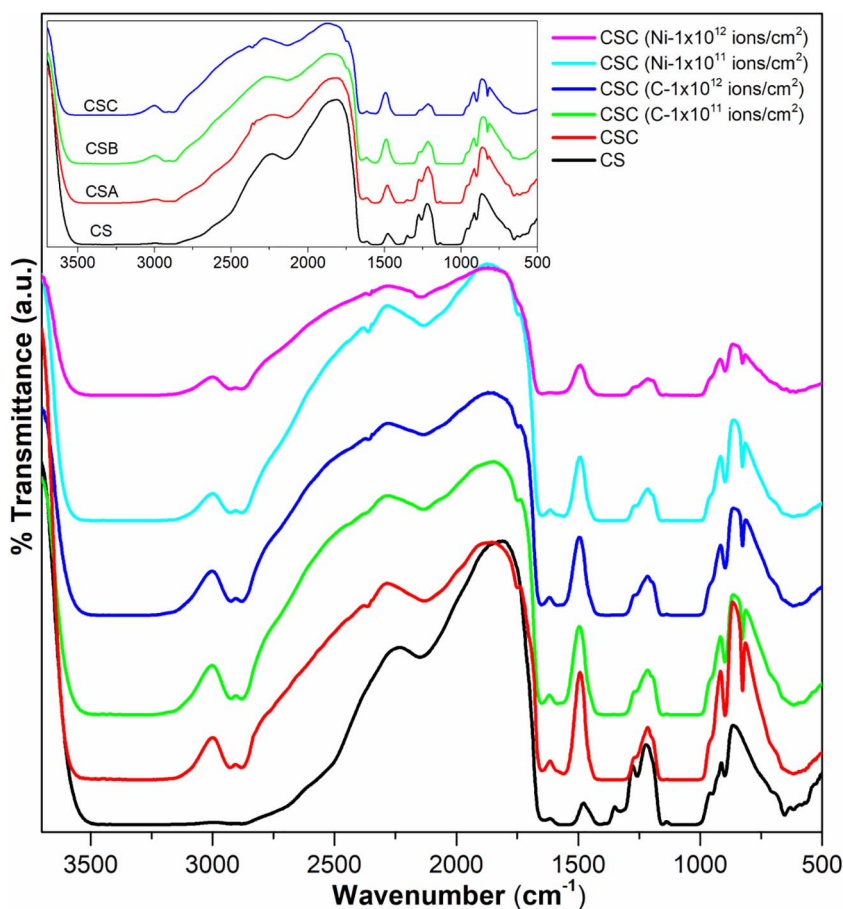


Fig. 2. FTIR spectrum of CS and CSC SPE samples.



peaks at wave numbers 665 and 1380 cm^{-1} disappeared, while a new peak appeared at wave number 826 cm^{-1} . Moreover, the absence of silver nitrate peaks in the IR spectra revealed the complexation of the salt with chitosan matrix [16]. These discussions conclude that there is a considerable interaction of the salt or metal ions with chitosan, which is responsible for ionic conductivity.

Fig. 3 shows the FTIR spectra of pristine CSC and irradiated CSC with carbon and nickel ions at different fluences. After the SPE film was irradiated, the transmission intensity of all the peaks decreased considerably without any significant shift in the peak position. The reduction in intensity may be ascribed to the changes in the bond structure of CSC due to the abstraction of intra-chain hydrogen linkage with NH_2 and/or OH groups of chitosan macromolecule. As the SHIs moved through the polymeric material, inter ionization and excitation of electrons occurred. As discussed in the earlier section, the electronic energy loss of SHI in chitosan matrix is of the order of kilo electron volts per micron. Because the strength of the chemical linkage in polymer matrix is of the order of a few electron volts [24], there could be scission of all the bonds in the zone of the ion track, thereby leading to the formation of free radicals or ions due to the heterolysis or homolysis bond cleavages in the SPE system, respectively [25]. These low-molecular species generated become a part of bulk polymer or leave the polymer due to high vacuum. Consequently, there will be localized structural modification through the randomization of polymeric chain and degradation of polymer. The degradation of SPE system increases with the increase in fluence. In addition, heavier ions cause significant amorphization than lighter ions because of larger electronic energy loss.

3.3. Optical analysis

The optical properties of concentration-dependent and SHI-exposed

Fig. 3. FTIR spectra of SPE samples irradiated with 60-MeV C^{+5} and 100-MeV Ni^{+7} ions at the fluences of 1×10^{11} and 1×10^{12} ions/ cm^2 , respectively. Inset shows the concentration-dependent FTIR spectra of SPE.

SPE systems were investigated by UV–Vis absorption spectroscopy. The nature of the optical band gap and its value can be determined using the fundamental absorption data, which correspond to the electron excitation. The absorption peak at 310 nm can be ascribed to the transformation of glucosamine into glucosamine acetate. This indicates the acetate form of SPE, which was revealed by the FTIR analysis also. The concentration-dependent absorption plot of SPE film (see inset of Fig. 4)

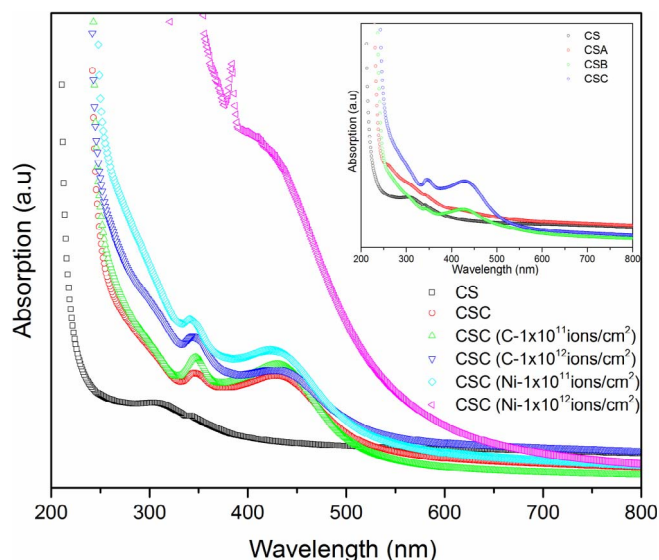


Fig. 4. UV–Vis spectrum of CS and CSC irradiated with 60-MeV C^{+5} and 100-MeV Ni^{+7} ions at the fluences of 1×10^{11} and 1×10^{12} ions/ cm^2 , respectively. Inset shows the concentration-dependent UV–Vis spectrum of SPE.

shows the absorption peak centered at 428 nm as compared to CS revealed the surface plasmon resonance (SPR) of Ag nanoparticles [1,26]. With the increase in doping concentration, the intensity of the peak increased due to glucosamine acetate, which can be ascribed to the chemical interaction between chitosan and AgNO₃, and another peak intensity was observed, which can be attributed to the concentration of Ag nanoparticles. The increase in SPR peak intensity corresponding to Ag nanoparticles revealed that the static charge transfer process [27] occurred during the SHI irradiation due to the availability of an abundant number of free electrons, resulting in the transformation of Ag⁺ ions into metallic Ag⁰ nanoparticles. In addition, the red shift in absorption edge (AE) is observed because of $\pi \rightarrow \pi^*$ electronic transition [28]. In this type of transition, the excitation of electrons occurs from the HOMO to the LUMO. In general, this type of transition occurs in materials with double or triple bonds and triggers in the unsaturated centers [28]. These observations indicate the strong interactions between the silver ions and NH₂ and/or OH groups of chitosan after doping. This resembles the change in crystallinity within the SPE system, which affects the band gap. This agrees with their XRD and FTIR responses. After irradiation, the AE become broader and shift toward the visible region, and the level of Ag nanoparticles increases. (shown in Fig. 4). The broadening of the AE is attributed to the formation of SHI-induced defects along with the formation of some low-molecular-weight radicals and ions. Moreover, these may cause excitation of non-bonding electrons to the conduction band, which generates new energy levels [29]. This shows an attenuation in optical band gap upon SHI irradiation, which enhances the conductivity of the SPE.

Tauc's method can be used to estimate the transition energy between parabolic bands and the nature of transition using the following equation [30]:

$$\alpha h\nu = B(h\nu - E_g)^n$$

where n is the power that describes the transition processes in k -space, namely phonon mediated (indirect) or not (direct) and dipole mediated (allowed) or not (forbidden) ($n = 0.5, 1.5$ stand for a direct and indirect allowed, while 2 and 3 values correspond to direct and indirect forbidden transitions), $h\nu$ is the photon energy, E_g is the band gap, and α is the absorption coefficient [30]. The Tauc plot yields a satisfactory straight line fit for $n = 0.5$, which specifies that the SPE system obeys direct allowed transition. The extrapolated intercept on $h\nu$ axis for $(\alpha h\nu)^2 \rightarrow h\nu$ plot yield E_g for unirradiated and irradiated SPE samples and is listed in Table 1. After SHI irradiation, a decreasing tendency in the values of E_g was observed for all the SPE samples. The decrease in E_g may be attributed to the formation of intermediate sub-band state upon SHI irradiation. The value of E_g for CS was 5.638 eV and that for CSC was 4.619 eV, which decreased to 3.469 and 2.890 eV upon C-ion and Ni-ion irradiation at highest fluence, respectively. In addition, the

Table 1

Variation in optical energy band gap (E_g) and the number of carbon atoms per conjugation length (N) at different fluences of 60-MeV C⁺⁵ and 100-MeV Ni⁺⁷ ion irradiation for SPE samples.

Sample	Carbon (60 MeV)		Nickel (100 MeV)	
	E_g (eV)	N	E_g (eV)	N
Pristine CS	5.638 ± 0.018	37	5.638 ± 0.018	37
Pristine CSA	5.196 ± 0.019	44	5.196 ± 0.019	44
CSA (1 × 10 ¹¹ ions/cm ²)	5.006 ± 0.017	47	4.661 ± 0.029	54
CSA (1 × 10 ¹² ions/cm ²)	3.958 ± 0.006	75	3.072 ± 0.010	125
Pristine CSB	4.869 ± 0.020	50	4.869 ± 0.020	50
CSB (1 × 10 ¹¹ ions/cm ²)	4.812 ± 0.020	51	4.454 ± 0.029	59
CSB (1 × 10 ¹² ions/cm ²)	4.186 ± 0.014	67	2.924 ± 0.035	138
Pristine CSC	4.619 ± 0.019	55	4.619 ± 0.019	55
CSC (1 × 10 ¹¹ ions/cm ²)	3.555 ± 0.004	93	3.424 ± 0.011	100
CSC (1 × 10 ¹² ions/cm ²)	3.469 ± 0.007	98	2.890 ± 0.014	141

decrease in E_g upon C-ion and Ni-ion irradiations for CSC electrolyte sample was approximately ~24.9% and ~37.4%, respectively. A persuasive decrease in E_g was observed after Ni-ion irradiation as compared to C-ion irradiation because of higher electronic loss of Ni-ions than C-ions, and heavier Ni-ion may yield major defects below the conduction band such that there may be shifting of the conduction band edge into the forbidden gap. In addition, heavier Ni-ions effectively yield structural disorder and may form a large number of radicals in the polymer matrix compared to C-ions. As stated by the density of state for polymeric materials, disorder in the polymeric matrix is responsible for the increase in conductivity and decrease in band gap due to irradiation [31,32]. Moreover, the SHI irradiation of polymeric materials is accompanied by the evolution of some volatile gases and H₂ gas because of the cleavage of C–H linkages. Compagnini et al. [33] explained that optical behavior and H-concentration in the polymeric samples are strongly correlated, and a decrease in the H/C atomic fraction is observed because of hydrogen abstractions from polymeric structure upon SHI irradiation, which is in good agreement with the FTIR analysis. Hence, after irradiation, an increase in the number of C atoms was observed as compared to the number of H atoms, thus inducing the formation of carbonaceous clusters in the SPE sample [28,29,31,34].

As explained by Robertson and O'Reilly [31], the carbonaceous compact cluster can be considered a system of autonomous cluster, owing to the C₆ structure. Thereafter, the Robertson and O'Reilly model was revised by Fink et al. [34] by considering the cluster structure as C₆₀ rather than C₆. The number of carbon atoms per conjugation length (N) was evaluated by using the modified Fink model via the following relation [34]:

$$E_g = \frac{34.3}{\sqrt{N}} \text{eV}$$

The value of N for pristine and irradiated SPE samples are listed in Table 1. It reveals that with the increase in the level of doping and SHI irradiation fluence, there was an increase in the value of N . The variation in value of N upon C-ion irradiation was quite small when compared with that upon Ni-ion irradiation. This is attributed to significant energy density transferred per track and track overlapping in the grain structures by high-energetic [35] Ni-ions in the SPE matrix. Similarly, the formation of clusters ascribed to the transformation of the polymeric grain structure in the SPE matrix along with the degassing of volatile components and formation of radicals [34,35]. The electrical response of irradiated SPE system strongly depends on the size and density of carbonaceous clusters.

3.4. AC electrical frequency response

Dielectric spectroscopy is an ingenious tool for exploring the electrical response of polymeric materials and their interfaces to understand the conductivity mechanism and molecular relaxation behavior. The fundamental principle implicated that when an oscillating electric field is applied to the polymer film (sandwiched between the electrodes) charges polarize due to the alignment of dipoles. Hence, the output current failed to follow the oscillating field and lagged by a phase shift. This information that determines the capacitance and conductance as a function of frequency yields the dielectric properties of the materials. The real part $\epsilon'(\omega)$ of complex permittivity (ϵ^*) is given as follows:

$$\epsilon'(\omega) = C_p d / \pi r^2 \epsilon_0$$

where C_p is the measured capacitance using Zview2 software, d is the thickness (m) of SPE film, and r is the radius (m) of electrode–electrolyte contact area, and the dielectric permittivity of air is $8.854 \times 10^{-12} \text{ C}^2/\text{Nm}^2$. Fig. 5 illustrates the graph of $\epsilon'(\omega) \rightarrow \log f$ for pristine SPE samples irradiated with carbon and nickel ions. At first look, $\epsilon'(\omega)$ increased with the increase in dopant level of silver nitrate salt (See Fig. 5) and with the increase in ion fluence for both ions ascribed to some effect on dipoles. Furthermore, $\epsilon'(\omega)$ exhibited a similar

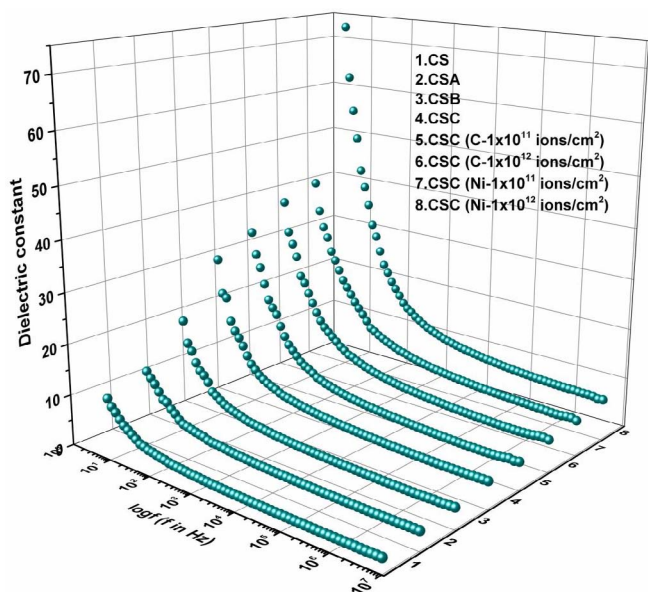


Fig. 5. Plot of dielectric constant versus log frequency for pristine and irradiated SPE with 60-MeV C^{+5} and 100-MeV Ni^{+7} ions at the fluences of 1×10^{11} and 1×10^{12} ions/cm², respectively.

increasing tendency with the decrease in frequencies attributed to polymer responses such as degree of polarization, deformation, and macromolecular motion in a time-varying field. $\epsilon'(\omega)$ can be explained in terms of polarization due to the migration of charge and dipole orientation. Fig. 5 shows that $\epsilon'(\omega)$ exhibited a certain behavior; indeed, $\epsilon'(\omega)$ increased substantially at low frequencies (< 10 kHz) and at a fluence of 1×10^{12} ions per square centimeter for Ni-ion and approached a constant value at higher frequencies. At low frequencies, the charge carriers in the electrolyte matrix had a long-range drift owing to enough time through a slow rate of change in the oscillation field. This is attributed to the increased accumulation of charges on the surfaces of the amorphous electrolyte/crystalline electrode regions (interfacial polarization) in low-frequency regions [2,12,16]. In addition, the induced dipoles follow the reversing field and attain the static dielectric constant at low frequencies. As the frequency increased (> 10 kHz), the induced dipoles lagged the reversing field, and a moderate decrease in $\epsilon'(\omega)$ was observed because of the vanishing orientation polarization. At a higher frequency region, the induced dipoles failed to follow the field, and they attained a constant value. Another promising reason for the decrease in $\epsilon'(\omega)$ at higher frequencies can be attributed to the migration of charge carriers through the dielectric and then the initiation of neutralization of charge carriers at defect sites by trapping [36]. Moreover, the polarization of trapped and bound charges cannot occur at higher frequency regions, thus decreasing the value of $\epsilon'(\omega)$ [37]. The increase in $\epsilon'(\omega)$ upon irradiation reveals the degradation of the polymer by breaking numerous bonds (which is observed from the FTIR data) and reduction of Ag^+ to Ag^0 (as explained in optical data). The degradation leads to an increase in the polymeric chain mobility because of the formation of low-molecular-weight segments. We can state that the heavier nickel ions caused considerable degradation of the SPE system and thus enhanced the value of dielectric constant more effectively.

The electric modulus spectra are a key tool to provide a prospect for dielectric spectroscopy to investigate relaxation in SPE system and conduction phenomena by vanishing the electrode polarization effects. The measured data of ϵ' and ϵ'' were used to obtain the frequency-dependent electric modulus (i.e., real part $M'(\omega)$ and imaginary part $M''(\omega)$) as follows [38]:

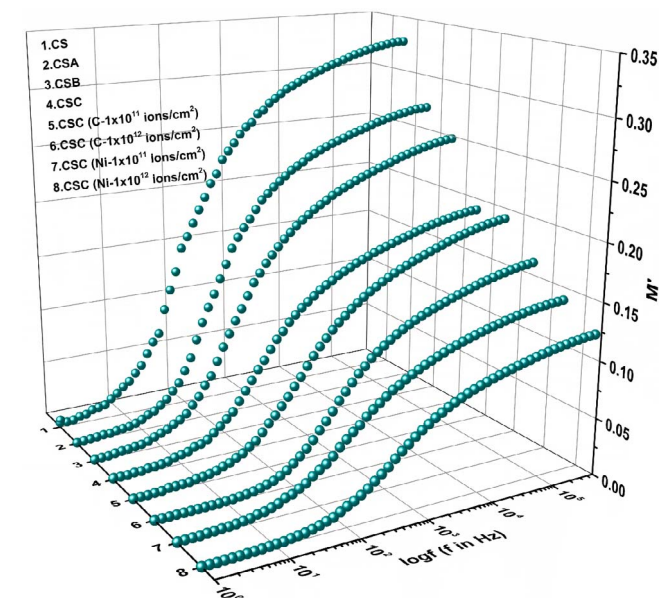


Fig. 6. Plot of real part of modulus versus log frequency for pristine and irradiated SPE with 60-MeV C^{+5} and 100-MeV Ni^{+7} ions at the fluences of 1×10^{11} and 1×10^{12} ions/cm², respectively.

$$M'(\omega) = \frac{\epsilon'(\omega)}{\epsilon'^2(\omega) + \epsilon''^2(\omega)}, M''(\omega) = \frac{\epsilon''(\omega)}{\epsilon'^2(\omega) + \epsilon''^2(\omega)}$$

In SPE system, the relaxation process of the real dielectric is suppressed because of ion conductivity. In addition, the electric potential of the surrounding in SPE system was perturbed because of the movement of ions from one site to another. This perturbed potential affects the transport properties of the other ions in this region. Such a cooperative motion of ions leads to a nonexponential decay or a conduction process with a distribution of relaxation time [39]. The long-range conduction mechanism and localized dielectric response can be interpreted by incorporating complex modulus and permittivity data.

Fig. 6 and Fig. 7 reveal the plot of $M'(\omega) \rightarrow \log f$ and $M''(\omega) \rightarrow \log f$ for pristine and irradiated SPE samples in the frequency range of 1–100 kHz at ambient temperature. At low frequencies, the curve $M'(\omega)$ almost tends to zero for all the samples (pristine and irradiated) ascribed to the ionic conduction/removal of the electrode polarization effect at the low-frequency dispersion [38,39]. The spreading of $M'(\omega)$ over a broader region of frequencies showed a maximum value (M_∞).

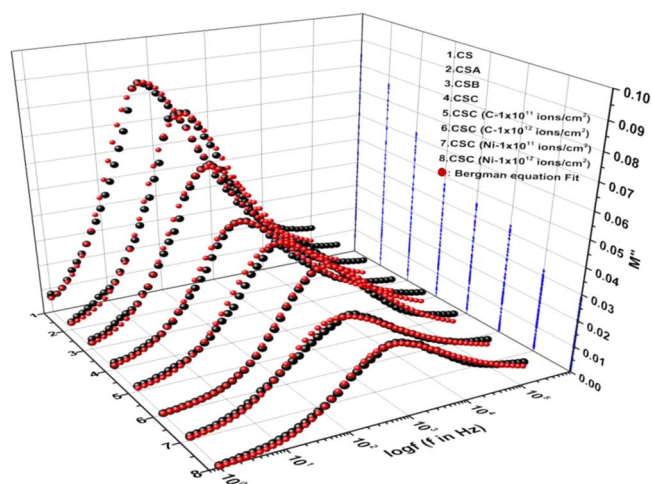


Fig. 7. Bergman equation fit of imaginary part of modulus versus log frequency for pristine and irradiated SPE with 60-MeV C^{+5} and 100-MeV Ni^{+7} ions at the fluences of 1×10^{11} and 1×10^{12} ions/cm², respectively.

This reveals the existence of a characteristic relaxation phenomenon in $M''(\omega) \rightarrow \log f$ plot along with a loss peak. In addition, no peak appearing in the plot of $M'(\omega) \rightarrow \log f$, which can be attributed to the fact that the real part of $M^*(\omega)$ resembles the real part of $\epsilon^*(\omega)$. A dominant reduction in the peak of $M''(\omega)$ upon irradiation was observed compared to that in the pristine sample, as revealed in Fig. 6 for nickel ion. This can be ascribed to the increase in local polymeric segmental motion and the mobility of the charge carriers [26,38,39] because of bond cleavage, as confirmed by the FTIR analysis. The decrease in the $M''(\omega)$ value for irradiated samples as a function of beam parameter could be caused by the increase in the $\epsilon'(\omega)$ values of the SPE samples.

The $M''(\omega)$ plot (Fig. 7) reveals a peak at a particular relaxation frequency f_{max} for all the SPE samples. The relaxation frequency correlates to the conductivity relaxation and mobility of charge carriers. The figure shows that the f_{max} shifted toward higher frequencies along with a decrease in the values of $M''(\omega)$, upon the inclusion of salt and increase in fluence of irradiation. These results indicate that the conductivity increased upon SHI irradiation because of the formation of conducting track and the increase in number of free radicals and charge carriers in the host matrix. Furthermore, the occurrence of relaxation peak in the frequency ($f < f_{max}$) region shows a long-range movement of charge carriers and reveals the presence of interfacial polarization. In contrast, the occurrence of a relaxation peak in the frequency ($f > f_{max}$) region shows a short-range transfer of free radicals and charge carriers within potential wells. In addition, the induced dipoles that no longer pursue the AC field revealed the elimination of the interfacial polarization effect.

The Kohlrausch–Williams–Watt (KWW) [40] stretched exponential function for the best curve fitting of $M''(\omega)$ in the frequency domain was modified by Bergman and can be expressed as follows [41]:

$$M''(\omega) = \frac{M''_{max}}{(1 - \beta_{KWW}) + \left[\left(\frac{\beta_{KWW}}{1 + \beta_{KWW}} \right) \left(\beta_{KWW} \left(\frac{f_{max}}{f} \right) + \left(\frac{f}{f_{max}} \right)^{\beta_{KWW}} \right) \right]}$$

where β_{KWW} is the Kohlrausch coefficient, with the condition $0 \leq \beta_{KWW} \leq 1$, and M''_{max} is the peak value of $M''(\omega)$. The value of $\beta_{KWW} = 1$ indicates the ideal Debye relaxation behavior and the value of β_{KWW} less than unity indicates non-Debye relaxation behavior. The red ball in Fig. 7 represents the fitted value of $M''(\omega)$, while the black ball corresponds to experimental data. The figure shows that there is a close agreement between the theoretical curve and experimental data. The precise fit to experimental data of $M''(\omega)$ with theoretically estimated values is obtained by calculating the figure of merit (FOM). A summary of the $M''(\omega)$ parameters β_{KWW} , M''_{max} , and f_{max} calculated by the Bergman equation is listed in Table 2 for each plot of SPE. The values of β_{KWW} for all SPE films revealed non-Debye relaxation behavior. In addition, the concentration, ion species, and ion beam fluence dependent values of M''_{max} decreased and shifted toward higher frequencies. This can be ascribed to the increase in conductivity of SPE because of the increased charge carriers (i.e., Ag^+ ions and polymer radicals) owing to the scissioning of the polymer chain and release of trapped charges. The plot of $M''(\omega)$ shows a peak, whereas the $\epsilon''(\omega)$ plot (see Fig. 8) does not show any peak, indicating a conduction

Table 2
Parameter values obtained from the Bergman equation fit.

Sample	M''_{max}	f_{max}	β_{KWW}	FOM (%)
Pristine CS	0.13200	178.50000	0.42121	5.32
Pristine CSA	0.11798	289.11018	0.47594	7.17
Pristine CSB	0.09673	310.74838	0.42400	7.07
Pristine CSC	0.07401	370.35681	0.40418	6.69
CSC (C- 1×10^{11} ions/cm ²)	0.07120	580.14059	0.36286	6.94
CSC (C- 1×10^{12} ions/cm ²)	0.06554	1000.19030	0.40534	4.81
CSC (Ni- 1×10^{11} ions/cm ²)	0.05102	590.16188	0.34333	5.96
CSC (Ni- 1×10^{12} ions/cm ²)	0.04533	1119.83290	0.37309	5.31

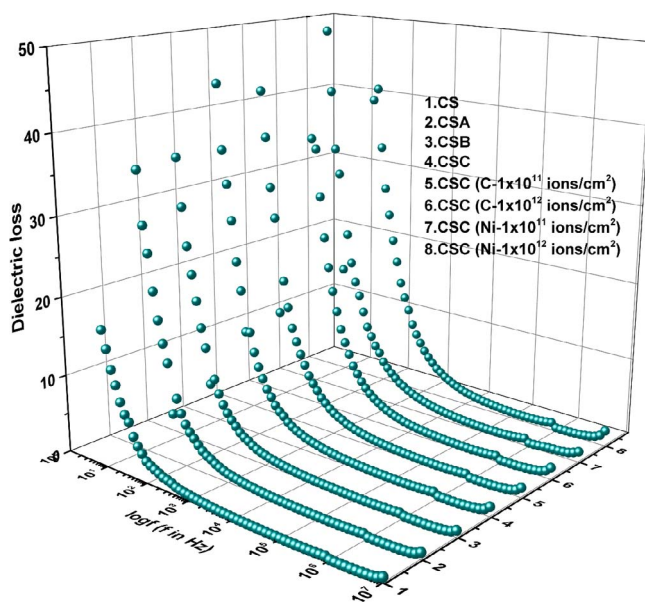


Fig. 8. Plot of dielectric losses versus log frequency for pristine and irradiated SPE with 60-MeV C^{+5} and 100-MeV Ni^{+7} ions at the fluences of 1×10^{11} and 1×10^{12} ions/cm², respectively.

process and that the motion of ions and polymeric radicals are potentially coupled. These results are attributed to structural degradation and defects created upon irradiation. There is also a strong consonance between modulus and FTIR data. Additionally, the $M''(\omega)$ spectrum for all films was normalized using the parameters extracted from the Bergman fitting, thereby yielding master-normalized spectra of $(M''/M''_{max}) \rightarrow (f/f_{max})$, as represented in Fig. 9. This plot shows that the relaxation mechanism in SPE matrix is not affected by dopant level or irradiation parameters.

The frequency-dependent AC conductivity (σ_{ac}) at constant temperature of the SPE samples was obtained from the measured values of C_p and $\tan \delta$. In addition, σ_{ac} obeys the “Jonscher universal power law” expressed as follows:

$$\sigma(\omega, T) = \sigma_{dc} + B\omega^s$$

where σ_{dc} is the frequency-independent plateau at low frequency, which is commonly known as the dc conductivity of the material; B is the pre-exponential parameter; and s is the dimensionless temperature-dependent fractional exponent ranging between 0 and 1. The electrical

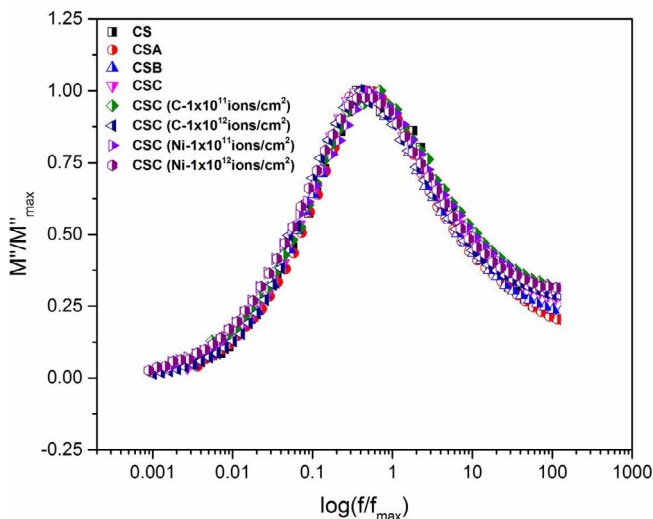


Fig. 9. Scaling behavior of imaginary part of modulus for all the SPE samples.

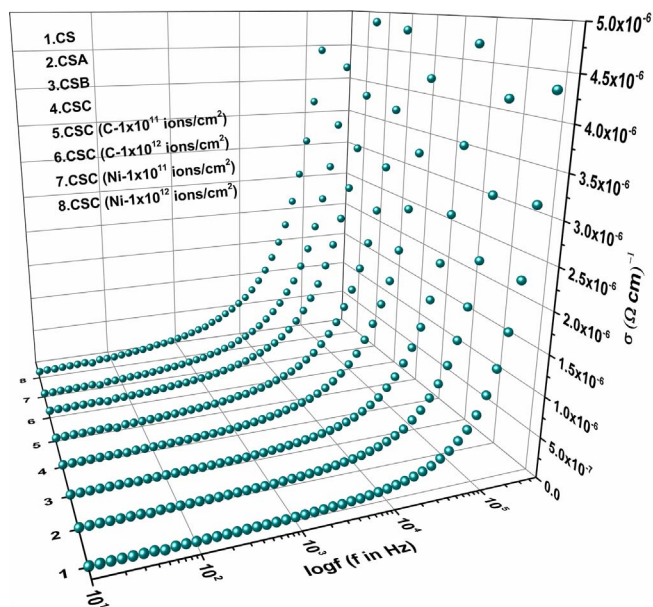


Fig. 10. Plot of conductivity versus log frequency for pristine and irradiated SPE with 60-MeV C^{+5} and 100-MeV Ni^{+7} ions at the fluences of 1×10^{11} and 1×10^{12} ions/cm², respectively.

conductivity is frequency independent or dc type for $s=0$, and it depends on the frequency or AC type for $s > 0$.

Fig. 10 shows the graph of $\sigma \rightarrow \log f$ for all the SPE samples under investigation. At low frequency, constant plateau-like region is seen owing to the long-range drift of charges controlled by an external field. For CS, the value of σ_{dc} was $\sim 3 \times 10^{-8}$ S/cm at 10 Hz, as seen in Fig. 11, while at 10 Hz, σ_{dc} for CSC irradiated with carbon and nickel ions at a fluence of 1×10^{12} ions per cm² attained a value of $\sim 2.78 \times 10^{-7}$ and $\sim 3.46 \times 10^{-7}$ S/cm, respectively. Optical studies showed that the reduction of Ag^+ to Ag^0 is greater for 1×10^{12} ions/cm² fluence for both ions. In general, the values of σ_{dc} of electrolyte system are higher in the presence of nanocomposites [42]. This trend was observed in our case also; the increased σ_{dc} conductivity implies the disruption of the crystallinity yield and increase in the mobility of charge carriers through the amorphous phase. With the increase in frequency, the mean drift range of charge carriers decreased, and at the critical frequency (f_c), the conductivity obeys the power law $\sigma(\omega) \approx \omega^n$. In disordered or inhomogeneous materials, this trend is generally observed. The AC conductivity of irradiated SPE samples was found to be

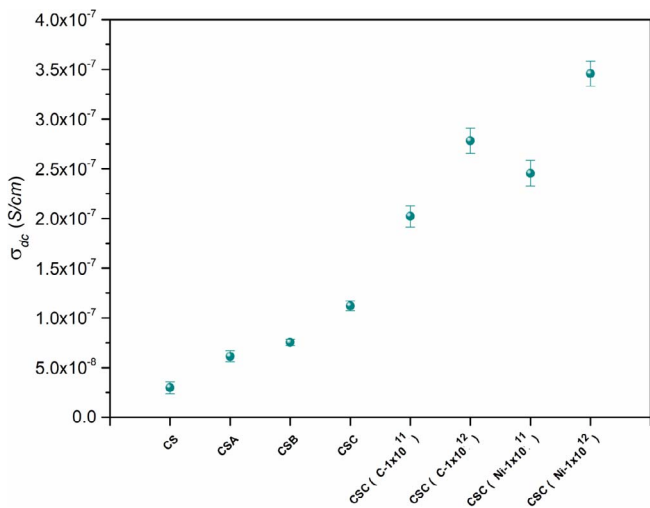


Fig. 11. Variation in dc conductivity as a function of salt concentration and ion fluence.

moderately higher than that of pristine. The increase in conductivity can be ascribed to the increased free volume in the polymer matrix, scissioning of macromolecule chain, structural degradation, creation of defects, and carbon-rich localized network [13,14,36]. Furthermore, the increase in conductivity for nickel ion irradiation is more pronounced and increased with the increase in ion fluence, because the SPE system follows the universal law. The hopping behavior of the charge carriers can be explained by the exponent s . The slope ($d\sigma_{ac}/d\omega$) obtained from the plot of $\log \sigma_{ac} \rightarrow \log \omega$ in higher frequency region (where the space charge polarization is negligible) gives the value of s , as shown in Fig. 12. To achieve the best fitting, the linear regression method was used to obtain precise values of s , and the values of regression co-efficient R^2 ranging between 0.97 and 0.98 revealed a reliable accuracy. The value of s for all the SPE films was in the range of 0.98–0.83, with a standard deviation of ± 0.02 . Consequently, the conduction phenomenon in the SPE matrix is because of the hopping of charge carriers, and it is AC type [37].

3.5. Surface morphology

Fig. 13(a–d) shows the three-dimensional scanned topographical images of selected SPE samples using atomic force microscopy (AFM) in an area of $5 \times 5 \mu m^2$. The AFM image for CS (pristine chitosan) exhibited hillock-like structures (see Fig. 13(a)). The average surface roughness (R_a) was found to be 11.2 nm. For the CSC film, R_a attained a value of 101.7 nm, which implies an increase in the roughness after embedding the dopant. The CSC SPE sample irradiated with carbon and nickel ions at a fluence of 1×10^{12} ions/cm² showed substantial modification in surface roughness, as shown in Fig. 13(c and d). The value of R_a for CSC samples exposed to carbon and nickel ions decreased to 30.1 and 8.9 nm, respectively. Upon SHI irradiation, the surface became significantly smooth for both ions. In addition, the decrease in R_a in heavier nickel ions was more pronounced than that in carbon ions. This implies that the hitting impact and localized surface diffusion for nickel ions on the polymeric surface is more than those for carbon ions. Meanwhile, the breakage of hillock structure due to nickel ions was dominant and resulted in a smoother surface than carbon ions.

4. Conclusions

SPE-based biodegradable chitosan and silver salt were synthesized and exposed to 60-MeV carbon and 100-MeV nickel ions at different fluences at ambient temperature. This study shows that the optical and electrical properties of SPE system were modified by high energetic ions. The FTIR spectroscopic tests performed to study the effect of MeV ions on various band structure indicated scissioning and structural degradation. Hence, the SPE matrix is *carbonized*, and this resulted in decrease in E_g . Amendment in optical behavior is directly related to the structural deterioration and/or ion-induced defects in the matrix. Consequently, the AC electric response moderately changed upon SHI irradiation. The increase in $\epsilon''(\omega)$, $M''(\omega)$, and σ_{dc} was ascribed to the reduction of Ag^+ to Ag^0 , and the enhancement in ionic conduction was due to structural modification. The fitting of $M''(\omega)$ revealed non-Debye relaxation process in the SPE system. The present system ascribed to the hopping of charge carrier transport mechanism, and σ_{ac} obeys the power law. AFM studies showed considerable decrease in R_a because of the large effect of energetic ions. Moreover, various studies have shown that heavier nickel ions more effectively affect the physicochemical properties than the lighter carbon ions of the SPE matrix. Consequently, in addition to ion fluence, ion properties (i.e., mass, size, and energy) also play an important role in enhancing the environment of the friendly biodegradable matrix, which can be potentially used as electrolytes.

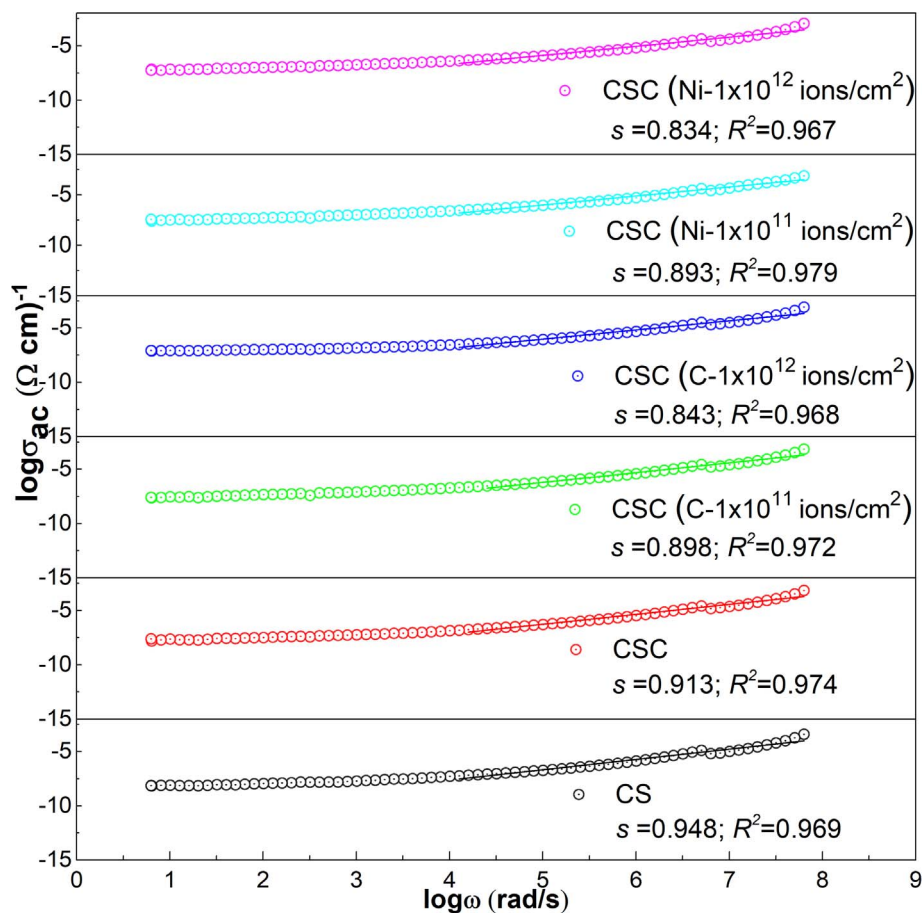


Fig. 12. Plot of log ac conductivity versus log angular frequency for all the SPE samples.

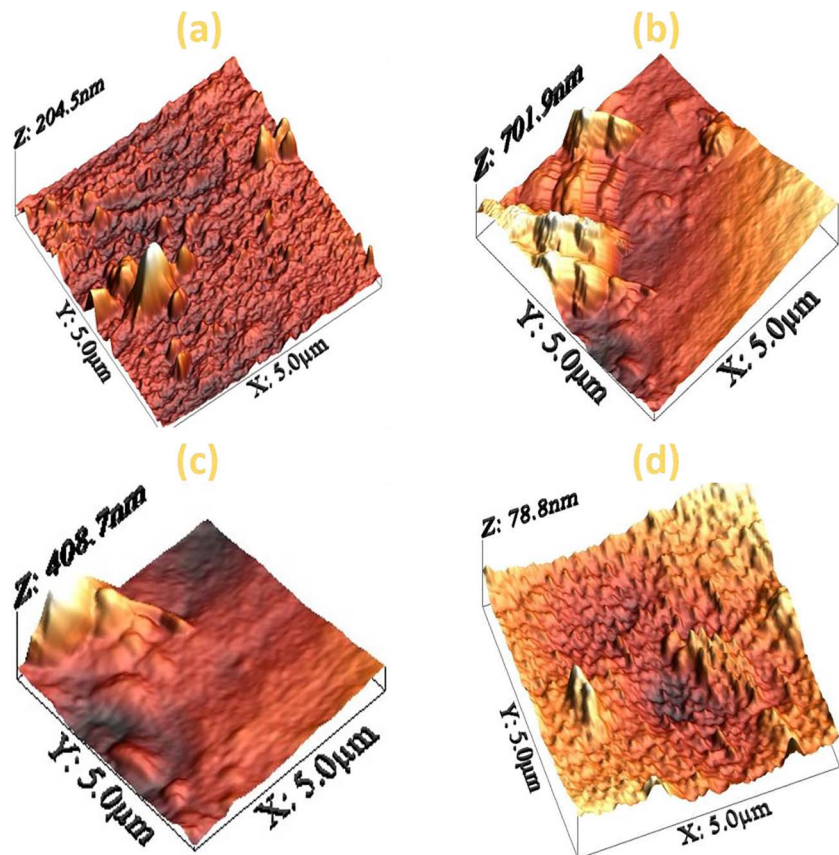


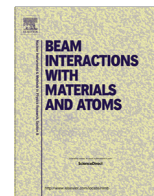
Fig. 13. AFM images of CS (a) and CSC (b) films and CSC films irradiated with 60-MeV C $^{+5}$ ions (c), 100-MeV Ni $^{+7}$ ions (d) at the fluence of 1×10^{12} ions/cm 2 .

Acknowledgments

The authors are grateful to IUAC, New Delhi, for providing irradiation/characterization facilities and financial support. One of the authors (GBP) is thankful to the DST-PURSE program for providing fellowship.

References

- [1] S.B. Aziz, Z.H.Z. Abidin, A.K. Arof, Effect of silver nanoparticles on the DC conductivity in chitosan–silver triflate polymer electrolyte, *Phys. B Condens. Matter.* 405 (2010) 4429–4433, <http://dx.doi.org/10.1016/j.physb.2010.08.008>.
- [2] S.B. Aziz, Z.H.Z. Abidin, Electrical conduction mechanism in solid polymer electrolytes: new concepts to arrhenius equation, *J. Soft Matter.* 2013 (2013) 1–8, <http://dx.doi.org/10.1155/2013/323868>.
- [3] N.M. Morni, A.K. Arof, Chitosan–lithium triflate electrolyte in secondary lithium cells, *J. Power Sources* 77 (1999) 42–48, [http://dx.doi.org/10.1016/S0378-7753\(98\)00170-0](http://dx.doi.org/10.1016/S0378-7753(98)00170-0).
- [4] N.M. Morni, N.S. Mohamed, A.K. Arof, Silver nitrate doped chitosan acetate films and electrochemical cell performance, *Mater. Sci. Eng., B* 45 (1997) 140–146, [http://dx.doi.org/10.1016/S0921-5107\(96\)02023-5](http://dx.doi.org/10.1016/S0921-5107(96)02023-5).
- [5] K. Rama Mohan, V.B.S. Achari, V.V.R.N. Rao, A.K. Sharma, Electrical and optical properties of (PEMA/PVC) polymer blend electrolyte doped with NaClO₄, *Polym. Test.* 30 (2011) 881–886, <http://dx.doi.org/10.1016/j.polymertesting.2011.08.010>.
- [6] S.S. Rao, K.V.S. Rao, M. Shareefuddin, U.V.S. Rao, S. Chandra, Ionic conductivity and battery characteristic studies on PEO + AgNO₃ polymer electrolyte, *Solid State Ionics* 67 (1994) 331–334, [http://dx.doi.org/10.1016/0167-2738\(94\)90026-4](http://dx.doi.org/10.1016/0167-2738(94)90026-4).
- [7] S. Liang, J. Yang, X. Zhang, Y. Bai, The thermal-electrical properties of polyvinyl alcohol/AgNO₃ films, *J. Appl. Polym. Sci.* 122 (2011) 813–818, <http://dx.doi.org/10.1002/app.34060>.
- [8] N.E.A. Shuhaimi, N.A. Alias, M.Z. Kufian, S.R. Majid, A.K. Arof, Characteristics of methyl cellulose-NH₄NO₃-PEG electrolyte and application in fuel cells, *J. Solid State Electrochem.* 14 (2010) 2153–2159, <http://dx.doi.org/10.1007/s10008-010-1099-4>.
- [9] C.K.S. Pillai, W. Paul, C.P. Sharma, Chitin and chitosan polymers: Chemistry, solubility and fiber formation, *Prog. Polym. Sci.* 34 (2009) 641–678, <http://dx.doi.org/10.1016/j.progpolymsci.2009.04.001>.
- [10] D. Enescu, C.E. Olteanu, Functionalized chitosan and its use in pharmaceutical, biomedical, and biotechnological research, *Chem. Eng. Commun.* 195 (2008) 1269–1291, <http://dx.doi.org/10.1080/00986440801958808>.
- [11] D.J. Macquarrie, J.J.E. Hardy, Applications of functionalized chitosan in catalysis, *Ind. Eng. Chem. Res.* 44 (2005) 8499–8520, <http://dx.doi.org/10.1021/ie050007v>.
- [12] Y.N. Sudhakar, M. Selvakumar, D.K. Bhat, LiClO₄-doped plasticized chitosan and poly(ethylene glycol) blend as biodegradable polymer electrolyte for super-capacitors, *Ionics (Kiel)*. 19 (2013) 277–285, <http://dx.doi.org/10.1007/s11581-012-0745-5>.
- [13] G.B. Patel, S. Bhavsar, N.L. Singh, F. Singh, P.K. Kuliya, SHI induced modification in structural, optical, dielectric and thermal properties of poly ethylene oxide films, *Nucl. Instrum. Methods Phys. Res. Sect. B Beam Interact. Mater. Atoms.* 379 (2016) 156–161, <http://dx.doi.org/10.1016/j.nimb.2016.04.018>.
- [14] N.L. Singh, A. Sharma, D.K. Avasthi, V. Shrinet, Temperature and frequency dependent electrical properties of 50 MeV Li³⁺ ion irradiated polymeric blends, *Radiat. Eff. Defects Solids* 160 (2005) 99–107, <http://dx.doi.org/10.1080/10420150500116649>.
- [15] E. Yulianti, A.K. Karo, L. Susita, Sudaryanto synthesis of electrolyte polymer based on natural polymer chitosan by ion implantation technique, *Procedia Chem.* 4 (2012) 202–207, <http://dx.doi.org/10.1016/j.proche.2012.06.028>.
- [16] G. Hirankumar, S. Selvasekarapandian, M.S. Bhuvanewari, R. Baskaran, M. Vijayakumar, Ag⁺ ion transport studies in a polyvinyl alcohol-based polymer electrolyte system, *J. Solid State Electrochem.* 10 (2006) 193–197, <http://dx.doi.org/10.1007/s10008-004-0612-z>.
- [17] J.F. Ziegler, M.D. Ziegler, J.P. Biersack, SRIM – The stopping and range of ions in matter (2010), *Nucl. Instrum. Methods Phys. Res. Sect. B Beam Interact. Mater. Atoms.* 268 (2010) 1818–1823, <http://dx.doi.org/10.1016/j.nimb.2010.02.091>.
- [18] S.-F. Wang, L. Shen, W.-D. Zhang, Y.-J. Tong, Preparation and mechanical properties of chitosan/carbon nanotubes composites, *Biomacromolecules* 6 (2005) 3067–3072, <http://dx.doi.org/10.1021/bm050378v>.
- [19] V.K. Sharma, R.A. Yngard, Y. Lin, Silver nanoparticles: Green synthesis and their antimicrobial activities, *Adv. Colloid Interface Sci.* 145 (2009) 83–96, <http://dx.doi.org/10.1016/j.cis.2008.09.002>.
- [20] S. Kumar-Krishnan, E. Prokhorov, M. Ramirez, M.A. Hernandez-Landaverde, D.G. Zarate-Triviño, Y. Kovalenko, et al., Novel gigahertz frequency dielectric relaxations in chitosan films, *Soft Matter* 10 (2014) 8673–8684 [10.1039/C4SM01804D](https://doi.org/10.1039/C4SM01804D).
- [21] H. Wang, W. Li, Y. Lu, Z. Wang, Studies on chitosan and poly(acrylic acid) inter-polymer complex. I. Preparation, structure, pH-sensitivity, and salt sensitivity of complex-forming poly(acrylic acid): Chitosan semi-interpenetrating polymer network, *J. Appl. Polym. Sci.* 65 (1997) 1445–1450, [http://dx.doi.org/10.1002/\(SICI\)1097-4628\(19970822\)65:8<1445::AID-APP1>3.0.CO;2-G](http://dx.doi.org/10.1002/(SICI)1097-4628(19970822)65:8<1445::AID-APP1>3.0.CO;2-G).
- [22] Y. Dong, C. Xu, J. Wang, M. Wang, Y. Wu, Y. Ruan, Determination of degree of substitution for N-acetylated chitosan using IR spectra, *Sci. China, Ser. B: Chem.* 44 (2001) 216–224, <http://dx.doi.org/10.1007/BF02879541>.
- [23] C. Song, H. Yu, M. Zhang, Y. Yang, G. Zhang, Physicochemical properties and antioxidant activity of chitosan from the blowfly *Chrysomya megacephala* larvae, *Int. J. Biol. Macromol.* 60 (2013) 347–354, <http://dx.doi.org/10.1016/j.ijbiomac.2013.05.039>.
- [24] L. Vinet, A. Zhedanov, A “missing” family of classical orthogonal polynomials, *J. Phys. A Math. Theor.* 44 (2011) 85201, <http://dx.doi.org/10.1088/1751-8113/44/8/085201>.
- [25] J.R. Fried, *Polymer Science and Technology*, Prentice Hall PTR, Upper Saddle River, New Jersey 07458, 1995.
- [26] S.B. Aziz, Z.H.Z. Abidin, A.K. Arof, Influence of silver ion reduction on electrical modulus parameters of solid polymer electrolyte based on chitosan-silver triflate electrolyte membrane, *Express Polym. Lett.* 4 (2010) 300–310, <http://dx.doi.org/10.3144/expresspolymlett.2010.38>.
- [27] U. Kreibitz, G. Bour, A. Hilger, M. Gartz, Optical Properties of Cluster–Matter: Influences of Interfaces, *Phys. Status Solidi.* 175 (1999) 351–366, [http://dx.doi.org/10.1002/\(SICI\)1521-396X\(199909\)175:1<351::AID-PSSA351>3.0.CO;2-U](http://dx.doi.org/10.1002/(SICI)1521-396X(199909)175:1<351::AID-PSSA351>3.0.CO;2-U).
- [28] M.F. Zaki, Gamma-induced modification on optical band gap of CR-39 SSNTD, *J. Phys. D Appl. Phys.* 41 (2008) 175404, <http://dx.doi.org/10.1088/0022-3727/41/17/175404>.
- [29] V. Kumar, R.G. Sonkawade, S.K. Chakarvarti, P. Kuliya, K. Kant, N.L. Singh, et al., Study of optical, structural and chemical properties of neutron irradiated PADC film, *Vacuum* 86 (2011) 275–279, <http://dx.doi.org/10.1016/j.vacuum.2011.07.001>.
- [30] J. Tauc, R. Grigorovici, A. Vancu, Optical Properties and Electronic Structure of Amorphous Germanium, *Phys. Status Solidi* 15 (1966) 627–637, <http://dx.doi.org/10.1002/pssb.19660150224>.
- [31] J. Robertson, E. O'Reilly, Electronic and atomic structure of amorphous carbon, *Phys. Rev. B* 35 (1987) 2946–2957, <http://dx.doi.org/10.1103/PhysRevB.35.2946>.
- [32] N. Vukmirović, L.-W. Wang, Density of states and wave function localization in disordered conjugated polymers: a large scale computational study, *J. Phys. Chem. B* 115 (2011) 1792–1797, <http://dx.doi.org/10.1021/jp1114527>.
- [33] G. Compagnini, G. Foti, R. Reitano, G. Mondio, Graphitic clusters in hydrogenated amorphous carbon induced by keV-ion irradiation, *Appl. Phys. Lett.* 57 (1990) 2546–2548, <http://dx.doi.org/10.1063/1.103832>.
- [34] D. Fink, W.H. Chung, R. Klett, A. Schmoltd, J. Cardoso, R. Montiel, et al., Carbonaceous clusters in irradiated polymers as revealed by UV-Vis spectrometry, *Radiat. Eff. Defects Solids* 133 (1995) 193–208, <http://dx.doi.org/10.1080/10420159508223990>.
- [35] D. Fink, R. Klett, L.T. Chadderton, J. Cardoso, R. Montiel, H. Vazquez, et al., Carbonaceous clusters in irradiated polymers as revealed by small angle X-ray scattering and ESR, *Nucl. Instrum. Methods Phys. Res. Sect. B Beam Interact. Mater. Atoms.* 111 (1996) 303–314, [http://dx.doi.org/10.1016/0168-583X\(95\)01433-0](http://dx.doi.org/10.1016/0168-583X(95)01433-0).
- [36] N.L. Singh, A. Qureshi, F. Singh, D.K. Avasthi, Effect of swift heavy ion irradiation on dielectrics properties of polymer composite films, *Mater. Sci. Eng., B* 137 (2007) 85–92, <http://dx.doi.org/10.1016/j.mseb.2006.10.013>.
- [37] A.K. Jonscher, *Dielectric Relaxation in Solids*, Chesla Dielectric Press, London, 1983.
- [38] G.M. Tsangaris, G.C. Psarras, N. Kouloumbi, Electric modulus and interfacial polarization in composite polymeric systems, *J. Mater. Sci.* 33 (1998) 2027–2037, <http://dx.doi.org/10.1023/A:1004398514901>.
- [39] Y. Fu, K. Pathmanathan, J.R. Stevens, Dielectric and conductivity relaxation in poly(propylene glycol)–lithium triflate complexes, *J. Chem. Phys.* 94 (1991) 6323–6329, <http://dx.doi.org/10.1063/1.460420>.
- [40] G. Williams, D.C. Watts, Non-symmetrical dielectric relaxation behaviour arising from a simple empirical decay function, *Trans. Faraday Soc.* 66 (1970) 80, <http://dx.doi.org/10.1039/TF9706600080>.
- [41] R. Bergman, General susceptibility functions for relaxations in disordered systems, *J. Appl. Phys.* 88 (2000) 1356–1365, <http://dx.doi.org/10.1063/1.373824>.
- [42] A.S. Bhatt, D.K. Bhat, M.S. Santosh, C. Tai, Chitosan/NiO nanocomposites: a potential new dielectric material, *J. Mater. Chem.* 21 (2011) 13490, <http://dx.doi.org/10.1039/c1jm12011e>.



SHI induced modification in structural, optical, dielectric and thermal properties of poly ethylene oxide films



Gnansagar B. Patel^a, Shilpa Bhavsar^a, N.L. Singh^{a,*}, F. Singh^b, P.K. Kulriya^b

^aDepartment of Physics, The M.S. University of Baroda, Vadodra 390002, India

^bInter University Accelerator Centre, Aruna Asaf Ali Marg, New Delhi 110067, India

ARTICLE INFO

Article history:

Received 10 November 2015

Received in revised form 7 April 2016

Accepted 7 April 2016

Available online 25 April 2016

Keywords:

Poly ethylene oxide

SHI irradiation

XRD

UV–Vis

SEM

ABSTRACT

Poly ethylene oxide (PEO) films were synthesized by solution cast method. These self-standing films were exposed with 60 MeV C⁺⁵ ion and 100 MeV Ni⁺⁷ ion at different fluences. SHI induced effect was investigated by employing various techniques. The crystalline size decreased upon irradiation as observed from XRD analysis. FTIR analysis reveals the decrement in the peak intensity upon irradiation. Tauc's method was used to determine the optical band gap (E_g), which shows decreasing trends with increase of fluence. The dielectric properties were investigated in the frequency range 10 Hz to 10 MHz for unirradiated and irradiated films. The dielectric constant remains same for the broad-spectrum of frequency and increases at lower frequency. The dielectric loss also moderately influence as a function of frequency due to irradiation. DSC analysis validated the results of XRD. Scanning electron microscopy (SEM) reveals that there is significant change in the surface morphology due to irradiation.

© 2016 Elsevier B.V. All rights reserved.

1. Introduction

Polymers with very high molecular weight having vast applications in all field of modern life. The physical and chemical properties of polymers are being modified by neutron, electron, gamma rays and ion beam irradiation for desired applications. Investigation of polymer modification through energetic ions is extremely important because of versatile functional desire of polymers in radiation backgrounds like nuclear reactor, ballistic capsule, high energy particle accelerators, sterilization irradiators, etc. [1,2]. Swift heavy ion (SHI) beam causes irreversible modification of the structural, optical, dielectric, thermal and surface properties through depositing the energy in materials at macro-level. There may be breaking of covalent bond and chain scissioning and as a result creation of carbon cluster and cross-linking of polymeric chains in the polymer matrix. The extent of modification of these properties depends on the nature of polymers and irradiation condition, like charge, mass, energy and fluence of incident ion [3].

Poly ethylene oxide (PEO) is a semi crystalline, biodegradable, nontoxic and water soluble polymer having versatile applications. Many efforts had been devoted in the past few years to modify the properties of PEO for synthesis of hydrogel and to tailor the prop-

erties of PEO base electrolytes by gamma, ultraviolet and ion beam irradiation [4–11].

In this work, comparative analysis of 60 MeV C⁺⁵ and 100 MeV Ni⁺⁷ ions induced modifications in structural, optical, dielectric and thermal behavior of PEO polymer film has been discussed as a function of ion beam parameters.

2. Materials and methods

2.1. Sample preparation and SHI irradiation

Self-standing PEO films of thickness about 200 μm were prepared by solution casting method. The PEO ($\text{CH}_2\text{-CH-O}$)_n was purchased from Alfa Aesar in powder form. It was used without further purification and dissolved in water by stirrer at ambient temperature. The solution was cast on Teflon petridish to form PEO film. The films were irradiated at different fluences using 60 MeV C⁺⁵ and 100 MeV Ni⁺⁷ ions having beam current of 0.5 pA (particles per nano-ampere). The beam was scanned on the film in xy-plane of area (1 × 1) cm² using the 15UD Pelletron at the Inter University Accelerator Center (IUAC), New Delhi. The SRIM 2013 [12] code was used to calculate range and energy loss of C⁺⁵ and Ni⁺⁷ ions in PEO film. The projected range (R_p) are ≈ 149.0 and 34.0 μm , the electronic stopping power (S_e) ≈ 256 and 4161 keV/ μm , and the nuclear stopping power (S_n) ≈ 0.15 and 6.79 keV/ μm , for C⁺⁵ ion and Ni⁺⁷ ion, respectively.

* Corresponding author.

E-mail address: nl.singh-phy@msubaroda.ac.in (N.L. Singh).

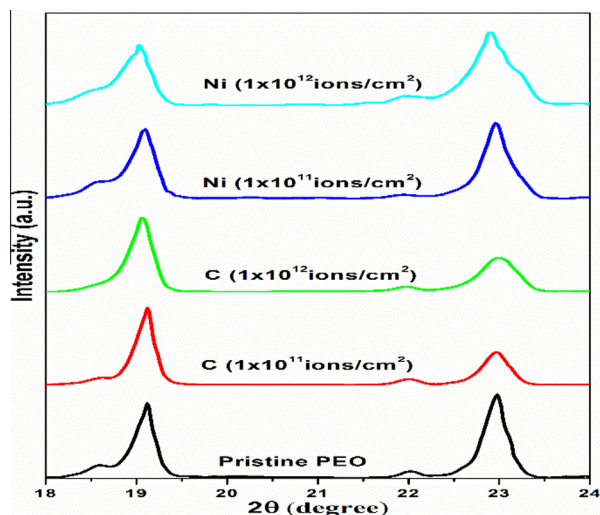


Fig. 1. XRD spectra of PEO irradiated with 60 MeV C^{+5} and 100 MeV Ni^{+7} ions at the fluences of 1×10^{11} and 1×10^{12} ions/cm².

2.2. Sample characterization

The structural modifications of the film was examined with the help of powder X-ray diffractometer and the spectra were recorded for Bragg angle of $18^\circ < 2\theta < 24^\circ$ with Cu K_α radiation (Bruker D8-Avance diffractometer). The FTIR spectroscopy was performed in wavenumber range 500–3500 cm^{-1} in the transmission mode (JASCO-4100). The FTIR spectrum with hundred times scanned averaged were taken with a resolution of 4 cm^{-1} . The UV-visible spectra were studied in the region of 200–800 nm to observe optical properties (Hitachi Model U-3300 spectrometer). The frequency dependent dielectric properties of pristine and irradiated films were carried out by employing impedance gain/phase analyzer in the frequency range 10 Hz to 10 MHz at ambient temperature (Solartron SI-1260). The differential scanning calorimetry (DSC) analysis was performed by heating 1–2 mg of the sample in the temperature range 35–90 °C in nitrogen environment at the rate of 10 °C/min (SII EXSTAR 6000). The surface morphology was studied using SEM (Scanning electron microscopy, Hitachi SU1510).

3. Results and discussion

3.1. X-ray diffraction analysis

The XRD patterns are presented in Fig. 1 to investigate the structural changes in irradiated (with C^{+5} and Ni^{+7} ions) PEO films. Two peaks are observed at 2θ angle 19.12° and 22.98°, which indicate semi-crystalline nature of PEO.

The Scherrer's formula was used to determine the crystallite size (L) [13],

$$L = \frac{K\lambda}{\beta_{1/2} \cos \theta}$$

Table 1

Variation of crystallite size at different fluences of 60 MeV C^{+5} and 100 MeV Ni^{+7} ions irradiation for PEO polymer.

Ion fluence (ions/cm ²)	Carbon (60 MeV)		Nickel (100 MeV)	
	FWHM (in radians)	Crystallite Size (in nm)	FWHM (in radians)	Crystallite Size (in nm)
Pristine PEO	0.0048	29.0 ± 2.5	0.0048	29.0 ± 2.5
1×10^{11}	0.0050	28.3 ± 5.4	0.0057	24.2 ± 0.3
1×10^{12}	0.0068	21.4 ± 4.8	0.0076	18.5 ± 2.3

where $\lambda = 1.5418 \text{ \AA}$ is the incident X-ray wavelength, K is a constant varied from 0.89 to 1.39, $\beta_{1/2}$ is the FWHM of the diffraction peak and θ is the Bragg angle (in radian). In this calculation, $K = 0.89$ was taken as per literature. The calculated values of L for unirradiated and irradiated PEO films with C^{+5} and Ni^{+7} ions at different fluences are listed in Table 1. The full width at half maximum (FWHM) increases and hence reduction in crystallite size is observed due to irradiation. In consequence of C^{+5} and Ni^{+7} ions irradiation, the crystallite size of PEO reduced to ~26.2% and ~36.3%, respectively. It reveals that the heavier mass ion caused more amorphization of the material than that of lighter one and resulted in the carbonization and production of low molecular weight radicals. This result is in agreement with the DSC result.

3.2. FTIR analysis

The vibration mode of PEO was studied by means of infrared spectroscopy in transmission mode. Fig. 2 presents the FTIR spectra of the unirradiated and irradiated PEO films using C^{+5} and Ni^{+7} ions. The pristine PEO shows bands at 529 cm^{-1} (C–O–C bending vibrations), 946 cm^{-1} (C–O–C vibration mode), while 1050 cm^{-1} and 1150 cm^{-1} (C–O–C stretching vibrations). The vibration bands appeared at 846 cm^{-1} , 1275 cm^{-1} , 1350 cm^{-1} , 1462 cm^{-1} are due to rocking mode, twisting mode, wagging mode and scissoring mode, respectively for CH_2 vibrational band [14]. The strong wide absorption band appeared in the region of 2950–2700 cm^{-1} , attributed to C–H stretching modes (symmetric and asymmetric) of the CH_2 group [15].

There is no significant shifting of vibration mode and no new mode of vibration appeared due to irradiation. This mean that the overall polymeric structure remains same. However, there is a reduction in transmission intensity of all vibration modes due to irradiation. It was also noticed that the decrease in peak intensity is more significant for Ni^{+7} ion compared to C^{+5} ion irradiated samples. This implies that heavier ion caused considerably more amorphization than that of lighter ion. The reduction in intensity is ascribed to the breakage of few carbonate bonds and –H abstraction from the backbone of the polymeric structure along with release of hydrogen and /or other volatile gases [16]. This resulted into the creation of low molecular weight segment and formation of conjugated bonds. These results validated with the results of XRD, UV-vis and dielectric analysis.

3.3. UV-visible analysis

SHI induced modification of optical property of unirradiated and irradiated (with C^{+5} and Ni^{+7} ions) PEO samples was investigated in the UV-visible region. The irradiation may create some defect in the material and cause the formation of unsaturated conjugated bonds and carbon clusters in the polymer matrix, which led to the modification in optical property. The optical absorbance was used to determine the change in the optical band gap (E_g) due to irradiation using following equation:

$$\alpha h\nu = B(h\nu - E_g)^n$$

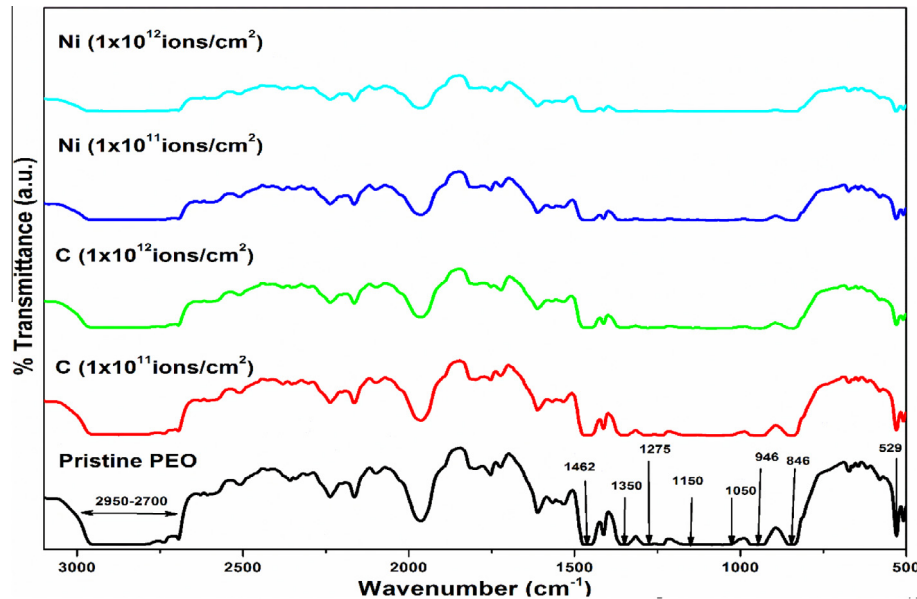


Fig. 2. FTIR spectra of PEO irradiated with 60 MeV C^{+5} and 100 MeV Ni^{+7} ions at the fluences of 1×10^{11} and 1×10^{12} ions/cm².

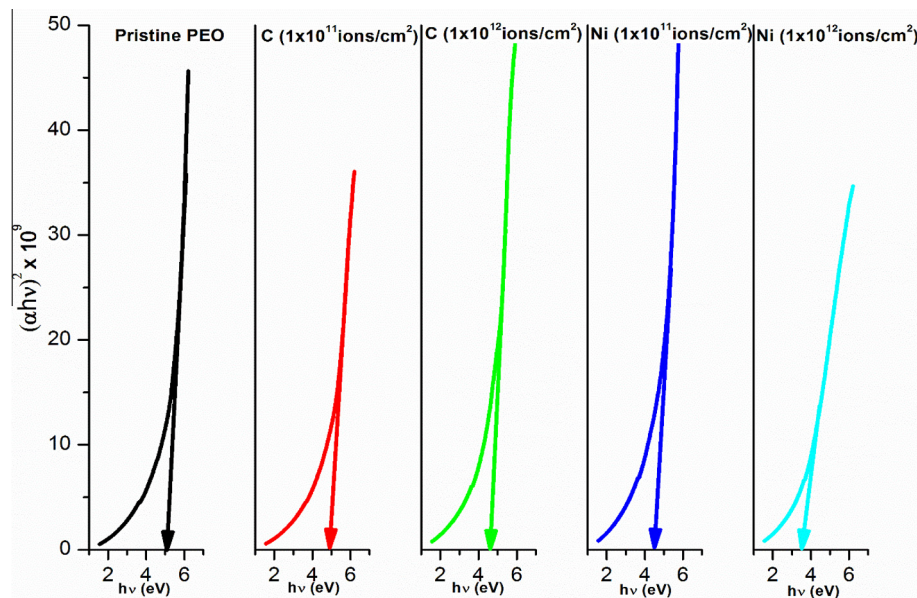


Fig. 3. Variation in $(\alpha h\nu)^{1/2}$ versus $(h\nu)$ for PEO films irradiated with 60 MeV C^{+5} and 100 MeV Ni^{+7} ions at the fluences of 1×10^{11} and 1×10^{12} ions/cm².

Table 2

Variation of optical energy band gap (E_g) and the number of carbon atoms per conjugation length (N) at different fluences of 60 MeV C^{+5} and 100 MeV Ni^{+7} ions irradiation for PEO polymer.

Ion fluence ions/cm ²	Carbon (60 MeV)		Nickel (100 MeV)	
	E_g (eV)	N	E_g (eV)	N
Pristine PEO	5.36	40.95	5.36	40.95
1×10^{11}	5.06	45.95	4.82	50.64
1×10^{12}	4.87	49.61	3.71	85.47

where $h\nu$ is photon energy, α is the absorption coefficient, B is constant, E_g is band gap, n is a constant having values 0.5, 1.5, 2 or 3 accounting for a direct and indirect allowed, direct and indirect forbidden optical transitions, respectively [17]. In the present investigation, allowed direct transition has been observed. The value of E_g

was obtained by extrapolating the graph of $(\alpha h\nu)^{1/2} \rightarrow h\nu$ on the photon energy axis and is shown in Fig. 3. The optical band gap for unirradiated and irradiated PEO films is tabulated in Table 2. It shows that on increasing the fluence of SHI irradiation, the optical band gap of the PEO polymer exhibits decreasing trends. Further, the attenuation in band gap is about $\sim 9.1\%$ and $\sim 30.8\%$ due to C^{+5} ion and Ni^{+7} ion irradiation, respectively. Hence, the change in the band gap due to Ni^{+7} ion is large as compared to C^{+5} ion. It may be attributed to a large amount of energy deposited by heavier and bigger size Ni^{+7} ion than the lighter and smaller size C^{+5} ion. The hydrogen and/or other volatile gases are released due to SHI irradiation because of scissioning of polymeric chain. This leads to increase in number density of carbon atoms in host material as compared to hydrogen atom, i.e. reduction in H/C atom ratio and formation of conjugated bond, resulted in the decrease of optical band gap [18].

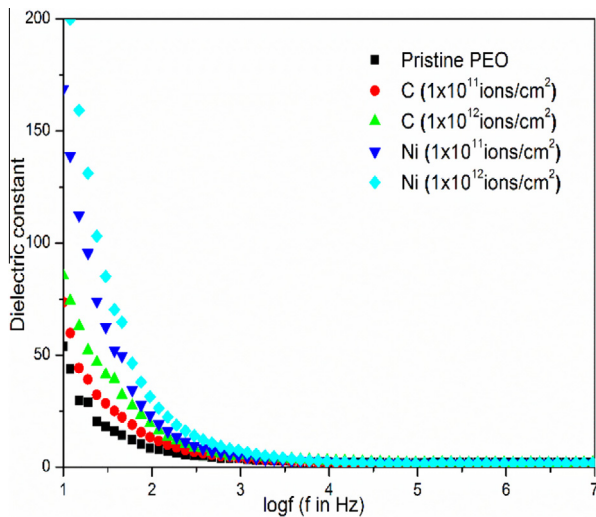


Fig. 4. Plot of dielectric constant versus log frequency for PEO films irradiated with 60 MeV C^{+5} and 100 MeV Ni^{+7} ions at the fluences of 1×10^{11} and 1×10^{12} ions/cm².

The number of carbon atoms (N) per conjugation length was calculated by using Robertson and O'Reilly formula, in which the structure of clusters was assumed to be C_6 [19]. Later on, Fink et al. modified the Robertson and O'Reilly's relation by considering the structure of cluster to be like a C_{60} [20]. The value of (N) was calculated employing Fink method by following formula [20],

$$E_g = \frac{34.3}{\sqrt{N}} \text{ eV}$$

The values of (N) are tabulated in Table 2. It indicates that the size of carbon cluster increases with increasing fluence. It is also revealed that the cluster size is bigger for Ni^{+7} ion than that of C^{+5} ion irradiated films. This is attributed to a large electronic energy loss due to Ni^{+7} ion. The modification in optical properties of the polymer is considerably depends on the profile of incident ion beam such as energy, mass and dimension.

3.4. Dielectric properties

The dielectric behaviors of the polymeric material are expressed by complex permittivity (ϵ^*) and is defined as [21],

$$\epsilon^*(\omega) = \epsilon'(\omega) - j\epsilon''(\omega)$$

Fig. 4 shows the graph of $\epsilon' \rightarrow \log f$ at ambient temperature for unirradiated and irradiated PEO films. The increase in dielectric constant in lower frequency is mainly due to the orientation of induced dipoles in the direction of the applied field. The dielectric constant decreases exponentially as frequency increases up to a frequency of 5 kHz and then became constant beyond this frequency. The induced dipoles are gradually failed to follow the direction of the applied field and decreases exponentially up to 5 kHz. The dielectric constant probably remains same beyond 5 kHz frequencies, attributed to constant motion of free charge carriers beyond these frequencies [22,23]. It is observed that the influence of Ni^{+7} ion on dielectric constant is more significant than the C^{+5} ion in the low frequency regions by virtue of high electronic energy loss due to Ni^{+7} ion. The increase in dielectric constant after SHI irradiation ascribe to scissioning of polymer chain and formation of few free radicals, unsaturation etc.

The dielectric materials have an ability to store the electrical energy. The dissipation factor ($\tan \delta$) expressed as the fraction of loss to storage:

$$\tan \delta = \epsilon'' / \epsilon'$$

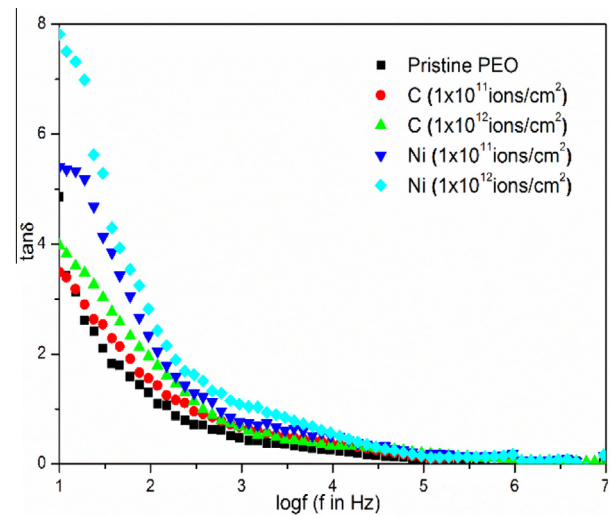


Fig. 5. Plot of dielectric loss versus log frequency for PEO films irradiated with 60 MeV C^{+5} and 100 MeV Ni^{+7} ions at the fluences of 1×10^{11} and 1×10^{12} ions/cm².

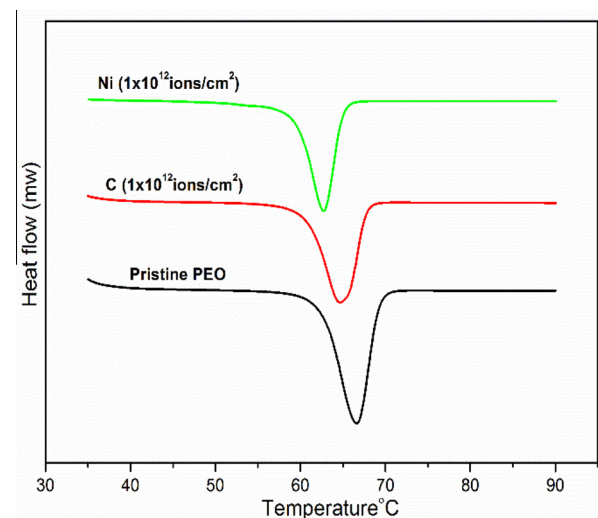


Fig. 6. DSC thermograms of PEO films irradiated with 60 MeV C^{+5} and 100 MeV Ni^{+7} ions at the fluences of 1×10^{11} and 1×10^{12} ions/cm².

Table 3

Variation in T_m and $X_c\%$ upon 60 MeV C^{+5} and 100 MeV Ni^{+7} ions irradiation at highest fluences.

Sample	(T_m)	$X_c\%$
Pristine PEO	66.6	80.5
Carbon (1×10^{12} ions/cm ²)	64.7	66.4
Nickel (1×10^{12} ions/cm ²)	62.7	50.1

Fig. 5 shows the graph of $\tan \delta \rightarrow \log f$ for unirradiated and irradiated PEO films. It illustrates that the dielectric loss decreases exponentially and then became almost independent at higher frequency. At higher frequencies, the induced dipoles no longer follow the reversing field and start lagging behind the oscillating field. Also, the dielectric loss increases moderately upon ion irradiation attributed to random orientations of polymeric radicals produced due to scissioning of polymer chains [24].

3.5. DSC analysis

DSC is a vital method to understand the thermal behavior and degree of crystallinity of the polymeric material. DSC thermograms

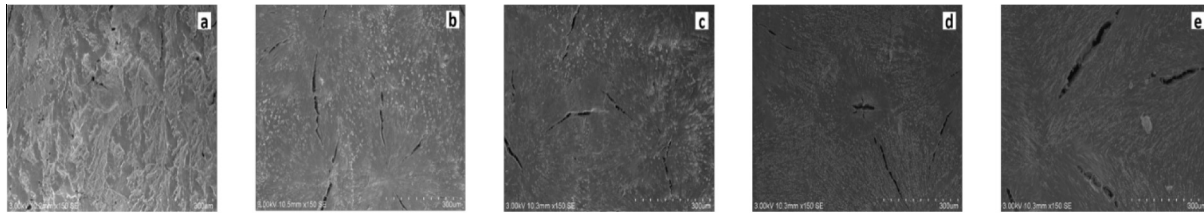


Fig. 7. SEM images of pristine PEO film (a), PEO films irradiated with 60 MeV C^{5+} at the fluences of 1×10^{11} ions/cm² (b) and 1×10^{12} ions/cm² (c), PEO films irradiated with 100 MeV Ni^{7+} ions at the fluences of 1×10^{11} ions/cm² (d) and 1×10^{12} ions/cm² (e).

of unirradiated and irradiated PEO at the maximum fluence of 1×10^{12} ions/cm² for C^{5+} ion and Ni^{7+} ion are presented in Fig. 6. The thermograms show a sharp single endothermic peak in the temperature range 35–90 °C. This peak reveals the melting temperature (T_m) of the PEO and indicates the phase transition of PEO from semicrystalline to the amorphous phase. The degree of crystallinity at the maximum fluence was evaluated by the following formula [25]:

$$X_c = \Delta H_m / \Delta H_{m,0}$$

where ΔH_m is the enthalpy of melting per gram of PEO sample and $\Delta H_{m,0}$ is the melting enthalpy per gram of completely crystalline polymer, equal to 213.7 J/g [26]. Table 3 depicts the melting temperature and percentage crystallinity of unirradiated and irradiated PEO polymer films. In present case, T_m value is ~ 66.6 °C for pristine PEO and percentage crystallinity of pure PEO exhibited decreasing nature upon irradiation. It is attributed to reduction in the molecular weight of polymer due to the scissioning of polymeric chain. The DSC analysis reveals that the amorphization of the polymer upon ion irradiation. This result is also corroborated with the FTIR and XRD results.

3.6. Surface morphology

The SEM images of the unirradiated and irradiated PEO films with C^{5+} and Ni^{7+} ions at fluences of 1×10^{11} and 1×10^{12} ions/cm² are presented in Fig. 7(a–e). The pristine PEO shows a rough surface and surface became significantly smooth upon irradiation. The SHI irradiation led to the defect enhanced surface diffusion resulted in decrease of surface roughness [22]. The cracks seemed on the surface of PEO upon irradiation revealed destruction of spherulites structure of PEO polymer. The size of crack observed to be larger for Ni^{7+} ion as compare to those of C^{5+} ion irradiation. It is attributed to large electronic energy loss due to Ni-ion irradiation than C-ion.

4. Conclusions

PEO films irradiated with SHI of C^{5+} and Ni^{7+} ions at different fluences of ion beam. The XRD, FTIR and DSC analyses revealed that the crystallinity of the PEO decreases with increasing ion fluence. The crystalline nature was affected because of degradation of PEO's structure after irradiation by SHI. UV–Vis studies revealed a reduction in band gap and increase in cluster size, which may lead to change in dielectric property of the irradiated samples. The degradation caused some changes in the structure of PEO because of formation of carbon clusters, defects, decrease in molecular weight and unsaturation due to cleavage of the polymer chain. The changes in structural properties enhance the optical and dielectric properties of PEO. Scanning electron micrographs indicate decrease in surface roughness and exhibits destruction of spherulites structure of PEO upon irradiation. It is also observed that heavier Ni^{7+} ion caused more impact in the properties of PEO than

the lighter C^{5+} ion. It specified that energy, size and fluence of ion beam play a vital role in transforming the properties of the host polymer.

Acknowledgments

We express gratitude to IUAC, New Delhi, India, for providing SHI irradiation, characterization facilities and financial support. Gnansagar B. Patel is obliged to DST-PURSE for providing JRF. DRS materials laboratory is gratefully acknowledged.

References

- [1] E. Grossman, I. Gouzman, Space environment effects on polymers in low earth orbit, Nucl. Instr. Methods Phys. Res. Sect. B Beam Interact. Mater. Atoms. 208 (2003) 48–57, [http://dx.doi.org/10.1016/S0168-583X\(03\)00640-2](http://dx.doi.org/10.1016/S0168-583X(03)00640-2).
- [2] R.J. Woods, A.K. Pikaev, Applied Radiation Chemistry: Radiation Processing, John Wiley & Sons, 1994.
- [3] P.Y. Apel, A.Y. Didyk, B.I. Fursov, L.I. Kravets, V.G. Nesterov, G.S. Zhdanov, Particle track detection and relaxation transitions in polymer, Nucl. Instr. Methods Phys. Res. Sect. B 105 (1995) 91–96, [http://dx.doi.org/10.1016/0168-583X\(95\)00997-3](http://dx.doi.org/10.1016/0168-583X(95)00997-3).
- [4] Hou-Ching Yang, Joseph Silverman, Development and testing of radiation crosslinked poly(ethylene oxide) for sutureless anastomosis, Radiat. Phys. Chem. 25 (1985) 375–381.
- [5] E. Nedkov, S. Tsvetkova, Effect of gamma irradiation on the crystalline structure of ultra high molecular weight poly(ethylene oxide), Radiat. Phys. Chem. 43 (1994) 397–401, [http://dx.doi.org/10.1016/0969-806X\(94\)90034-5](http://dx.doi.org/10.1016/0969-806X(94)90034-5).
- [6] I.P. Tanja Jurkin, Irradiation effects in poly(ethylene oxide)/silica nanocomposite films and gels, Polym. Eng. Sci. 47 (2013) 21–25, <http://dx.doi.org/10.1002/pen>.
- [7] M. Doytcheva, R. Stamenova, V. Zvetkov, C. Tsvetanov, UV irradiation-induced crosslinking of solid poly(ethylene oxide) modified with tetraalkyl ammonium salt, Polymer (Guildf) 39 (1998) 6715–6721, [http://dx.doi.org/10.1016/S0032-3861\(98\)00133-5](http://dx.doi.org/10.1016/S0032-3861(98)00133-5).
- [8] C. Zhou, Q. Wang, Q. Wu, UV-initiated crosslinking of electrospun poly(ethylene oxide) nanofibers with pentaerythritol triacrylate: effect of irradiation time and incorporated cellulose nanocrystals, Carbohydr. Polym. 87 (2012) 1779–1786, <http://dx.doi.org/10.1016/j.carbpol.2011.09.095>.
- [9] M. Ramakrishna Murthy, E. Venkateshwar Rao, Ion-beam modifications of the surface morphology and conductivity in some polymer thin films, Bull. Mater. Sci. 25 (2002) 403–406, <http://dx.doi.org/10.1007/BF02708018>.
- [10] S. Kishore, N.L. Singh, 120 MeV Si¹⁰⁺ ions induced modifications of PEO/SnO₂ composites, Radiat. Effects Defects Solids 168 (2013) 547–556, <http://dx.doi.org/10.1080/10420150.2013.777442>.
- [11] B. Rupp, M. Schmuck, A. Balducci, M. Winter, W. Kern, Polymer electrolyte for lithium batteries based on photochemically crosslinked poly(ethylene oxide) and ionic liquid, Eur. Polym. J. 44 (2008) 2986–2990, <http://dx.doi.org/10.1016/j.eurpolymj.2008.06.022>.
- [12] J.F. Ziegler, M.D. Ziegler, J.P. Biersack, SRIM – The stopping and range of ions in matter, Nucl. Instr. Methods Phys. Res. Sect. B Beam Interact. Mater. Atoms. 268 (2010) 1818–1823, <http://dx.doi.org/10.1016/j.nimb.2010.02.091>.
- [13] P. Scherrer, Bestimmung der Größe und der inneren Struktur von Kolloidteilchen mittels Röntgenstrahlen, Nachrichten von der Gesellschaft der Wissenschaften zu Göttingen, Math. Klasse. (1918) 98–100.
- [14] V.M. Mohan, V. Raja, A.K. Sharma, V.V.R. Narasimha Rao, Ion transport and battery discharge characteristics of polymer electrolyte based on PEO complexed with NaFeF₄ salt, Ionics (Kiel) 12 (2006) 219–226, <http://dx.doi.org/10.1007/s11581-006-0035-1>.
- [15] S.J. Wen, T.J. Richardson, D.I. Ghantous, K.A. Streibel, P.N. Ross, E.J. Cairns, FTIR characterization of PEO+LiN(CF₃SO₂)₂ electrolytes, J. Electroanal. Chem. 415 (1996) 197, [http://dx.doi.org/10.1016/S0022-0728\(96\)01010-8](http://dx.doi.org/10.1016/S0022-0728(96)01010-8).
- [16] S. Singh, S. Prasher, The optical, chemical and spectral response of gamma-irradiated Lexan polymeric track recorder, Radiat. Meas. 40 (2005) 50–54, <http://dx.doi.org/10.1016/j.radmeas.2004.11.005>.
- [17] E. Tauc, in: A. Ables (Ed.), Optical Properties of Solids, 1970.

- [18] Z. Zhu, Y. Sun, C. Liu, J. Liu, Y. Jin, Chemical modifications of polymer films induced by high energy heavy ions, *Nucl. Instr. Methods Phys. Res. Sect. B Beam Interact. Mater. Atoms.* 193 (2002) 271–277.
- [19] J. Robertson, E. O'Reilly, Electronic and atomic structure of amorphous carbon, *Phys. Rev. B.* 35 (1987) 2946–2957, <http://dx.doi.org/10.1103/PhysRevB.35.2946>.
- [20] D. Fink, W.H. Chung, R. Klett, A. Schmoldt, J. Cardoso, R. Montiel, M.H. Vazquez, L. Wang, F. Hosoi, H. Omichi, P. Goppelt-Langer, Carbonaceous clusters in irradiated polymers as revealed by UV–Vis spectrometry, *Radiat. Eff. Defects Solids* 133 (1995) 193–208.
- [21] A.K. Jonscher, P. Place, Presentation and interpretation of dielectric data, *Thin Solid Films* 50 (1978) 187–204.
- [22] N.L. Singh, A. Qureshi, F. Singh, D.K. Avasthi, Effect of swift heavy ion irradiation on dielectrics properties of polymer composite films, *Mater. Sci. Eng. B.* 137 (2007) 85–92, <http://dx.doi.org/10.1016/j.mseb.2006.10.013>.
- [23] F.M. Reicha, M. El-Hiti, A.Z. El-Sonbati, M.A. Diab, Conducting polymers V: electrical conductivity of polymer complexes of bis-2,6-diaminopyridinesulphoxide-copper halides, *J. Phys. D Appl. Phys.* 24 (1991) 369–374.
- [24] N. Shah, D. Singh, S. Shah, A. Qureshi, N.L. Singh, K.P. Singh, Study of microhardness and electrical properties of proton irradiated polyethersulfone (PES), *Bull. Mater. Sci.* 30 (2007) 477–480, <http://dx.doi.org/10.1007/s12034-007-0075-9>.
- [25] N.L. Singh, A. Qureshi, N. Shah, A.K. Rakshit, S. Mukherjee, A. Tripathi, et al., Surface modification of polyethylene terephthalate by plasma treatment, *Radiat. Meas.* 40 (2005) 746–749, <http://dx.doi.org/10.1016/j.radmeas.2005.01.014>.
- [26] J.H. Shin, K.W. Kim, H.J. Ahn, J.H. Ahn, Electrochemical properties and interfacial stability of (PEO)₁₀LiCF₃SO₃–TiO_{2n-1} composite polymer electrolytes for lithium/sulfur battery, *Mater. Sci. Eng. B Solid State Mater. Adv. Technol.* 95 (2002) 148–156. pii: S0921-5107(02)00226-X.